NANOCELLULOSE MEMBRANES VIA LAYER-BY-LAYER ASSEMBLY

A THESIS SUBMITTED TO
THE GRADUATE SCHOOL OF NATURAL AND APPLIED SCIENCES
OF
MIDDLE EAST TECHNICAL UNIVERSITY

BY

ONUR KAAN AYDIN

IN PARTIAL FULFILLMENT OF THE REQUIREMENTS
FOR
THE DEGREE OF MASTER OF SCIENCE
IN
CHEMICAL ENGINEERING

MARCH 2024

Approval of the thesis:

NANOCELLULOSE MEMBRANES VIA LAYER-BY-LAYER ASSEMBLY

submitted by **ONUR KAAN AYDIN** in partial fulfillment of the requirements for the degree of **Master of Science in Chemical Engineering, Middle East Technical University** by,

Prof. Dr. Naci Emre Altun
Dean, **Graduate School of Natural and Applied Sciences**   _____

Prof. Dr. Yusuf Uludağ
Head of the Department, **Chemical Engineering**   _____

Prof. Dr. Pınar Zeynep Çulfaz - Emecen
Supervisor, **Chemical Engineering, METU**   _____

Prof. Dr. İrem Erel - Göktepe
Co-Supervisor, **Chemistry, METU**   _____

Examining Committee Members:

Prof. Dr. Halil Kalıpçılar
Chemical Engineering, METU   _____

Prof. Dr. Pınar Zeynep Çulfaz - Emecen
Chemical Engineering, METU   _____

Prof. Dr. İrem Erel - Göktepe
Chemistry, METU   _____

Prof. Dr. Nihal Aydoğan
Chemical Engineering, Hacettepe University   _____

Assoc. Prof. Dr. Simge Çınar - Aygün
Metallurgical and Materials Engineering, METU   _____

Date: 26.03.2024

I hereby declare that all information in this document has been obtained and presented in accordance with academic rules and ethical conduct. I also declare that, as required by these rules and conduct, I have fully cited and referenced all material and results that are not original to this work.

Name Last name : Onur Kaan Aydın

Signature :

ABSTRACT

NANOCELLULOSE MEMBRANES VIA LAYER-BY-LAYER ASSEMBLY

Aydın, Onur Kaan
Master of Science, Chemical Engineering
Supervisor : Prof. Dr. Pınar Zeynep Çulfaz - Emecen
Co-Supervisor: Prof. Dr. İrem Erel - Göktepe

March 2024, 139 pages

Membrane filtration is a cost-effective alternative to traditional separation processes and is diversely applied in treating aqueous streams. While organic solvents may be purified via membrane filtration, many common membrane materials are dissolved by organic solvents. Membranes were manufactured from cellulose for the investigation of their separation performance in aqueous environment as well as in Organic Solvent Ultrafiltration and Nanofiltration (OSU, OSN) applications.

Integrally Skinned Asymmetric (ISA) cellulose acetate membranes were prepared via Nonsolvent Induced Phase Separation (NIPS) and chemically treated to form cellulose membranes of tunable charge. The membranes were tested in water, methanol (MeOH), dimethylformamide (DMF), and dimethylsulfoxide (DMSO). The Pure Solvent Permeabilites (PSP), dye rejections and Molecular Weight Cut-Off (MWCO) values were evaluated.

Moreover, nanocellulose materials were synthesized, characterized and applied as Layer-by-Layer (LbL) coatings to cellulose ISA support membranes to improve the separation performance without significantly compromising PSP. The chemical and liquid crystal properties of these materials were studied. LbL self-assembled nanocellulose or nanocellulose / polyelectrolyte coatings were deposited onto the membranes. LbL modified membranes were tested under equivalent conditions and compared with the unmodified membranes.

The Layer-by-Layer modified membranes were stable in the solvents tested for up to a week as evidenced by constant PSP and MWCO values. The separation performance was improved based on MWCO values (5-6kDa vs. 15kDa in water, 17-18kDa vs. >35kDa in MeOH, 3-5kDa vs. 8kDa in DMSO, 2-4kDa vs. 18kDa in DMF). The membranes were found to be significantly negatively charged and could reject small molecules based on their charge (complete rejection of Rose Bengal (RB) in water, up to 95% RB rejection in MeOH). Consequently, the membranes were found to be promising for the separation of aqueous and organic solutions.

Keywords: Membrane, Cellulose, Nanocrystal, Ultrafiltration, Nanofiltration

ÖZ

KATMAN KATMAN KAPLANMIŞ NANOSELÜLOZ MEMBRANLAR

Aydın, Onur Kaan
Yüksek Lisans, Kimya Mühendisliği
Tez Yöneticisi: Prof. Dr. Pınar Zeynep Çulfaz - Emecen
Ortak Tez Yöneticisi: Prof. Dr. İrem Erel - Göktepe

Mart 2024, 139 sayfa

Membran ile sıvı ayırma, geleneksel sıvı ayırma süreçlerine ekonomik bir alternatiftir ve sulu çözeltilerin ayrımında sıklıkla kullanılır. Organik çözücüler de membranla ayrılabilir, ancak çoğu yaygın kullanılan membran malzemesi organik çözücülerde çözünür. Sulu çözelti ayrımı, organik çözücü ultrafiltrasyonu ve nanofiltrasyonu (OSU, OSN) uygulamalarında kullanılmak üzere selüloz membranlar hazırlandı.

Bütünleşik kaplamalı asimetrik (ISA) selüloz asetat membranlar çöktürücü kaynaklı faz ayrımı (NIPS) yöntemiyle hazırlandı ve ardından kimyasal muamele ile elektrik yükü ayarlanabilen selüloz membranlara çevrildi. Hazırlanan membranlar su, metanol (MeOH), dimetilformamid (DMF), dimetilsülfoksit (DMSO) gibi farklı çözücülerde test edildi. Membranların saf çözücü geçirgenlikleri (PSP), boya tutulma oranları ve molekül ağırlığı ayırma sınırları (MWCO) belirlendi.

Ayrıca nanoselüloz malzemeler sentezlendi, karakterize edildi ve ISA destek membranların geçirgenliğinden feragat etmeden ayrım verimini arttırmak için katman – katman kaplamada kullanıldı. Nanoselüloz sıvı kristal malzemelerin kimyasal ve koloidal özellikleri incelendi. Katman – katman (LbL) kendiliğinden yapılanma tekniği ile membran yüzeyine nanoselüloz veya nanoselüloz / polielektrolit kaplamalar uygulandı. Katman – katman kaplanan membranlar benzer şartlarda test edildi ve kaplanmamış membranlarla kıyaslandı.

Katman – katman kaplanan membranlar deneylerde kullanılan çözücülerde bir hafta süresince kararlı davranış ve sabit PSP ve MWCO değerleri sergiledi. Kaplanan membranların ayrım verimi kaplanmamış membranlara kıyasla üstün bulundu (suda 5-6kDa'ya kıyasla 15kDa, metanolde 17-18kDa'ya kıyasla >35kDa, dimetilsülfoksitte 3-5kDa'ya kıyasla 8kDa, dimetilformamidde 2-4kDa'ya kıyasla 18kDa). Membranların önemli derecede eksi yüklü oldukları ve yük ayrımı yoluyla eksi yüklü küçük molekülleri tuttukları gözlemlendi (rose bengal (RB) boyasının sulu ortamda tamamen tutulması, metanolde %95'e kadar tutulması). Sonuç olarak membranlar sulu ve organik çözeltilerin ısıl işlemsiz, enerji tasarruflu ayrımı için uygun bulundu.

Anahtar Kelimeler: Membran, Selüloz, Nanokristal, Ultrafiltrasyon, Nanofiltrasyon

To My Family

ACKNOWLEDGMENTS

TABLE OF CONTENTS

LIST OF TABLES

LIST OF FIGURES

FIGURES

LIST OF ABBREVIATIONS

ABBREVIATIONS

AcOH	Acetic Acid
BBR	Brilliant Blue R
BPEI	Branched Polyethyleneimine
BTB	Bromothymol Blue
CA	Cellulose Acetate
cP	centiPoise
CV	Crystal Violet
DLS	Dynamic Light Scattering
DMF	Dimethylformamide
DMSO	Dimethylsulfoxide
DS	Degree of Substitution
EtOH	Ethanol
ELS	Electrophoretic Light Scattering
GPC	Gel Permeation Chromatography
GTMAC	Glycidyltrimethylammonium Chloride
iPrOH	Isopropanol
kDa	kiloDalton
KHP	Potassium Hydrogen Phthalate
MADLS	Multiple Angle Dynamic Light Scattering

MeOH	Methanol
MF	Microfiltration
MW	Molecular Weight
MWCO	Molecular Weight Cut-Off
NF	Nanofiltration
NIPS	Nonsolvent Induced Phase Separation
NMMO	N-Methylmorpholine N-Oxide
PAA	Polyacrylic Acid
PAH	Polyallylamine Hydrochloride
PDAD	Polydiallyldimethylammonium Chloride
PEG	Polyethylene Glycol
PES	Polyether Sulfone
PSP	Pure Solvent Permeance
PSS	Polystyrene Sulfonate
PWP	Pure Water Permeance
RID	Refractive Index
RB	Rose Bengal
RO	Reverse Osmosis Water
ROP	Ring Opening Polymerization
TMP	Transmembrane Pressure
UF	Ultrafiltration
UPW	Ultra-Pure Water

CHAPTER 1

INTRODUCTION

Separation processes in chemical plants have high capital and operational costs. The most commonly used techniques, namely distillation, absorption, extraction, drying, leaching, and crystallization account for 40% to 70% of the total costs incurred. Therefore, traditional separation processes have a direct impact on energy requirements, product prices, and plant profitability (1).

Membrane processes have emerged as an alternative to the traditional separation processes discussed above. Membranes may be defined as semipermeable barriers which can separate substances with differing properties such as size, charge or affinity to the membrane material (2). Membrane processes have the potential benefit of being highly energy efficient. An illustration comparing the energy requirements of distillation without heat recovery and membrane filtration at 30 bar in concentrating a dilute solution is available in Figure 1.1 (3).
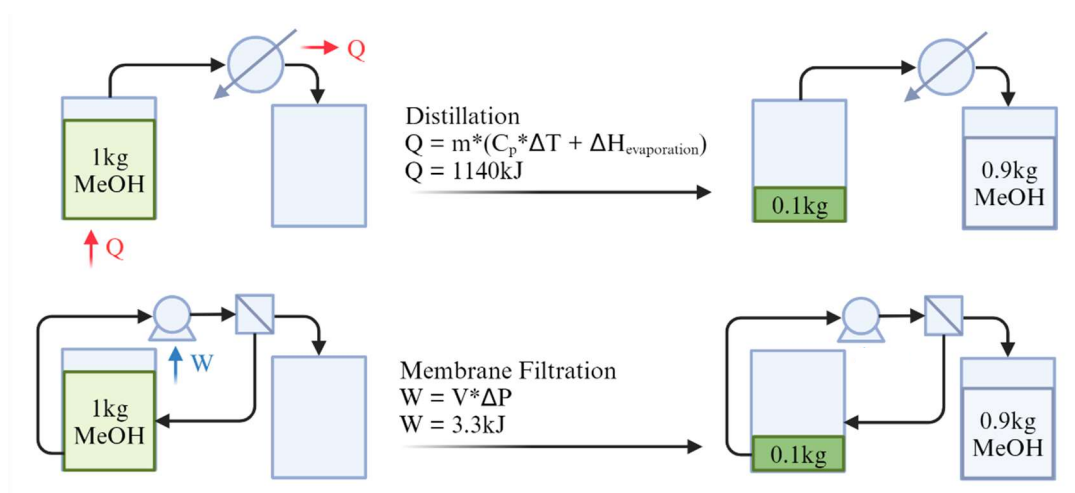
Figure 1.1 Energy Requirements of Distillation and Membrane Filtration in Concentrating 1kg of Dilute Methanol Solution Tenfold

Besides the treatment of aqueous solutions in processes like wastewater treatment (4) or desalination of saltwater (5); membrane liquid separation can also be applied to organic solutions (6–8). The main processes in organic solvent purification using membranes are organic solvent ultrafiltration (OSU), organic solvent nanofiltration (OSN) and organic solvent reverse osmosis (OSRO). Both of these processes remove impurities in organic solvents while avoiding increased energy consumption and flammable vapors encountered in distillation. Another benefit of membrane filtration is that the purification is conducted without heating, which can be dangerous for thermally labile solvents such as dimethyl sulfoxide (9).

Solvent resistant membranes can be made out of a diverse range of polymers including polyacrylonitrile, polyimides, fluoropolymers, and engineering polymers such as polyethersulfones and polyetherketones (7). However, many of these polymers are not resistant to polar aprotic solvents. In fact, solvents of this class are frequently used in dissolving the polymers for membrane preparation. The biopolymer cellulose is an alternative in solvent resistant membrane preparation. Besides being cheap, abundant and biodegradable (10), cellulose is insoluble except in select solvent systems such as ionic liquids (11), lithium chloride – dimethylacetamide, metal ammine solutions or amine oxides like NMMO (12).

A contemporary subject in membrane preparation is the application of layer-by-layer coatings. In this procedure, a selective layer is formed on top of porous support layers via the sequential application of positively and negatively charged substances. Although successful results and tunable membranes have been obtained in aqueous environments with this methodology (13–15) work in organic solvent filtration is sparse.

In this study, cellulose support membranes were prepared and coated using the layer-by-layer methodology. Nanocellulose was prepared , characterized and substituted in place of one or both polyelectrolytes. The resulting membranes were tested and compared with the support in aqueous as well as organic solvent media.

1.1 Classification of Membranes

Membranes can be classified according to their application area, morphology and material (2,16,17).

Table 1.1 Classification of Membranes Based on Application

Process	Pore Size	Pressure Range	Substances Rejected
Reverse Osmosis (RO)	Nonporous	> 5 – 10 MPa	Monovalent salts
Nanofiltration (NF)	1 – 10 nm	< 4 MPa	Organic molecules and multivalent salts
Ultrafiltration (UF)	5 – 100 nm	< 1 MPa	Macromolecules, proteins, viruses, colloids
Microfiltration (MF)	50 nm – 10 μm	5 – 500 kPa	Suspended particles and bacteria

As detailed in Table 1.1, a diverse range of membranes are available for various processes depending on the desired separation. As the permeability of the membranes decrease in the order MF > UF > NF > RO, the membrane with the largest pore size suitable for the particular separation is utilized to lower the necessary transmembrane pressure and membrane area.
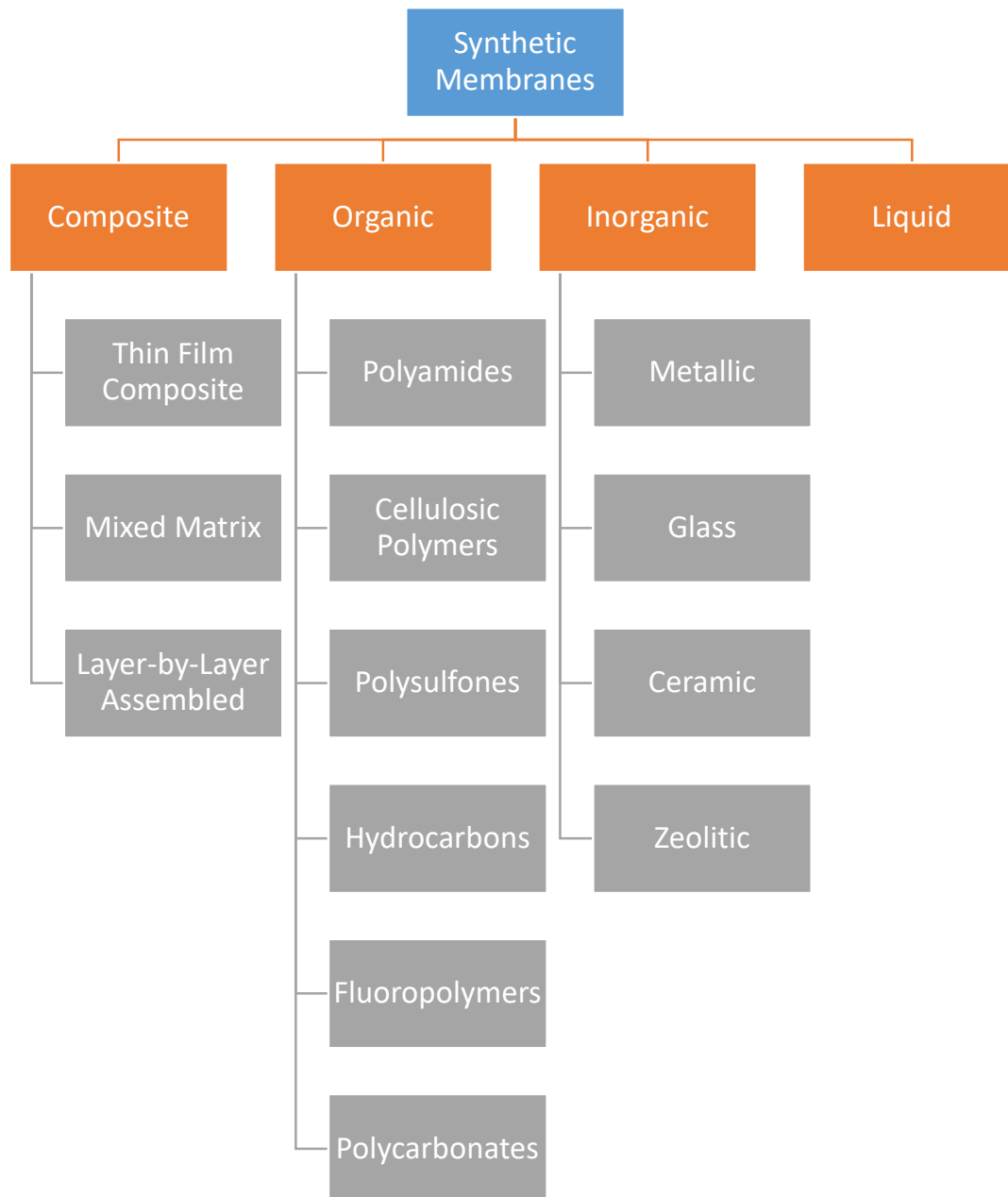
Figure 1.2 Classification of Membranes Based on Materials

As detailed in Figure 1.2, membranes can be manufactured out of a diverse range of materials. The material choice is made regarding the application the membrane will be used in. In the case of composite membranes, multiple materials are combined to take advantage of superior separation performance, permeability and mechanical stability.
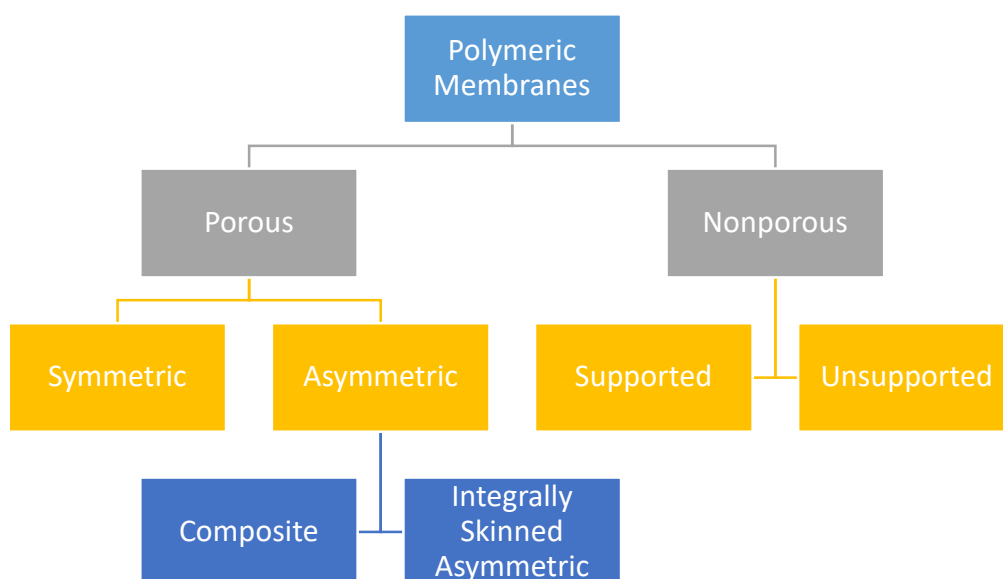
Figure 1.3 Classification of Polymeric Membranes Based on Morphology

Polymeric membranes can be made to be porous or nonporous. Among porous polymeric membranes, asymmetric membranes consisting of a dense skin layer with an underlying porous layer (see Figure 1.4) can be prepared. These membranes, called integrally skinned asymmetric (ISA) membranes have the advantage of having a thin selective layer which can effect the separation, and a porous layer underneath which mechanically supports the selective layer without diminishing the permeance by a large factor.

ISA membranes were discovered in 1962 by Loeb S. and Sourirajan S. (18) and are prepared from a single polymer in a single phase inversion step. The procedure has since been studied in detail and expanded upon (19,20). Due to their high performance and ease of production, ISA membranes represent a significant share of commercial membranes (21).
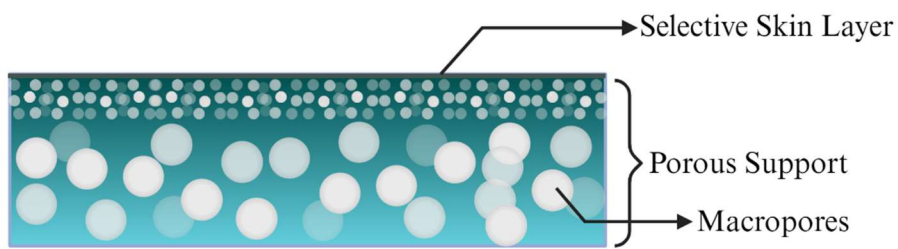
Figure 1.4 Schematic of an ISA Membrane

Another type of asymmetric membrane is composite membranes. These are formed from multiple materials and the selective layer differs in material identity. Commonly, the selective layer is a polyamide film formed with interfacial polymerization on top of a porous support membrane. Polyamide composite membranes can be used for NF and RO processes, and are suitable for applications like desalination (22).

1.2   Transport Through Membranes

Transport through membranes takes place under a driving force such as pressure difference, chemical potential difference, or electric potential difference across the sides of the membrane. There are two distinct transport modes in membranes, depending on the membrane and the substance being filtered. These modes are named pore-flow and solution-diffusion (23).
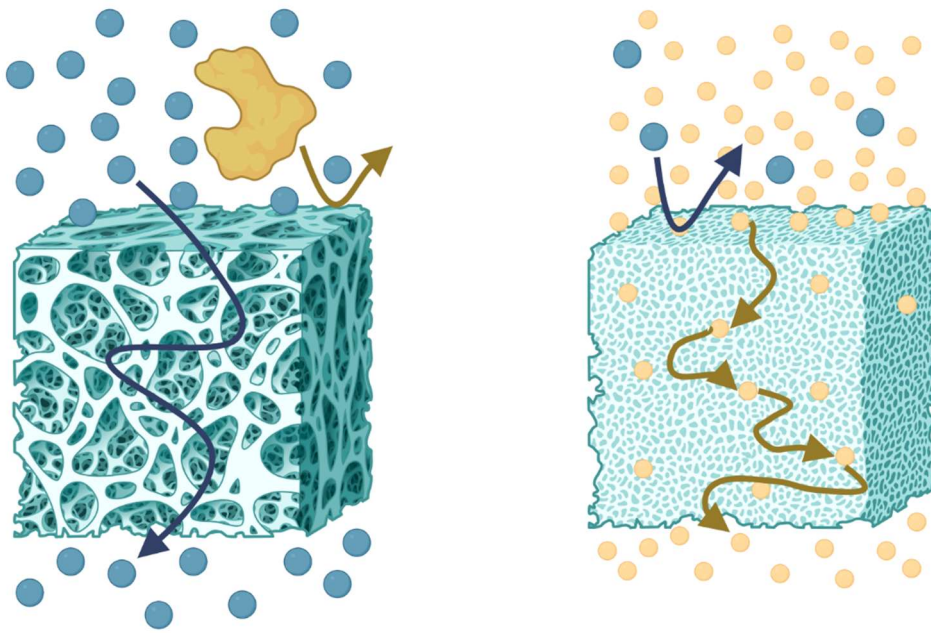
Figure 1.5 Illustration of Transport Across a Membrane: Pore-flow mode (left) and solution-diffusion mode (right)

As seen in the left hand side of Figure 1.5, pore flow occurs when the permeating species is smaller than the membrane pores and can flow through. This is the case for porous membranes and permeating species of low molar volume, such as solvents. In this case, liquid flow through the membrane can be described by traditional fluid mechanics (24,25) and the Hagen-Poiseuille equation holds true (2).

$$J = \frac{\Delta P * \varepsilon * d^2}{32 * \mu * l}$$

In reality, flowing liquid can take multiple paths through the membrane, and the pores are not vertical cylinders. Therefore, an additional parameter, tortuosity (τ) is included in the equation. Tortuosity has the physical significance of the average length of path taken by the fluid divided by the thickness of the media it is permeating through (26).

$$J = \frac{\Delta P * \varepsilon * d^2}{32 * \mu * \tau * l}$$

In the case of liquid flow through pores of cylindrical cross-section, an equation can be derived for the rejection of solutes. This is based on the fact that the solute needs to pass through the pore without touching the walls, and therefore can only travel through a select part of the cross-section (27).
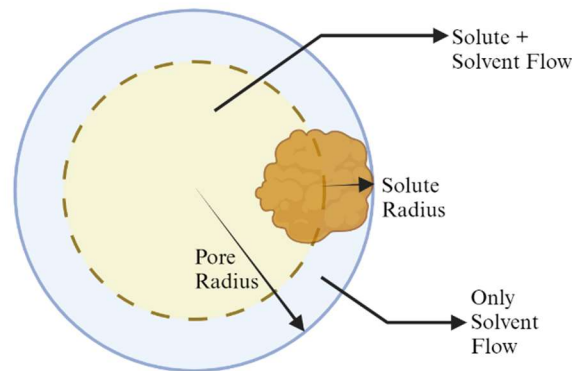
Figure 1.6 Flow Through a Pore with Size Sieving

As pore radii of membranes are very small, the flow is laminar and assumes a parabolic velocity profile. By taking the velocity profile of the fluid into consideration, the Ferry-Renkin equation relates rejection (R) to pore and solute radii (termed r and a respectively).

8

$$R = \left[1 - 2 * \left(1 - \frac{a}{r}\right)^2 + \left(1 - \frac{a}{r}\right)^4\right] * 100\%$$

In the alternative transport mode displayed on the right hand side of Figure 1.5, solution-diffusion, the permeating species first dissolves in the matrix material of the membrane and then diffuses through. The main difference between the two models is that pressure is assumed to drop gradually across a membrane filtering fluid in pore flow regime, while pressure remains constant in a membrane in solution-diffusion regime and drops abruptly at the permeate side. The driving force for permeation is then the activity gradient within the membrane. Solution-diffusion transport mode is important in nonporous membranes and in the case the permeating species has significant solubility in the matrix material (28).

1.3   Cellulose Membranes

Commercial polymeric membranes are frequently made out of the polymers polysulfone (PS), cellulose acetate (CA), polyacrylonitrile (PAN) and polyvinylidene fluoride (PVDF) (29). Cellulose is an attractive alternative as it is abundant and biodegradable. Cellulose also has excellent stability in many solvents and is insoluble, which can be inferred from the research on specialized solvents which can dissolve cellulose.

Table 1.2 Solvent Systems Which Can Dissolve Cellulose

Solvent / Reagent	Mode of Dissolution	Reference
Ionic Liquids	Hydrogen bond breaking	(30)
Amine Oxides	Hydrogen bond breaking	(31,32)
LiCl / DMAc	Coordination of metal ion	(33,34)
Cuoxam / Cadoxen	Coordination of metal complex	(35,36)
CS_2 in Alkali	Xanthate derivatization	(37,38)

As seen in Table 1.2, solvents need to break up the hydrogen-bond network or chemically modify the hydroxyl groups in cellulose in order to dissolve it. Since regular solvents have no capability of doing so, cellulose is stable and remains solid in many commonly used solvents such as hydrocarbons, aromatic solvents, alcohols, ketones, ethers, esters, chlorinated solvents and polar aprotic solvents such as acetonitrile, dimethyl sulfoxide, dimethylformamide, dimethylacetamide and N-methyl pyrrolidone. This gives cellulose the ability to filter solvents which would dissolve membranes made of other polymers. For example, the solvent dimethylformamide (DMF) dissolves all four of the polymers PS, PAN, CA and PVDF (39–42), whereas cellulose is insoluble in neat DMF (43) and can be used in filtering it.

Preparation and uses of cellulose membranes are summarized in Table 1.3.

Table 1.3 Examples of Preparation and Applications of Cellulose Membranes

Preparation	Application / Performance	Reference
Casting from CA solutions in DMSO, Acetic Acid and Acetone, Subsequent Regeneration	Aqueous solution filtration, diverse MWCO values from 35 – 2kDa.	(44)
Casting from CA solutions in DMSO, PEG 400 and Acetone, Subsequent Regeneration and Annealing	Aqueous and organic solution filtration in the solvents DMSO, methanol, propylene glycol methyl ether acetate, purification of photolithography wastes.	(45)
Casting from CA Solutions in DMSO and Acetone, Thermal Treatment and Regeneration	Polypropylene glycol 950Da and dye removal in polar solvents	(46)
Spinning from Cellulose Solutions in Ionic Liquids	Dye removal in water and alcohol	(47)
Spinning from Cellulose Solutions in Ionic Liquids	Oil-water emulsion separation	(48)
Alfa Laval RC70PP Commercial Regenerated Cellulose Membrane	Successful removal of phenolics and reduction of chemical oxygen demand in olive oil process water	(49)
Alfa Laval RCA 10, RCA 30, RCA 100 Commercial Regenerated Cellulose Membranes	Successful recovery of phytosterol antioxidants from orange juice	(50)

Table 1.3 (Continued)

Millipore 1 kDa Hydrophilic Regenerated Cellulose Membrane PLAC07610	Successful concentration of sugars and fructans with the aim of separating agave juice	(51)
Millipore 300 kDa Ultracel Regenerated Cellulose Membrane	Potato protein isolation with removal of polyphenol oxidase, superior performance to PES membranes	(52)
Millipore 1 kDa Regenerated Cellulose Membrane	Successful separation and concentration of sugars obtained from the hydrolysis of pine wood hemicellulose	(53)
Millipore 5 kDa and 10 kDa Regenerated Cellulose Membrane	Successful concentration of collagen from aqueous solutions	(54)

As detailed in Table 1.3, commercial and prepared cellulose membranes have been applied successfully to a wide variety of processes. However, work on organic solvent filtration using cellulose membranes is relatively sparse and represents an opportunity to develop novel membranes.

1.3.1   Cellulose Membrane Fabrication

For membrane preparation polymers are frequently dissolved, and the solution is cast. However, direct dissolution of cellulose represents challenges. One drawback is that specialized solvent mixtures are needed, which can contain expensive (ionic liquids) or toxic (cuoxam, cadoxen, CS_2) substances. Another challenge is that there is very little work done on morphology control of membranes prepared from such niche solvents.

Cellulose membrane preparation is instead commonly done through the preparation of cellulose acetate membranes and their subsequent hydrolysis (44,45,55). One advantage of this approach is that cellulose acetate is widely soluble in organic solvents, and can also be dissolved in solvents that are of low toxicity (acetone, acetic acid, DMSO) (44). Another benefit is that ISA membranes can be prepared from the solutions mentioned (56). Cellulose acetate membranes then undergo alkaline hydrolysis and are turned into cellulose. The reaction taking place is detailed in Figure 1.7.
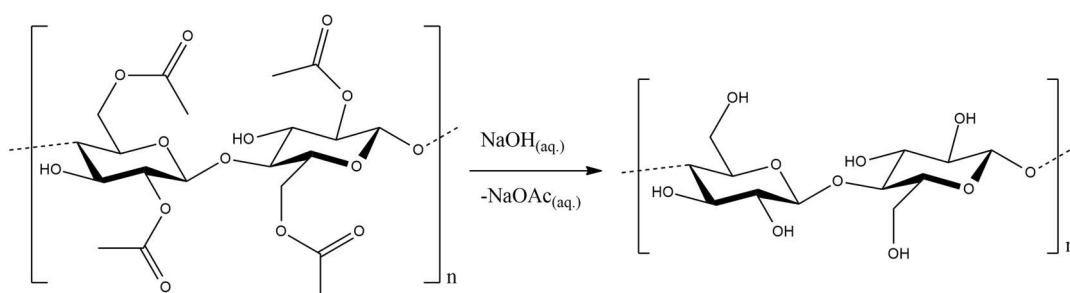
Figure 1.7 Alkaline Hydrolysis (Regeneration) of Cellulose Acetate

The hydrolysis reaction is conducted in a dilute (0.05 – 0.2M) solutions of NaOH in pure water or ethanol (45,46,57). In case of aqueous treatment with 0.05M NaOH, the reaction has been found to be complete within 24 hours at room temperature as inferred by FTIR data (45).

Cellulose membranes can be chemically modified in a number of ways to change properties such as hydrophilicity or zeta potential. One such method is the esterification of cellulose with polycarboxylic acids such as succinic acid, citric acid or 1,2,3,4-butanetetracarboxylic acid whose structures are displayed in Figure 1.8. The esterification can be conducted in aqueous environment with monosodium phosphate as the catalyst (58). The remaining carboxyl groups of the polycarboxylic acid may remain free and ionize in solution to yield a negatively charged membrane, or may esterify with other cellulose chains to crosslink the structure and provide mechanical rigidity.
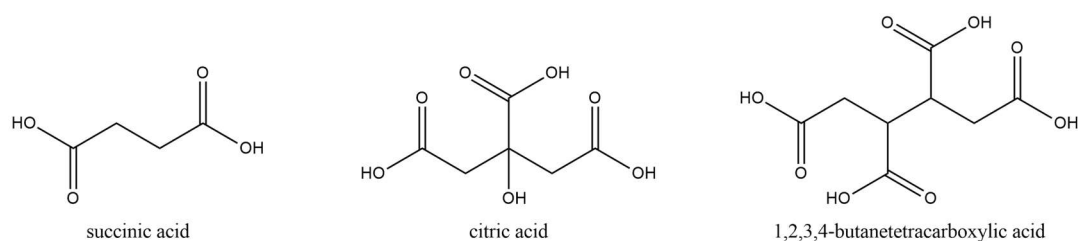
Figure 1.8 Polycarboxylic Acids for Cellulose Modification

Esterification can also be accomplished via a reaction with acid anhydrides such as phthalic anhydride. In this case, the solvent either has to be aprotic or should be a carboxylic acid to avoid solvolysis of the anhydride. Acetic acid has been found to be a suitable solvent for phthalic anhydride, and anhydrous sodium acetate has been found to be a satisfactory catalyst to effect the conversion (59).

The hydroxyl groups present on cellulose can also act as nucleophiles under suitable conditions, and can displace halides via substitution or can attack epoxide rings. These reactions have the benefit of forming ether linkages, which are less prone to hydrolysis compared to ester linkages. Reagents used to modify cellulose in this way are sodium 3-bromopropylsulfonate, 3-bromopropyltrimethylammonium bromide (60,61), chloroacetic acid (62) and glycidyltrimethylammonium chloride (63–65). The structures of these reagents are available in Figure 1.9.

14
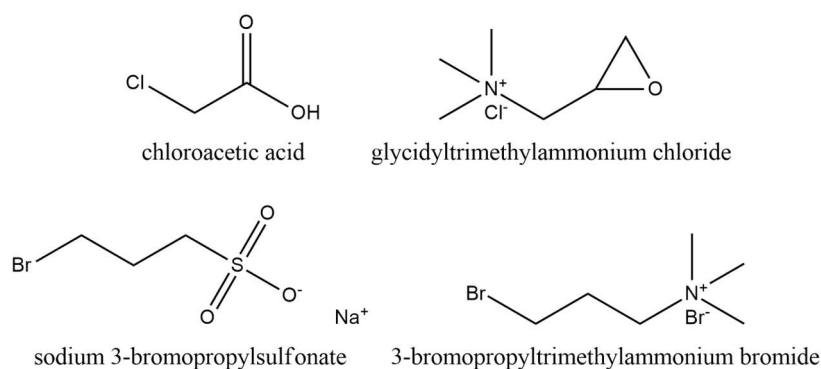
Figure 1.9 Some Reagents Used for Cellulose Derivatization

1.4   Nanocellulose Materials

Cellulose from natural sources (e.g. cotton, wood pulp, corncobs) can be processed via chemical or mechanical methods to yield nanocellulose. Nanocellulose is characterized by very small particle sizes and dispersibility in water.

Based on their morphology, two different nanocellulose materials are available. Cellulose nanocrystals (CNC) are entirely composed of the crystalline region of the fibrils and is produced via chemical treatment (hydrolysis) of cellulose.

Cellulose nanofibrils (CNF) are the building blocks of cellulose fibers in plant material and can be separated via mechanical delamination. This procedure can be combined with a chemical treatment to stabilize the CNF produced against aggregation. CNF particles are composed of both the crystalline and amorphous structures of cellulose.

Both CNC and CNF display high aspect ratios but the fibrils are considerably longer than nanocrystals. Both nanocellulose materials are biocompatible and biodegradable. Cellulose nanocrystals are mechanically robust with elastic moduli rivaling Kevlar and tensile strengths greater than cast iron. Finally, both forms have very high surface area and abundant hydroxyl groups available for modification (66–68). A schematic of how these particles are manufactured is available in Figure 1.10.
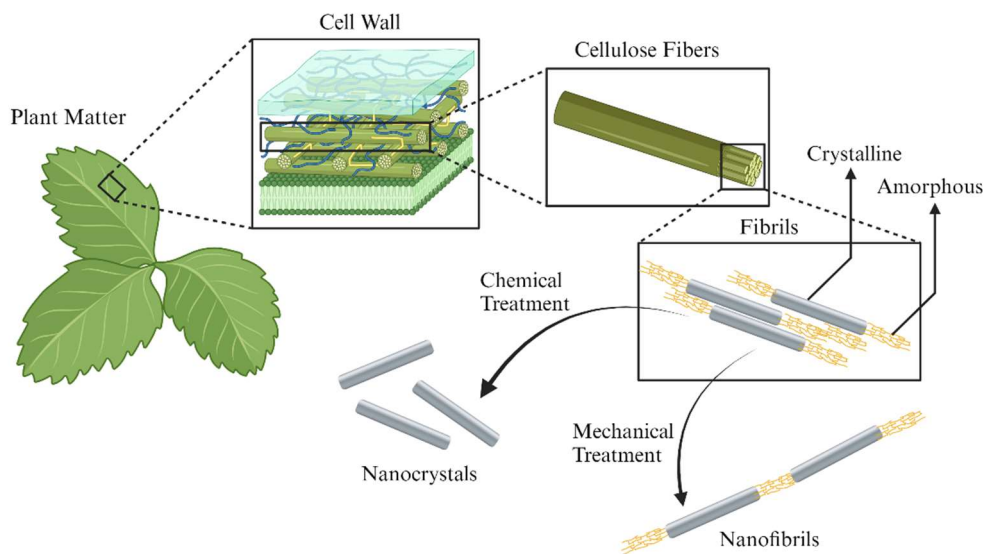
Figure 1.10 Nanocellulose Source and Extraction

Nanocellulose is used in reinforcing plastics owing to its high mechanical resilience and transparency in the polymer phase. It can also be used as an amphiphobic surface coating capable of repelling polar as well as nonpolar liquids. In the medical field, nanocellulose has been applied as a wound dressing and as a drug carrier (68).

Another possible use of nanocellulose is in improving membrane properties. Nanocellulose can be deposited in an aligned state and used as a tunable selective layer (69,70), coated onto membranes to limit fouling (71), or used as a component in the preparation of mixed matrix membranes (MMM) (72).

1.4.1 Chemical Modification of Nanocellulose

The abundant hydroxyl groups present on the surface of nanocellulose can be derivatized in several ways. This procedure aims to obtain nanocellulose with a desirable zeta potential, suitable surface polarity, or with appropriate chemical makeup. Common reactions to derivatize the surface include etherification, oxidation, desulfation, silylation, esterification with organic or mineral acids, and urethanization (73). These methods are summarized in Table 1.4.

Table 1.4 Methods for Chemical Derivatization of Nanocellulose

Reaction	Reagent and Group Introduced	Application	References
Etherification	Epoxides or halides, ethers introduced	Installation of robustly bound charged groups to alter surface charge	(74,75)
Oxidation	TEMPO / NaOCl / NaBr oxidant, carboxylic acid groups introduced	Altering rheological properties, zeta potential and pH dependent behavior	(76)
Desulfation	Alkali, sulfate groups removed	Altering zeta potential	(77)
Silylation	Orthosilicates or halosilanes, silyl groups introduced	Installation of robustly bound ionizable or hydrophobic groups	(78,79)
Esterification	With organic acids or acyl halides, esters introduced	Improving dispersibility for nanocomposites, or introducing functional groups through bifunctional acids	(80–82)
	With phosphoric acid, phosphates introduced	Improving dispersibility and biocompatibility	(83)
	With sulfuric or sulfamic acid, sulfates introduced	Introduced as part of synthesis, improves dispersibility	(77,84)
Urethanization	Isocyanates, urethane groups introduced	Applied in the production of self-healing nanocomposites	(85)
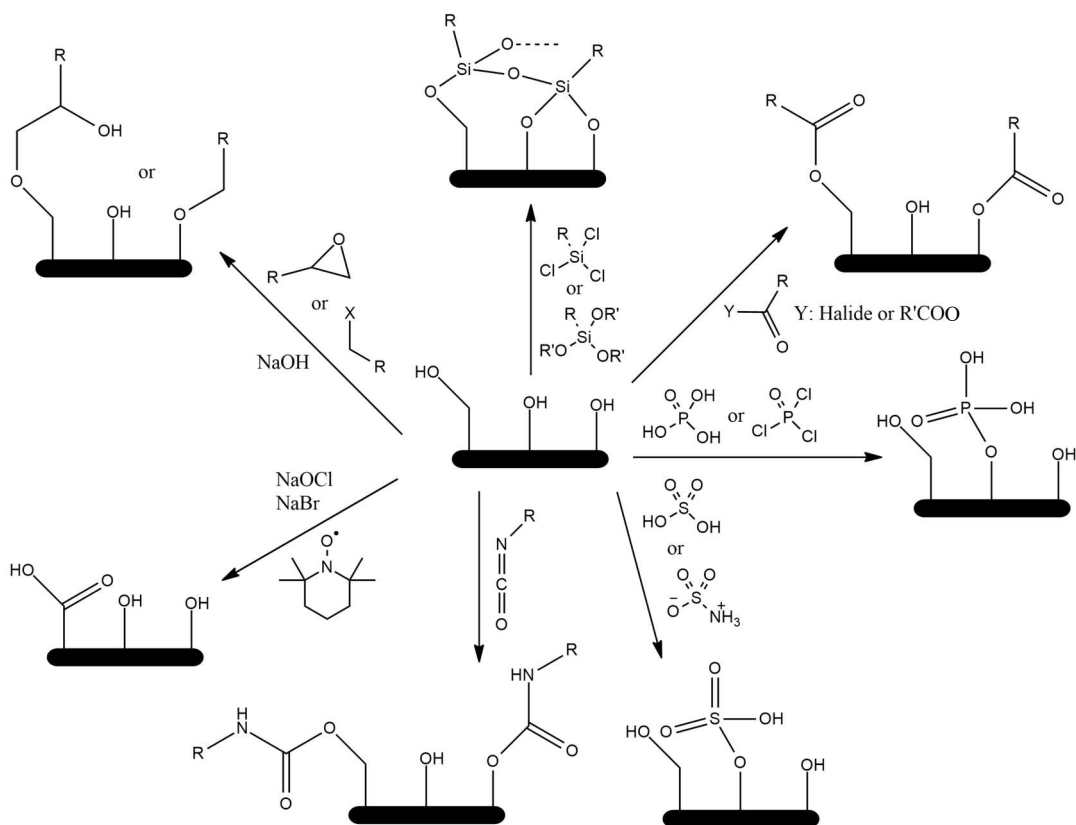
Figure 1.11 Chemical Derivatization of Nanocellulose

1.5   Layer-by-Layer Assembly

Layer-by-Layer (LbL) assembly is a fabrication method for preparing ordered thin films from oppositely charged materials such as polymers or colloids. In this method, thin films are formed on suitable surfaces by alternately applying substances of opposite electric charge with washing steps in between (86). The multilayer films are made out of extremely thin alternating layers with uniform coverage. Multilayer films can be useful in a wide variety of applications including membranes (87), catalysts (88), stimuli responsive materials (89,90) and medicine (91–95).

In LbL assembly, the positive and negatively charged layers form the basic subunit of the structure called a bilayer. Multiple bilayers are frequently deposited to achieve the desired characteristics for the particular application.

A variety of methods have been developed to apply the substances to the surface. These include immersion coating, spin coating, spray coating, electromagnetic coating and fluidic systems. In immersion coating, the substrate is submerged in a liquid containing the material to be adsorbed to the surface. Excess materials are then washed away and the material of opposite charge is applied in the same fashion. Immersion coating can be applied to obtain coatings of nanoparticles (96,97) and polymers (98). If the substrate material is permeable as in membrane applications, the liquid used in coating may be permeated through with applied pressure to force the deposition (99). In spin coating, the coating liquid is dripped in the center of a disk of substrate, which is spun at very high rate so that a uniform coating is obtained and excess materials fly off (100). In spray coating, the liquid is sprayed onto the substrate to uniformly wet the surface (101). In electromagnetic coating, an electric field (102) or magnetic field (103) is applied to attract charged or magnetic particles to the surface. In fluidic coating, LbL assembly is performed in microfluidic channels and this method can be used to change the properties of the channel itself or to coat small particles (104).

LbL assembly on membranes can be done by immersion coating, spin coating, and spray coating as well as novel methods such as inkjet printing (105). However, immersion coating remains a popular method as it requires no specialized equipment, can be applied while the membrane is fixed in a filtration module, and as it can coat nonplanar surfaces such as the inside surfaces of hollow fiber membranes.

Membranes are most frequently coated with polymers with an ionizable group in their repeating units, called polyelectrolytes. Polyelectrolytes ionize to varying degrees in solution and exist as multiply charged species. The structures of some commonly utilized polyelectrolytes are available in Figure 1.12.
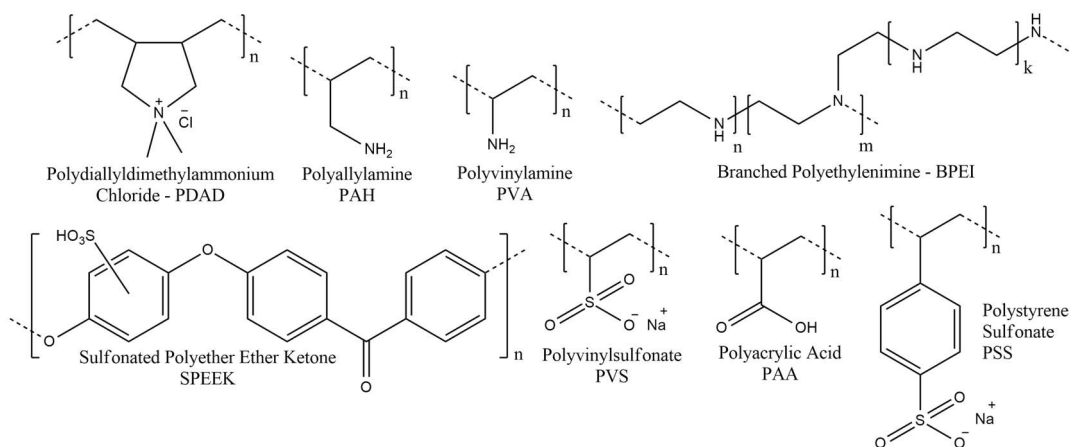
Figure 1.12 Polyelectrolyte Structures

Polyelectrolytes can adsorb onto membranes through electrostatic interactions. The subsequent deposition of an oppositely charged polyelectrolyte at the surface can form a film composed of a bilayer of the two oppositely charged polyelectrolytes. The deposition of polyelectrolytes is followed by rinsing steps to get rid of the loosely bound polyelectrolytes. The deposition and rinsing steps steps may be repeated to obtain films composed of alternating layers of positively and negatively charged polyelectrolytes. This procedure is called layer-by-layer (LbL) self-assembly, and the LbL-coated membranes prepared are called polyelectrolyte multilayer membranes (PEMM) (87).

Polyelectrolyte multilayer coatings can form excellent selective layers due to their dense structure covering the surface of the support membrane. The permeability of PEM membranes is not diminished significantly when compared to the support membrane itself since the selective layer formed from the polyelectrolytes is very thin (106).

Furthermore, the properties of PEM membranes can be tuned during their preparation. By changing the coating parameters, various coatings with different selectivities and permeabilities can be prepared.

Some applications of PEM membranes are summarized in Table 1.5 the structures and names of the polymers, which are abbreviated in Table 1.5, are available in Figure 1.12.

Table 1.5 Polyelectrolyte Multilayer Membrane Liquid Separation Applications.

Polyanion	Polycation	Number of Bilayers	Application, Performance	Reference
PSS	PDAD	4.5	NF, phosphate removal, 98% rejection	(107)
PSS	PAH	7	NF, amino acid separation, 90% glutamate rejection	(108)
PSS	PAH	4.5	NF, amino acid and sugar separation from salt, 99% sucrose rejection	(109)
PSS	PAH	5	NF, multivalent salt removal, 22.5 Na^+/Mg^{2+} and 50 Na^+/Ca^{2+} selectivity	(110)
PSS	PDAD	4	NF, fluoride removal from other anions, 3.4 Cl^-/F^- selectivity	(111)
SPEEK	PDAD	5	NF, monovalent multivalent anion separation, 20 Cl^-/SO_4^{2-} and Cl^-/HPO_4^{2-} selectivity	(112)
SPEEK	PDAD	20	Solvent resistant NF, dye removal, 99% rejection	(113)
PVS	PVA	60	RO, desalination, complete divalent cation removal, 96% NaCl rejection	(114)
PVS	PVA	60	RO, desalination, 98% magnesium, 96.4% calcium, 74.5 sodium salt rejection	(115)

Table 1.5 (Continued)

PAH (pH 7.5)	PAA (pH 3.5)	10-20 with thermal crosslinking	RO, desalination, 99.8% salt rejection	(116)

As detailed in Table 1.5, polyelectrolyte coatings can be used to manufacture membranes with good selectivity from nonselective support membranes. Depending on the polyelectrolytes used, and the conditions applied during coating, it is possible to obtain a diverse range of membranes suitable for various processes. In particular, polyelectrolyte type, ionic strength and pH are frequently varied to obtain different coatings. The effects these parameters have are summarized in Table 1.6.

Table 1.6 Experimental Parameters and Their Effects in LbL Coating

Parameter	Effect	Reference
Polyelectrolyte Type (Weakly / Strongly Ionizing)	Weak polyelectrolytes deposit in greater quantities, leading to thicker layers	(117)
Ionic Strength	High ionic strength leads to thicker, more hydrated layers	(118)
pH	Changes the degree of ionization for weak polyelectrolytes. Influences thickness and growth regime.	(119)

It has also been shown that nanocellulose materials are suitable for use in the layer-by-layer self-assembly methodology due to their multiple charges (120). The assemblies thus formed from nanocellulose are proposed as reinforcing materials, oxygen barriers or biocompatible electrodes (121–123).

1.6 Aim of Study

Membrane filtration is commonly used to separate aqueous solutions and has the advantage of being an energy efficient, non-thermal separation process. Although membrane separation is applicable to organic solvents, many common membrane materials are soluble in organic solvents and hence cannot be used in filtering them. An alternative, promising membrane material is cellulose. Cellulose has the advantages of having excellent solvent resistance, and being highly abundant and biodegradable.

In this study, the objective is to prepare cellulose membranes and to test their separation performance in aqueous and organic liquid separations by performing rejection tests. The applicability of nanocellulose materials in forming LbL assembled selective layers will be explored by synthesizing and characterizing nanocellulose materials, forming LbL assemblies on cellulose membranes and contrasting the rejections with the unmodified membranes. The membranes obtained are aimed to be suitably stable in aqueous as well as organic environments, and should ideally have favorable rejections and permeabilities.

To accomplish this objective, integrally skinned asymmetric cellulose acetate ultrafiltration membranes were prepared via the phase inversion method. These were turned into cellulose membranes suitable for layer-by-layer coating application and were prepared by alkaline hydrolysis followed by chemical treatment. Nanocellulose materials were synthesized from cotton linter cellulose, characterized and chemically modified if needed. Polyelectrolyte – nanocellulose coatings were deposited onto cellulose support membranes and their separation performances were contrasted with that of the support membrane. All – cellulose coatings were also prepared and tested.

CHAPTER 2

EXPERIMENTAL METHODS

2.1   Materials

Cellulose acetate (CA, Mn ∼50kDa by GPC), cotton linter cellulose, cellulose membrane dialysis tubing (14kDa MWCO), polyethylene glycol (TEG, PEG 400Da, 600Da, 1kDa, 2kDa, 6kDa, 10kDa, 20kDa, 35kDa), glycidyltrimethylammonium chloride (GTMAC, 90%), sodium bromide (NaBr, ACS), 2,2,6,6-tetramethylpiperidine N-oxide (TEMPO, 98%), rose bengal (RB), brilliant blue R (BBR), bromothymol blue (BTB), naproxen sodium salt (98-102%), atenolol (98%), branched polyethyleneimine (BPEI, 50kDa), and polyacrylic acid of two different molecular weights (PAA, 1.8kDa powder or 250kDa 35 wt. % aqueous solution) were purchased from Sigma-Aldrich. Sulfuric acid (95-97%), acetic acid (AcOH, 99.8), sodium hydroxide (NaOH, 99%), dimethyl sulfoxide (DMSO, 99.9%), dimethyl formamide (DMF, 99%), methanol (MeOH, 99%), ethanol (EtOH, 99.9%), isopropanol (iPrOH, 99.5%) were purchased from ISOLAB. Polyether sulfone (PES) was purchased from BASF. Sodium chloride (ACS), hydrochloric acid (ACS, 37%, fuming), phthalic anhydride (ACS), phenolphthalein (ACS), and crystal violet (CV, ACS), potassium hydrogen phthalate (KHP, ACS), potassium hydroxide (KOH) were purchased from Merck. Commercial sodium hypochlorite solution was standardized and used. Anhydrous sodium acetate was obtained by neutralizing acetic acid with NaOH and driving off water at 200ºC. Cellulose nanofibers (CNF) were prepared by Prof. Dr. Sedat Ondaral at KTU.

2.2   Preparation of Polymer Solutions

Three different membrane casting solutions were prepared. The compositions of the solutions are detailed in Table 2.1.

Table 2.1 Membrane Casting Solution Compositions

Membrane	Polymer	Solvent
CA15	15 wt. % CA	85 wt. % DMSO
CA12-UPW8	12 wt. % CA	80 wt. % DMSO, 8 wt. % water
PES15	15 wt. % PES	85 wt. % DMSO

The polymers CA and PES were dried under vacuum for at least one week before preparing the solutions. An appropriate amount of solvent was placed in glass bottles, and the weighed polymer was added on top. The contents were stirred with a magnetic stirrer. The bottles were then placed onto a roller mixer where they remained until homogenous solutions were obtained. The bottles were finally allowed to rest until no gas bubbles remained. A schematic for polymer solution preparation is available in Figure 2.1.
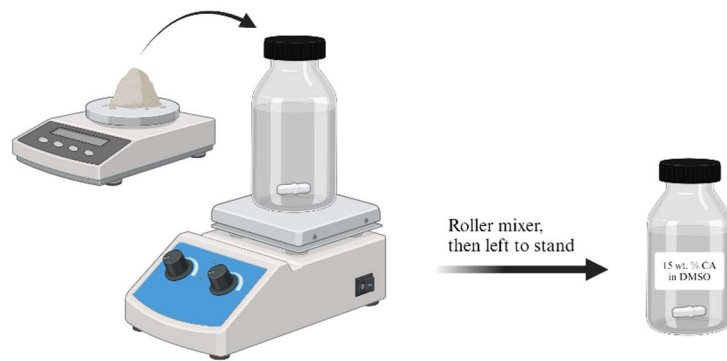
Figure 2.1 Polymer Solution Preparation

2.3 Support Membrane Preparation Procedure

The casting solutions were applied with 0.25mm thickness onto clean glass panes with the help of a casting bar. The glass panes were immediately placed into large tubs containing reverse-osmosis (RO) water, where nonsolvent-induced phase separation (NIPS) took place. After phase separation finished, the membranes obtained were removed from water and were marked such that the skin layer of the membrane could be distinguished. A schematic for support membrane preparation is available in Figure 2.2.
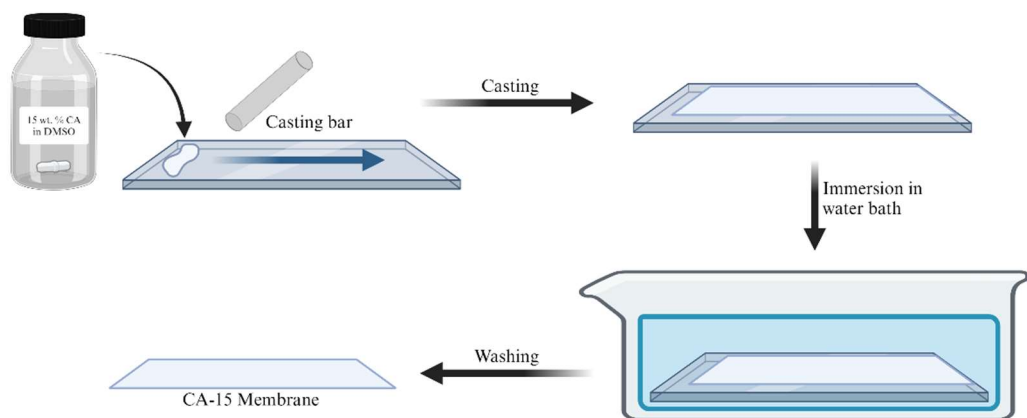
Figure 2.2 Support Membrane Preparation

The membranes were placed in beakers containing RO water and washed for another day before being stored in 20 vol. % EtOH as a preservative.

Some membranes were subjected to alkaline hydrolysis to hydrolyze the cellulose acetate into cellulose. In this procedure, membranes made from the polymer CA were placed in solutions of 0.05M NaOH in ultra-pure water (UPW) for 24 hours. No less than two liters of this alkaline solution was used per membrane of approximate size 10cm by 25cm. After hydrolysis was complete, the membranes were washed thoroughly with UPW, and stored in 20 vol. % EtOH as a preservative. This regeneration procedure is detailed in Figure 2.3.
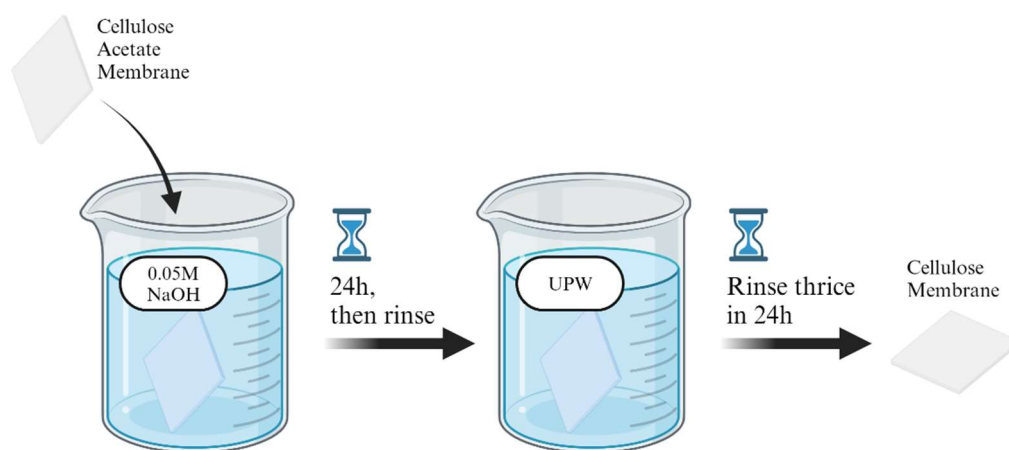
Figure 2.3 Regeneration of Cellulose Membranes

Some cellulose membranes were further chemically treated in order to install ionizable groups on their surfaces. In this process, the membranes were solvent exchanged first to EtOH and then to AcOH, as AcOH is a suitable solvent for acid anhydrides (59). Meanwhile, the reaction mixture comprising of 5 wt. % phthalic anhydride and 1 wt. % anhydrous sodium acetate in AcOH was prepared by mild heating (up to 50°C) while stirring.

No more than three membranes of approximate size 10cm by 25cm were submerged in 200mLs of reaction mixture and were treated for four hours at room temperature. After the reaction, the membranes were removed from the liquid and thoroughly washed first with EtOH and then with UPW until no acidic traces remained. A schematic for this procedure is available in Figure 2.4.
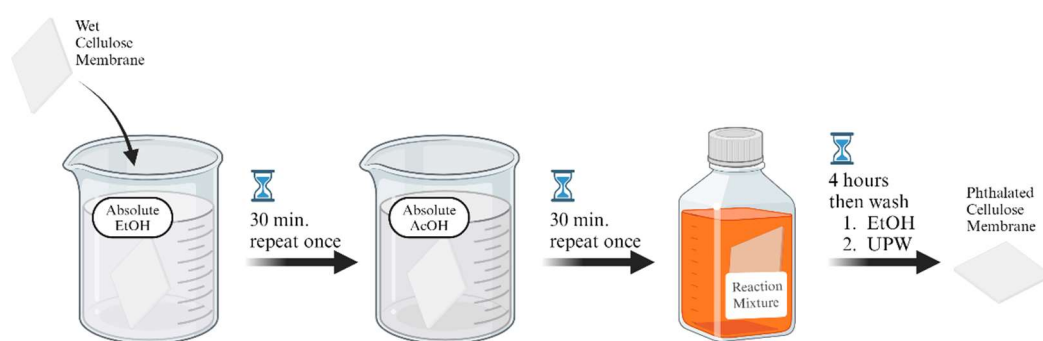
Figure 2.4 Preparation of Phthalated Cellulose Membranes

The membranes so prepared are detailed in Table 2.2.

Table 2.2 Preparation of Support Membranes

Membrane	Material	NIPS in RO	Alkaline Hydrolysis	Anhydride Treatment
CA15	Cellulose Acetate	+	-	-
RCA15	Cellulose	+	+	-
PRCA15	Cellulose Phthalate with low DS	+	+	+
CA12-UPW8	Cellulose Acetate	+	-	-
RCA12-UPW8	Cellulose	+	+	-
PRCA12-UPW8	Cellulose Phthalate with low degree of substitution	+	+	+
PES15	Polyether Sulfone	+	-	-

2.4 Cellulose Nanocrystal Preparation

Cellulose nanocrystals were prepared by the acid hydrolysis of cotton linter cellulose. The cotton linter cellulose in question was first dried at 80°C for two days and then stored under reduced pressure to eliminate moisture content. In this procedure, 150mLs of sulfuric acid was slowly added in portions with stirring to 80mLs of UPW in a three-neck round bottom flask equipped with a Dimroth condenser and stirred in a water bath heated to 45°C for at least 30 minutes. Meanwhile, 28.8 grams of cotton linter cellulose was weighed and hydrated with 58 mL of UPW in a one-liter beaker.

With strong and careful stirring with a glass rod, the warm acid mixture was mixed in with the cellulose paste. A dropper was used to wash down the walls in case there were cellulose clumps stuck to the sides of the beaker. The magnetic stirrer in the round bottom flask was also added and the beaker containing the cellulose–acid mixture was moved to the water bath. This mixture was continuously stirred at 45°C for 30 minutes to complete the acid hydrolysis. Once the reaction was complete, it was quenched with 700mLs of ice-cold UPW poured in at once and stirred.

The cellulose nanocrystal suspension so obtained was then allowed to settle at room temperature. The supernatant was removed every 24 hours with a syringe and replaced with UPW, the mixture was then stirred. The supernatant removed and replaced per day was around half the total volume. After 4 days, most of the acid was removed and the solution was dilute in sulfuric acid (<2 wt. %). The mixture was filled into dialysis tubes previously washed with UPW and exhaustively dialyzed against UPW.

After dialysis, the cellulose nanocrystal (CNC) suspension was transferred to glass bottles and stored in the fridge. Using dynamic light scattering (DLS), the hydrodynamic radius and zeta potential of the nanocrystals were measured. The concentration of the suspension was quantified with a Shimadzu MOC63u moisture analyzer. The procedure of CNC synthesis is detailed in Figure 2.5.
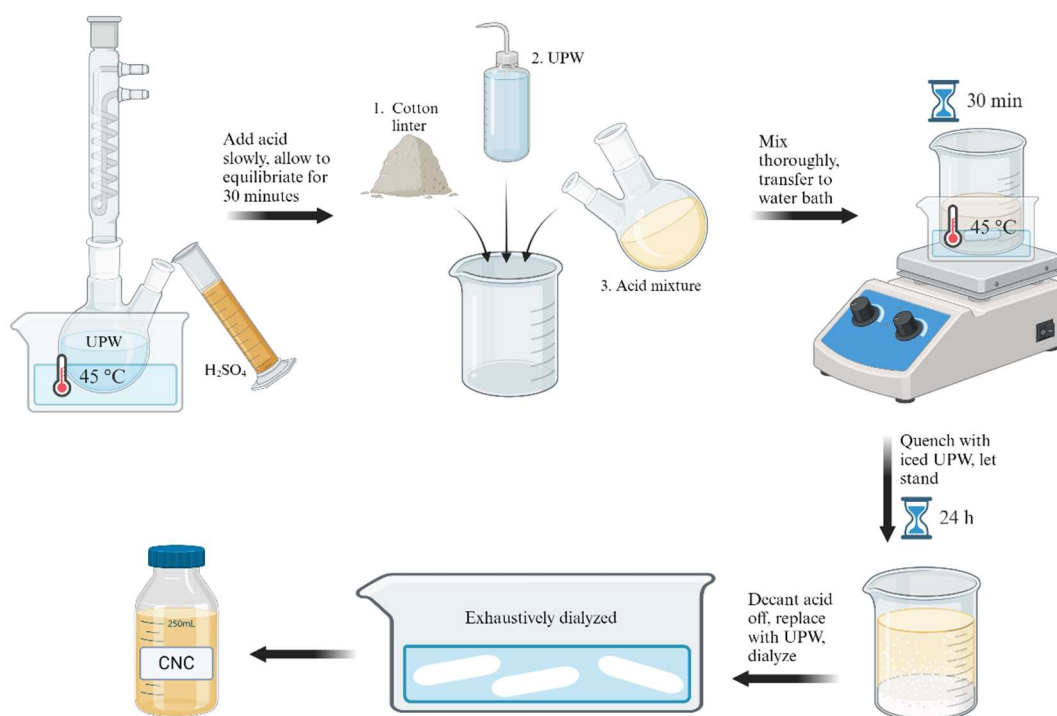
Figure 2.5 CNC Synthesis

2.5   Chemical Modification of Cellulose Nanocrystals

2.5.1   TEMPO Oxidation

CNC suspensions with known concentration were treated with hypochlorite in the presence of catalytic amounts of bromide and 2,2,6,6-tetramethylpiperidine N-oxide (TEMPO) to oxidize hydroxymethyl groups present on their surfaces to carboxylic acids (76). In this process, 29.5mg TEMPO, 324mg NaBr, and 6 grams of 12% NaOCl (or an equivalent volume of less concentrated solution) were added to the CNC suspension. The amounts of chemicals detailed are for the basis of 1g solids contained in the CNC suspension to be modified. TEMPO was dissolved in a minimal amount of UPW prior to addition. The reagents were added in the order of solid NaBr, then TEMPO solution, and finally NaOCl solution. A dilute (0.5M) solution of NaOH and a dropper were kept at ready for adjusting the pH.

34

A pH probe was dipped into the stirring mixture of CNC, NaBr, TEMPO, and NaOCl. During the reaction time of 3 hours, pH was checked and adjusted to the range of pH 10.0-10.5. After 3 hours had been elapsed, 3.7mLs of EtOH was added to destroy remaining NaOCl via the haloform reaction (124). Enough fuming HCl was added to bring the pH below 1.5 in order to protonate the newly formed carboxylate groups. The mixture was then filled into dialysis tubes previously washed with UPW and exhaustively dialyzed against UPW.

The TEMPO-CNC suspension so obtained was placed in glass bottles and stored in the fridge. The concentrations of sulfate and carboxylate groups were quantified using conductometric titration, and the solids content was measured using the moisture analyzer.

2.5.1.1 Iodometric Quantification of Hypochlorite

As hypochlorite solutions decompose into salt and chlorate during storage (125), a method was devised to quantify hypochlorite concentrations. In this procedure, 700 mg of sodium thiosulfate pentahydrate was dissolved in 100 mL of UPW. A 50-mL burette was loaded with this solution, purged to remove air, and loaded again. 250 μL of hypochlorite solution to be tested was diluted in 50 mL of UPW. 0.25 g of potassium iodide (excess for less than 20 wt. % active chlorine) was added with mixing. 0.25 mL of fuming HCl was also added, followed by enough cold-soluble dextrin as the indicator (126). The titration was started immediately. Iodine liberated from iodide in the acidic, oxidizing media was titrated against thiosulfate to afford iodide and tetrathionate (127). Hypochlorite concentrations were calculated as C_{NaOCl} (M) = 0.05641 * $V_{titrant}$ (mL).

The reactions taking place in this titration are detailed below:

$$OCl^- + 2H^+ + 3I^- \rightarrow Cl^- + H_2O + I_3^-$$

$$I_3^- + 2S_2O_3^{2-} \rightarrow 3I^- + S_4O_6^{2-}$$
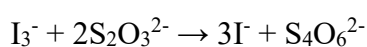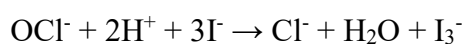
2.5.2   Cationization

CNC particles were rendered cationic through the concomitant removal of negatively charged groups (128) and the installation of positively charged ones. This is accomplished through a reaction with alkali and glycidyltrimethylammonium chloride (GTMAC) (74).

In this process, CNC suspensions were concentrated using membrane filtration using ultrafiltration (UF) membranes. A transmembrane pressure (TMP) of 1 bar was applied and the dead-end filtration cell was stirred at the highest rate practicable. Suspensions of 7.8 wt. % CNC content were obtained.

A concentrated solution of NaOH was prepared by dissolving 2.5g NaOH in UPW such that the final volume was 3.5 mL at room temperature (71.43 wt./vol. % NaOH). After this solution cooled down, enough was measured volumetrically and added to the CNC suspension to reach a NaOH concentration of 7 wt./vol. %. The CNC–alkali mixture was homogenized by drawing it in a syringe and passing it through the needle. This mixture was magnetically stirred at room temperature for half an hour, during which time sulfate groups were removed from the CNC particles.

A water bath at 65°C was kept ready. After 30 minutes had been elapsed, enough GTMAC to provide 3 moles GTMAC per mol anhydroglucose present in CNC was added. The amount added is:

$$V_{GTMAC}\ (mL) = \frac{C_{CNC}\left(\frac{g}{mL}\right) * V_{CNC}\ (mL) * 3\frac{mol\ GTMAC}{mol\ anhydroglucose}}{162.141\frac{g}{mol\ anhydroglucose} * Assay_{GTMAC}} * 134.21\frac{mL}{mol\ GTMAC}$$

The mixture was again homogenized by drawing it in a syringe and passing it through the needle. Then, the mixture was stirred in the water bath for five hours. The reactions taking place are detailed in Figure 2.6.
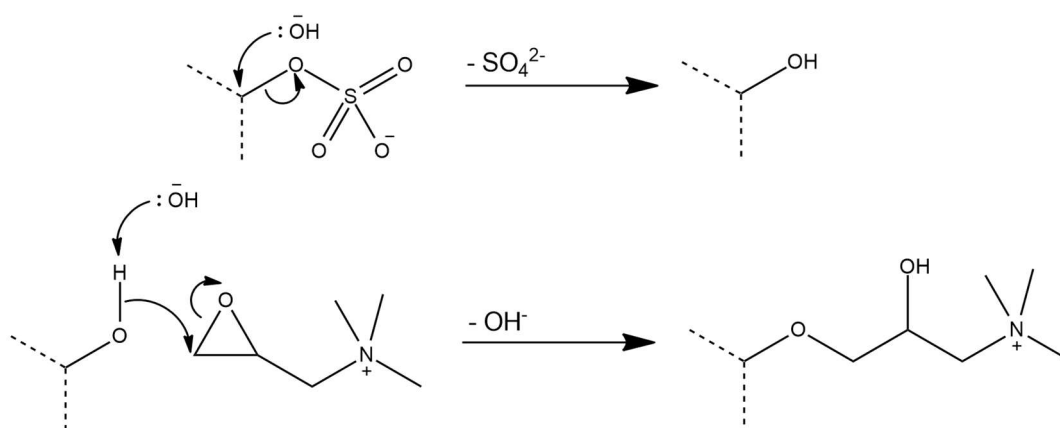
Figure 2.6 Proposed Desulfation and Epoxide Addition Reactions

After the reaction was complete, the reaction mixture was diluted, filled into dialysis tubes previously washed with UPW, and exhaustively dialyzed against UPW.

The CNC+ suspension so obtained was placed in glass bottles and stored in the fridge. The solids content was measured using the moisture analyzer.

2.5.2.1   GTMAC Assay Calculation

The reagent GTMAC was found to decompose under storage. Structures of possible decomposition products are given in Figure 2.7. Therefore, the assay of this reagent must be quantified before synthesis.
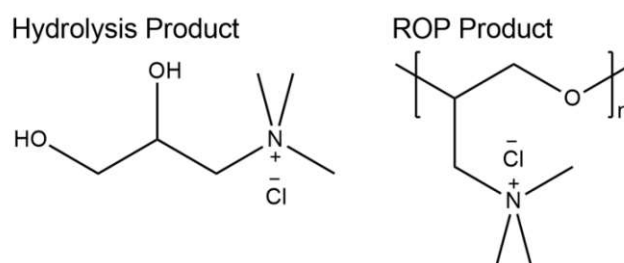
Figure 2.7 The decomposition products of GTMAC

A titration method sensitive to epoxide groups was devised. Sulfite attacks epoxide groups and liberates one equivalent of hydroxide (129). The hydroxide is then titrated against KHP. In this procedure, a solution of 25 mmol potassium metabisulfite (excess) and 50 mmol KOH was prepared in 75 mL of UPW, to yield a potassium sulfite solution. One drop of phenolphthalein in EtOH was added and the pH was adjusted using excess metabisulfite until the solution had a very faint pink color. 4 grams of GTMAC were weighed and added to the solution at once, which quickly turned pink. The beaker was covered with parafilm to limit carbon dioxide dissolution. As quaternary ammonium groups are prone to elimination in basic media (130), titration using concentrated KHP solution was started immediately. The endpoint was reached when the solution was colorless for 10 minutes. The amount of KHP consumed was used to calculate the GTMAC assay with $N_{KHP} = N_{GTMAC}$.

The reaction taking place in this titration is depicted in Figure 2.8.
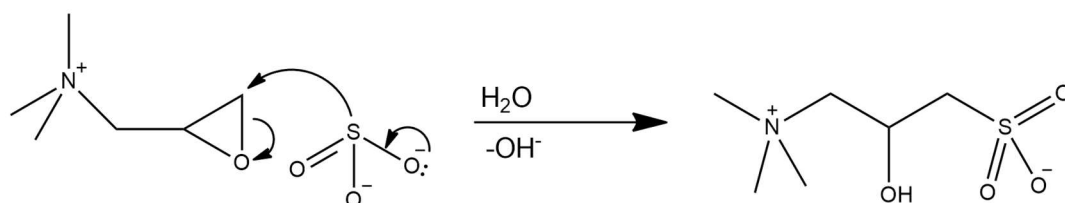
Figure 2.8 Reaction of GTMAC with sulfite

2.6   Preparation of Membranes via LbL Assembly

2.6.1   Preparation of Polymer Solutions and Nanoparticle Suspensions

Polyelectrolytes and nanocellulose materials (CNC, CNC+ or CNF) used for coating membranes were dissolved or suspended in UPW at a final concentration of 0.1 g/L. If necessary, pH adjustment was done with dilute (10mM) NaOH or HCl. Nanoparticle suspensions were homogenized using the ultrasonic probe BANDELIN SONOPULS mini20. For this purpose, an appropriate volume of concentrated nanoparticle suspension was diluted with UPW in a glass vial. The final volume of 25 mL was treated with the ultrasonic probe at 80% amplitude and 0.03 s pulse length for 10 minutes. Then, the contents of the vial were added to a volumetric flask, followed by water used to wash the vial, and topped off to the desired volume. When salts were to be added to coating solutions, they were first dissolved in UPW so that nanoparticles were not aggregated by transient high salt concentrations.

2.6.2   LbL Assembly of Selective Layers

After support membranes were fixed into Amicon dead-end filtration cells, they were coated using two distinct methods. The first method expressed as stationary coating, involved submerging the membrane in the appropriate coating solution for 15 minutes and then washing excess substances away. In the second method, expressed as transmembrane pressure (TMP) driven coating, the coating solutions were filtered through the membrane at 1 bar TMP until a desired volume of permeate was collected. The amount of permeate collected was 10 mL when an Amicon 8050 dead-end filtration cell of 50 mL holdup was used. This amount was scaled according to membrane surface area in the case larger dead-end filtration cells were used to obtain larger coated membranes. The surface areas and the amounts of permeate drawn for coating are available in Table 2.3.

Table 2.3 Active Membrane Surface Areas and Permeate Volumes Drawn

Dead-End Cell	Active Surface Area	Permeate Drawn per Layer
Amicon 8010	4.1 cm^2	3 mL
Amicon 8050	13.4 cm^2	10 mL
Amicon 8200	28.7 cm^2	21.5 mL
Amicon 8400	41.8 cm^2	31 mL

In both methods, excess coating material was removed from the surface by first swirling the cell twice with UPW and dumping out the contents, and then stirring under fresh UPW at 200 rpm for two minutes.

Coated membranes that showed promising separation performance, and which were investigated thoroughly are listed in Table 2.4.

Table 2.4 Membranes Made via LbL Assembly

Support	Polyanion	Polycation	Bilayers	[NaCl]	Denoted as
PRCA-15	PAA 1.8kDa	CNC+	4	None	CCM-1.8
PRCA-15	PAA 250kDa	CNC+	4	None	CCM-250
PES-15	PAA 1.8kDa	CNC+	4	None	CPM-1.8
PES-15	PAA 250kDa	CNC+	4	None	CPM-250
PRCA12-UPW8	CNC (CNF base coat)	CNC+	4	None	ACM-0S
PRCA12-UPW8	CNC (CNF base coat)	CNC+	4	5mM	ACM-5S
PRCA12-UPW8	CNC (CNF base coat)	CNC+	4	50mM	ACM-50S

Where CCM: coated cellulose membrane, CPM: coated PES membrane, ACM: all-cellulose membrane, 0S: zero salt, 5-50S: 5 or 50 mM salt.

2.7 Estimation of the Surface Charge of the Membranes

2.7.1 Dynamic and Electrophoretic Light Scattering

The hydrodynamic sizes of nanoparticles were measured using the device Malvern Zetasizer Ultra Pro using dynamic light scattering (DLS). Electrophoretic light scattering (ELS) mode of the same device was utilized to measure zeta potentials. In both techniques, a sample liquid is exposed to a laser light beam and scattered light is picked up by detectors.

Scattering in the same direction as the incident beam is called forward scattering and is very sensitive to larger particles. Scattering in the opposite direction is called back scattering and scattering with right angles is called side scattering. The software Malvern ZS Xplorer has a multiple angle DLS setting called MADLS, which processes data from all three scattering angles and yields an accurate combined result. This mode was used when the sample was compatible with the DTS0012 plastic cuvettes transparent on all four sides. As organic solvents had to be placed in glass cuvettes instead, and as these cuvettes had frosted sides, only back-scatter measurements were taken.

Dynamic light scattering technique observes the Brownian motion of particles under random collisions with the diluent molecules. This motion is used to infer the size of the particles. Electrophoretic light scattering observes the motion of particles under an applied electric field to gain insight about their charge at the slipping plane, which is termed as zeta potential.

The size data obtained via dynamic light scattering does not correspond to the exact dimensions of the particles if the particles are not spherical. However, the data obtained is still used as a measure of particle size for non-spherical particles such as dissolved polymers.

2.7.2　Dye Sorption Tests

The zeta potentials of membrane samples were qualitatively inferred by dye sorption tests. In this procedure, membranes that underwent different treatments were cut to the same size and submerged in equal volumes of dye solutions of known absorbance. The dyes used were positively charged (crystal violet, CV) or negatively charged (brilliant blue R, BBR). The chemical structures of these dyes are available in Table 2.8. After letting the samples equilibrate with the solution, absorbances were measured again. As dye molecules were attracted to surfaces of opposing charge and are sorbed upon contact, the amount of dye sorbed gives an understanding of the magnitude of membrane charge.

Transient dye sorption tests were done to observe the time dependent behavior of membranes during sorption. In these experiments, the membranes were fixed in tall dead-end filtration cells and the cells were filled with dye solution. The dye used had an opposite electric charge (positive) to the membrane (negative). The cells were stirred to keep the contents uniform in composition, and the absorbance was measured in short time intervals. Measured samples were poured back in the cell so as to have a valid material balance. The amounts withdrawn (1mL) were negligible compared to the volume of dye solution in the cells (400mL). The amount of dye sorbed by the membrane, as well as the rate of sorption were calculated from the absorbance values.

2.7.3 Conductometric Titration

Charged groups on nanocellulose can be quantified using conductometric titration. The groups in question are sulfate half-ester groups present in acid-hydrolyzed neat CNC (77), carboxylate groups present in TEMPO-CNC (76), and quaternary ammonium chloride groups present in CNC+ (74). The latter can be quantified by titration against silver nitrate, while the former two can be quantified by titration against NaOH. In both methods, the titrant is slowly added in small portions of known volume and the conductivity is monitored. The conductivity is volume-corrected to account for the increasing volume due to titrant addition. This is done by multiplying the conductivity with the ratio of the solution volume to the initial solution volume. The reactions taking place are detailed below:

Sulfate Half-Ester Group Neutralization in CNC and TEMPO-CNC (2.7.3-1):

$$ROSO_3^- + H_3O^+ + Na^+ + OH^- \rightarrow ROSO_3^- + Na^+ + 2H_2O$$

Carboxylate Group Neutralization in TEMPO-CNC (2.7.3-2):

$$RCOOH + Na^+ + OH^- \rightarrow RCOO^- + Na^+ + H_2O$$
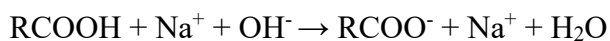
Quaternary Ammonium Group Double Displacement (2.7.3-3):

$$RNMe_3^+ + Cl^- + Ag^+ + NO_3^- \rightarrow AgCl_{(s)}\downarrow + RNMe_3^+ + NO_3^-$$
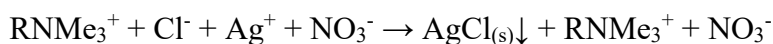
Ions present before and after the addition of the titrant are indicated in Table 2.5. The molar conductivities of these ions at infinite dilution are available in Table 2.6.

Table 2.5 Ions Present Before and After the Addition of the Titrant

Titration for Group	Before Addition	After Addition
Sulfate Half-Ester	H_3O^+	Na^+
Carboxylic Acid	None	$RCOO^-$, Na^+
Quaternary Ammonium Chloride	Cl^-	NO_3^-

Table 2.6 Molar Conductivities of Ions at Infinite Dilution

Ion	Molar Conductivity (S*cm^2/mol)
Hydronium	350
Hydroxide	199
Sodium	50
Silver (I)	62
Chloride	76
Nitrate	61

According to the molar conductivities, the volume-corrected conductivity should decrease when sulfate groups or quaternary ammonium chloride groups are being titrated and increase when carboxylate groups are titrated. Practically, a relatively constant conductivity is observed during the titration of carboxylate groups as these weak acid groups ionize to some degree to afford hydronium ions. In all three titrations, the conductivity is expected to rapidly increase following the exhaustion of titrable groups due to the accumulation of ions present in the titrant. Observed titration curves are available in Figure 2.9.
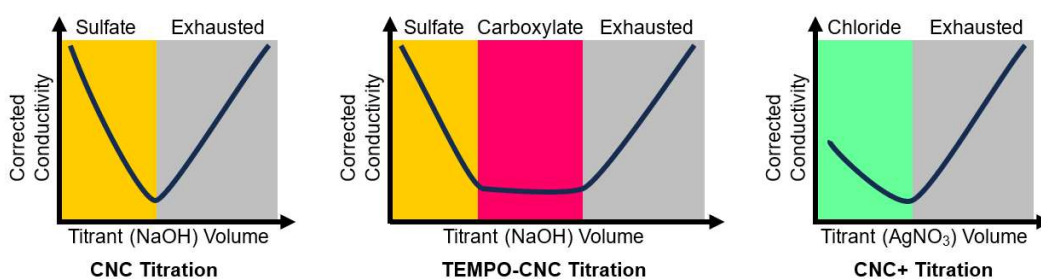
Figure 2.9 Qualitative Titration Curves

Linear trendlines are used to determine the point at which the behavior of the titration curve changes. These titrant volumes are taken as equivalence points and titrable group concentrations are calculated using the relation $N_{titrant} = N_{titrable}$.

2.8   Performance Tests

2.8.1   Molecular Weight Cut-Off Determination

The molecular weight cut-off (MWCO) is an important parameter in UF membranes. MWCO is defined as the lowest molecular weight of a particular substance which will be 90% rejected by the membrane. Example rejection calculations are available in Appendix A. An exemplary MWCO curve is available in Figure 2.10. Although MWCO values change with the nature of the probe molecule used, polyethylene glycol (PEG) and dextran probe molecules of known molecular weight can still be used to gain insight about the structure of the membrane pore structure (131).
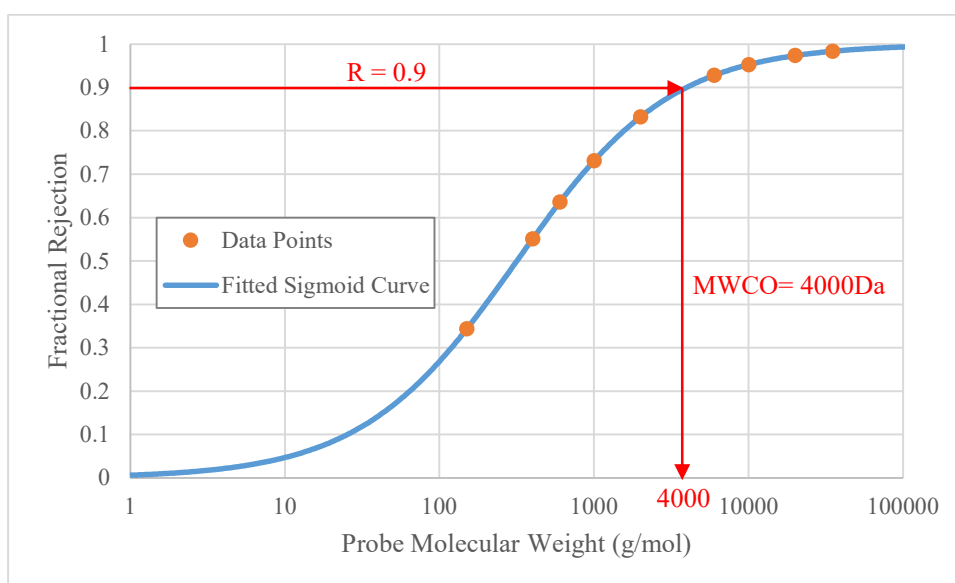
Figure 2.10 Example MWCO Curve Using PEG Probe Molecules of Differing MW

For the curve in Figure 2.10, the MWCO value corresponds to 4000Da.

The MWCO values of the membranes were determined by filtering solutions of polyethylene glycol (PEG) probe molecules of different molecular weights through the membranes. The PEG solutions were prepared by dissolving 0.5 g/L of each probe molecule in water, or in an organic solvent. For solutions in organic solvents (MeOH, DMF, DMSO), mild heating (up to 60°C) and stirring was necessary to ensure complete dissolution of the probe molecules.

PEG solutions were filtered through the membranes in Amicon 8050 dead-end filtration cells for rejection tests in water. The feed solution volumes were 50mL. A TMP of 0.2 bar was applied for filtrations in the aqueous environment. A stirring rate of 500 rpm was applied. Fixed, appropriate volumes (e.g. 2mL, 3mL) of permeate were drawn during the filtration, and the liquid flux was continuously monitored. A total of 3 or 5 permeate samples were taken. Samples were obtained from the feed solution, each of the permeate samples, and the retentate solution left in the cell after filtration. These samples were filled into 1.5 mL GPC sample vials and stored in the fridge until analyzed to prevent microbial contamination.

Organic solvent filtrations were conducted in the same manner but with a few differences: a solvent-resistant stainless steel dead-end cell Sterlitech HP4750 was used. A TMP of 1 bar was applied and the cell was stirred at 400 rpm. Feed solutions of 25 mL volume were used and permeate volumes of 1 mL were drawn. Another difference in methodology was purging the cell: as the Sterlitech HP4750 cell has a larger dead volume in the permeate spout (1mL) compared to the Amicon 8050 cell (0.5mL), the first 1 mL of the first permeate samples were discarded.

The stability of the membranes in organic solvents was checked by performing rejection tests repeatedly, while the membrane remained submerged in the solvent in between tests. For MeOH, rejection tests were repeated after one week. For DMSO and DMF, rejection tests were repeated on day 1, 2, 3, 5 and 7 measured from the moment the membrane was first solvent-exchanged (removed from aqueous environment, submerged in solvent and washed with solvent until no water remained).

2.8.1.1   Checking for Concentration Polarization

During membrane filtration, some of the solutes in the feed solution are expected to be rejected by the membrane. Therefore, these substances remain at the feed side of the membrane and their local concentration increases (2). The presence of this concentration gradient on the membrane surface is termed concentration polarization (CP). As the concentration of rejected solutes is greater at the membrane surface compared to the bulk of the feed, the observed rejection can deviate from the actual value. For this reason, it is desirable to prevent CP by hindering the accumulation of rejected solutes. There are four factors significantly affecting the CP phenomena: membrane flux, boundary layer thickness, intrinsic enhancement ratio, and the diffusivities of solute molecules (2). Among these, two can be controlled with relative ease during membrane filtration. Lowering TMP to have lower membrane flux decreases the rate at which the rejected solute is transported to the surface and lowers CP effects. The boundary layer thickness may be decreased by inducing turbulence via stirring the feed side. Therefore, to lessen the effects of CP phenomena and to obtain reliable rejection measurements, low TMP and high rates of stirring were applied.

The apparent degree of CP was inferred by measuring permeance during all filtrations. This value was divided by either pure water permeance (PWP) or pure solvent permeance (PSP) depending on the solvent choice. Significant deviations of permeance from either PWP or PSP were regarded as signs of concentration polarization and if these deviations were present the experiments were repeated at lower TMP values.

2.8.1.2   Quantification of PEG Concentrations

Analyte concentrations were quantified using Agilent 1260 Infinity II Gel Permeation Chromatograph (GPC) using two PL aquagel-OH columns. The eluent was UPW and its flow rate through the columns was 1 mL/min. The columns and the refractive index detector were operated at 30°C. As the columns could not separate PEG probes that are very close in molecular weight, the probe molecules were grouped in two or three different solutions the compositions of which are described in Table 2.7. GPC signal analysis is detailed in Appendix B.
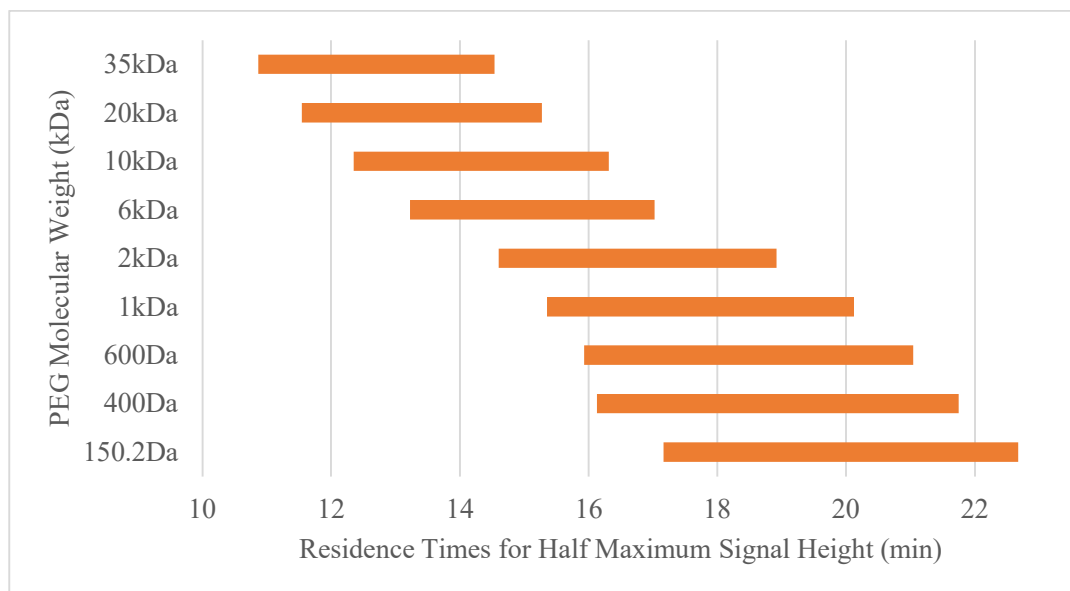

Figure 2.11 Residence Times for Half-Maximum RID Signal Heights

In Figure 2.11, it can be seen that the signals for PEG probes close in molecular weight overlap. For example, running the probes triethylene glycol (150.2Da), PEG 400Da and PEG 600Da simultaneously through the column will yield a single signal which cannot be deconvoluted.

Table 2.7 PEG Solution Compositions

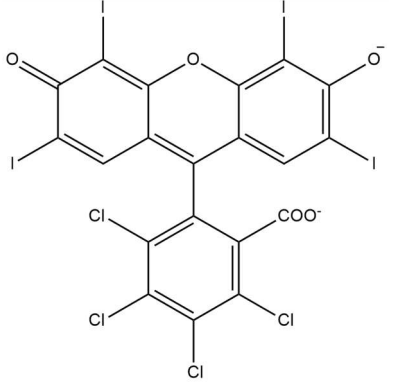| Containing PEG 400Da, 2kDa, 6kDa, 10kDa, 20kDa, 35kDa				
Solution 1	PEG 400Da	PEG 2kDa	PEG 10kDa	PEG 35kDa
Solution 2	PEG 400Da	PEG 6kDa	PEG 20kDa	-
Containing PEG 400Da, 600Da, 2kDa, 6kDa, 10kDa, 20kDa, 35kDa				
Solution 1	PEG 400Da	PEG 2kDa	PEG 10kDa	PEG 35kDa
Solution 2	PEG 600Da	PEG 6kDa	PEG 20kDa	-
Containing TEG, PEG 400Da, 600Da, 1kDa, 2kDa, 6kDa, 10kDa, 20kDa, 35kDa				
Solution 1	TEG (150Da)	PEG 1kDa	PEG 10kDa	-
Solution 2	PEG 400Da	PEG 2kDa	PEG 20kDa	-
Solution 3	PEG 600Da	PEG 6kDa	PEG 35kDa	-
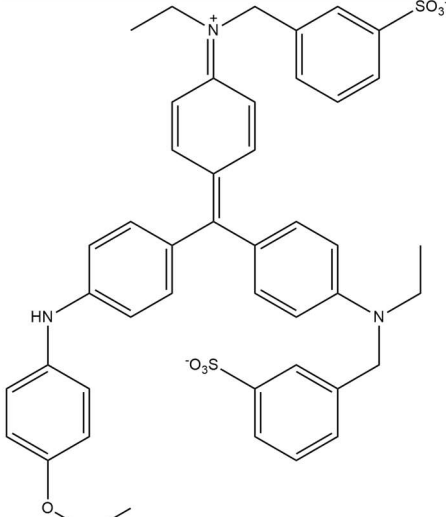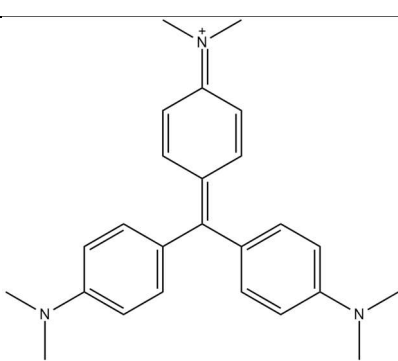
2.8.1.3   Pore Size Determination

PEG probe molecules of differing molecular weights were dissolved in water, MeOH, DMSO and DMF. Dynamic light scattering analysis was performed to obtain hydrodynamic diameters of the probe molecules. Ferry – Renkin equation was then applied to infer the average pore sizes of the membranes.

2.8.2   Dye Filtration Tests

To test the retention of small and charged molecules, dye rejection tests were performed. The dyes in use were rose bengal (RB), brilliant blue R (BBR), and crystal violet (CV). The chemical structures of these compounds are given in Table 2.8. The phenol group in RB is sufficiently acidic with a pK_a of 3.93 (132) to ionize to a significant degree in neutral aqueous solutions and therefore RB has a charge of 2- in solution. BBR has a zwitterionic structure with an overall charge of 1- (133). CV has a charge of 1+ (134). All of the dyes used are small molecules with a molar mass lower than 1 kDa.

Table 2.8 Chemical Structures of the Dye Ions in Aqueous Solution

Dye	Structure	Formula	Charge	Molar Mass
RB		$C_{20}H_2Cl_4I_4O_5{}^{2-}$	2-	971.66Da
BBR		$C_{45}H_{44}N_3O_7S_2{}^-$	1-	802.98Da
CV		$C_{25}H_{30}N_3{}^+$	1+	372.53Da

Feed solutions were prepared by diluting appropriate volumes of concentrated dye stock solutions in the desired solvent (UPW or MeOH) such that the diluted solutions had an absorbance of 1 at a particular wavelength. The wavelengths chosen are detailed in Table 2.9. These wavelengths either correspond to the absorption maxima in the visible region, or the dye is very strongly absorbing at these wavelengths. Dye calibration curves are available in Appendix C.

Table 2.9 Chosen Wavelengths

Dye	Aqueous Solutions	MeOH Solutions
RB	550 nm	558 nm
BBR	595 nm	585 nm
CV	590 nm	585 nm

2.9 Polarized Optical Microscope Imaging

Optical microscope images were obtained using a ZEISS Axioscope A1 microscope equipped with a polarizing filter as well as a camera. These images were used in discerning the colloidal behavior of nanocrystal suspensions.

For obtaining images of flowing liquids, glass capillary tubes of 0.5mm inner diameter were fixed onto glass cover slides at a 45-degree angle and connected to flexible tubes on both ends. One of the ends was connected to a luer-lock syringe tip which in turn was fitted to the tip of a syringe fixed to a NE-300 syringe pump (New Era Pump Systems Incorporated). The cover slide was fixed to the holder of the polarized optical microscope and an appropriate flow rate was applied using the syringe pump. A schematic of this setup is available in Figure 2.12.
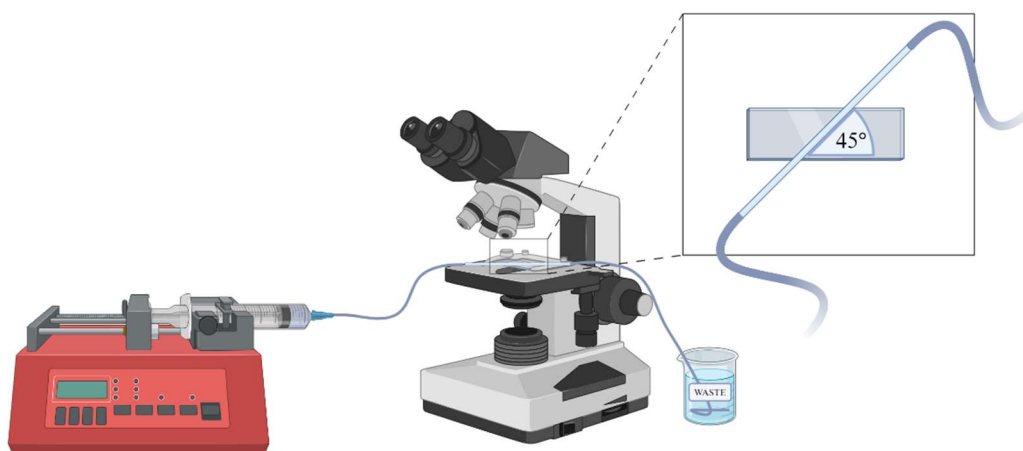

Figure 2.12 Setup Used to Obtain POM Images of Flowing Liquids

2.10   Ellipsometry Experiments

Multilayers were deposited onto silicon wafers and the film thickness was measured using a spectroscopic ellipsometer, Optosense OPT-S6000. Prior to film deposition, silicon wafers were cleaned using the following procedure:

1. The wafers were submerged in absolute acetone at 50°C for 10 minutes.
2. Without rinsing, the wafers were transferred to absolute MeOH at room temperature and were left for 4 minutes.
3. Both sides of the wafers were washed with UPW and dried under nitrogen flow through a capillary tube.
4. The wafers were submerged in concentrated sulfuric acid for 85 minutes.
5. Wafers were taken out and submerged in a sufficiently large quantity (>100mL for 4 wafers) of UPW. Then, both sides were washed with UPW and dried under nitrogen flow through a capillary tube.
6. Wafers were submerged in a sufficient quantity (>40mL for 4 wafers) of freshly prepared 0.25M NaOH for 10 minutes. Then, both sides were washed with UPW and dried under nitrogen flow through a capillary tube.

While it is possible to store the wafers after the fifth step (acid treatment) and to perform the sixth step (base treatment) later, it is not recommended to store the wafers for long periods of time after base treatment. This is because the silica passivation layer on the surface thinned out by base treatment (135) thickens again under exposure to oxygen and moisture for long periods of time (136).

Coating thicknesses were measured by coating the wafers with the desired polyelectrolyte or nanoparticle in an aqueous environment, rinsing in UPW and drying followed by ellipsometry measurements from three different locations on the wafers.

CHAPTER 3

RESULTS AND DISCUSSION

3.1   Nanocellulose Characterization

Cellulose nanocrystals as well as chemical derivatives thereof were characterized using multiple methods. These methods are available in Table 3.1.

Table 3.1 Methods Used for the Characterization of Nanocellulose

Property to be Measured	Experimental Method	Unit of Measurement
Concentration	Moisture Analysis	g/L
Yield	Moisture Analysis	1
pH	pH Probe	1
Mean Hydrodynamic Diameter	Dynamic Light Scattering	nm
Zeta Potential	Electrophoretic Light Scattering	mV
Sulfate Content	Conductometric Titration	mol/kg
Carboxylate Content	Conductometric Titration	mol/kg
Ammonium Content	Conductometric Titration	mol/kg
Surface Charge Density	Calculated from Titration	C/m^2
Mean Particle Charge	Calculated from Titration	1

DLS size and zeta potential distributions are available in Appendix D. Surface charge density calculations are available in Appendix E.

3.1.1　　Properties of CNC

The properties of cellulose nanocrystals obtained via sulfuric acid hydrolysis of cotton linter (CNC) are available in Table 3.2. The titration curve for sulfate content determination is available in Figure 3.1.

Table 3.2 Typical Properties of CNC

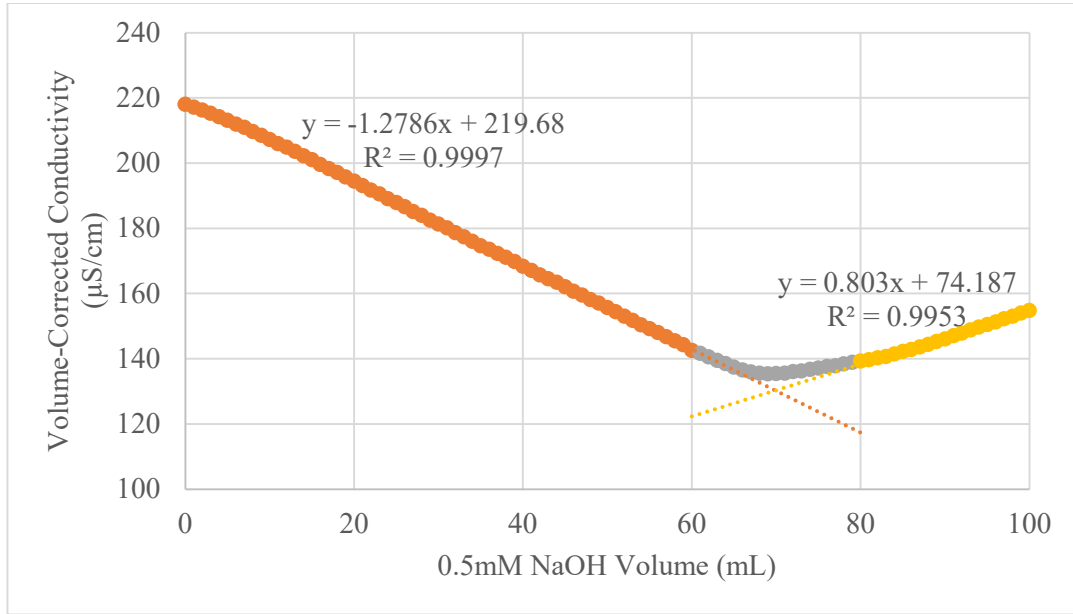| Property	Value
Concentration	10 g/L
Yield on Cotton Linter	19 – 27 %
pH	3
Mean Hydrodynamic Diameter (Intensity Average)	133 nm
Zeta Potential	-54 mV
Sulfate Content	0.241 – 0.350 mol/kg
Surface Charge Density	-0.0812 C/m^2
Mean Particle Charge	-2450

Figure 3.1 Conductometric Titration Curve for Sulfate Content Determination

According to Figure 3.1, the point at which the curve changes behavior is at the titrant volume of 42.35mLs. The mass of CNC in suspension is known and was 0.088 grams for this experiment. Therefore, the sulfate content can be calculated as follows.

$$N_{titrant} = N_{titrable}$$

$$N_{NaOH} = N_{ROSO_3H}$$

$$0.04235L * 0.5mM = 0.088g * C_{sulfate}$$

$$C_{sulfate} = 0.241 \frac{mmol}{g} = 0.241 \frac{mol}{kg}$$

The liquid crystal properties of the CNC suspension produced were also studied. For this purpose, CNC suspension was concentrated to 8 g/L, 16 g/L, or 32 g/L concentration using ultrafiltration at 1 bar TMP and with the highest practicable rate of stirring. After concentration, the suspensions were homogenized using the ultrasonic probe and loaded into the syringe pump. Different shear rates were applied to each suspension and POM images were obtained.
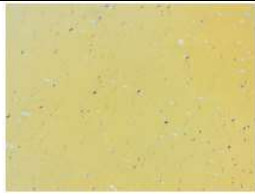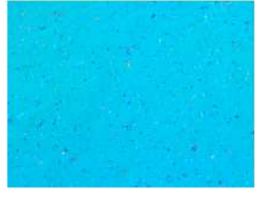
Table 3.3 POM Images of Flowing CNC Suspensions. The diagonal bands represent the flow channel in the capillary. The polarizing and analyzing filters are oriented at 90º angle to each other, blocking light that has not interacted with the birefringent suspension. The flow of the suspension is at 45º angle to both filters.

	CNC Suspension Concentration		
Shear Rate	8 g/L	16 g/L	32 g/L
50/s			
100/s			
200/s			
400/s			
600/s			

The apparent brightness seen in Table 3.3 increases with increasing shear rate and concentration. This brightness is caused by the phenomenon of birefringence, which arises from long-range ordering in colloids. This alignment in the flow direction is caused by the effect of shear stress to the rod-shaped particles and is a common feature in liquid crystals (137). Therefore, CNC particles can be aligned in the flow direction provided that the applied shear rate and the nanoparticle concentrations are sufficient.

CNC suspensions of sufficient concentration are viscous enough to preserve the long-range order and birefringence properties for long periods of time (on the order of hours). This was demonstrated by casting CNC suspensions of 100 g/L concentration on glass slides and observing them under the POM after half an hour. Five images were taken for each sample, and the sample was rotated such that the angle between the polarizing filter and casting direction was 0, 22.5, 45, 67.5, or 90 degrees. The POM images are available in Table 3.4.

Table 3.4 POM Images of CNC Films.

Filter Angle	Film Thickness - Approximate Shear Rate Applied		
	250µm - 200/s	120µm - 420/s	60µm - 830/s
0º			
22.5º			
45º			
67.5º			
90º			

The apparent brightness observed at a 45º angle between the casting direction and the filters indicates that the samples are birefringent. The nematic alignment of cellulose nanocrystals causes this property and its magnitude can be read off the Michel – Lévy interference color chart (138). However, as the films have poor mechanical properties even after coagulation with aluminum chloride, further analysis of their characteristics was not pursued.

3.1.2 Properties of TEMPO-CNC

The properties of TEMPO-oxidized cellulose nanocrystals obtained from CNC are available in Table 3.5. The titration curve for carboxylic acid and sulfate content determination is available in Figure 3.2.

Table 3.5 Typical Properties of TEMPO-CNC

Property	Value
Concentration	10.8 g/L
pH	4
Mean Hydrodynamic Diameter	120 nm
Zeta Potential	-43 mV
Carboxylic Acid Content	0.400 mol/kg
Sulfate Content	0.315 mol/kg
Surface Charge Density	-0.194 C/m^2 (on complete ionization)
Mean Particle Charge	-5840 (on complete ionization)
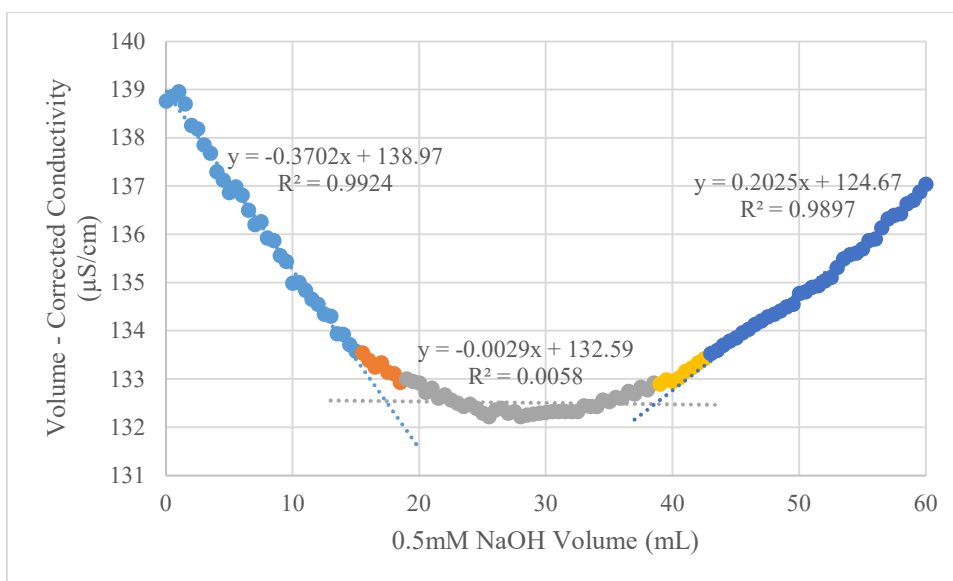
Figure 3.2 Conductometric Titration Curve for Carboxylic Acid and Sulfate
Content Determination

In Figure 3.2 there are two equivalent volumes. The first one at V_1 = 18mL corresponds to the exhaustion of sulfate groups. The second equivalent volume V_2 = 35.6mL corresponds to the exhaustion of carboxylic acid groups. Therefore, the titrant volume used to calculate sulfate content is V_1, and the titrant volume used to calculate carboxylic acid content is $V_2 - V_1$.

Similar to CNC suspensions, TEMPO-CNC suspensions of sufficient concentration are viscous enough to preserve the long-range order and birefringence properties for long periods of time (on the order of hours). This was demonstrated by casting TEMPO-CNC suspensions of 100 g/L concentration on glass slides and observing them under the POM after half an hour. Five images were taken for each sample, and the sample was rotated such that the angle between the polarizing filter and casting direction was 0, 22.5, 45, 67.5, or 90 degrees. The POM images are available in Table 3.6.

Table 3.6 POM Images of TEMPO-CNC Films. The diagonal bands represent the flow channel in the capillary. The polarizing and analyzing filters are oriented at 90º angle to each other, blocking light that has not interacted with the birefringent suspension. The flow of the suspension is at 45º angle to both filters.

Filter Angle	Film Thickness - Approximate Shear Rate Applied		
	250µm - 200/s	120µm - 420/s	60µm - 830/s
0º			
22.5º			
45º			
67.5º			
90º			

Similar to the case with CNC gels, birefringence was also observed for cast films of TEMPO-CNC. These films were crosslinked with silver / persulfate radical oxidation (139) in an attempt to obtain a robust structure but were ultimately deemed unsuitable as standalone membranes due to their poor mechanical characteristics.

On the other hand, films that were cast onto porous supports and subsequently crosslinked could be used as membranes as the support resisted deformation under applied pressure. These composite membranes displayed decent (70% – 75%) rejections of the probe blue dextran 5kDa. This procedure was not investigated further as depositing a cake layer by filtering TEMPO-CNC and stabilization with aluminum chloride yields membranes with superior blue dextran rejection with a more straightforward procedure (69).

3.1.3 Properties of CNC+

The properties of cationized cellulose nanocrystals obtained from CNC are available in Table 3.7. The titration curve for quaternary ammonium content determination is available in Figure 3.3.

Table 3.7 Typical Properties of CNC+

Property	Value
Concentration	14 - 20 g/L
Yield on CNC	90%
pH	10
Mean Hydrodynamic Diameter	188 nm
Zeta Potential	36 mV
Quaternary Ammonium Content	0.160 mol/kg
Surface Charge Density	0.0406 C/m^2
Mean Particle Charge	1230
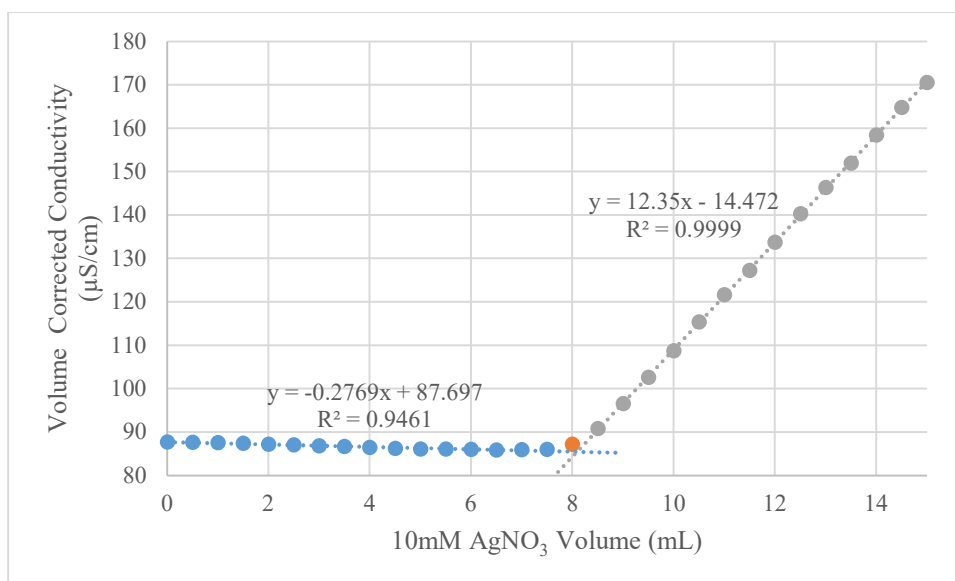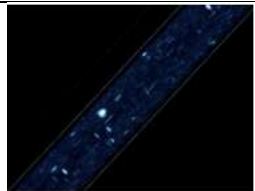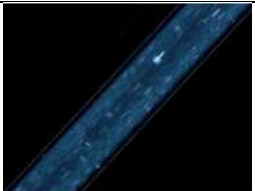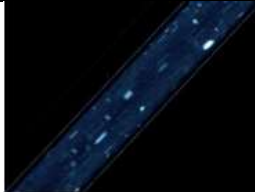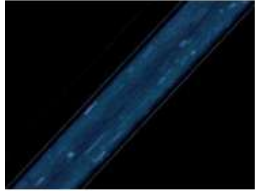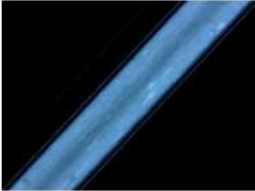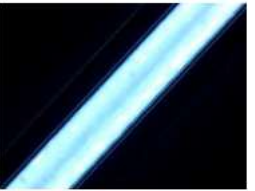
Figure 3.3 Conductometric Titration Curve for Quaternary Ammonium Content
Determination

The colloidal properties of the CNC+ suspension produced were also studied. For
this purpose, CNC suspension was concentrated to 5 g/L, 10 g/L, or 20 g/L
concentration using ultrafiltration at 1 bar TMP and with the highest practicable rate
of stirring. After concentration, the suspensions were homogenized using the
ultrasonic probe and loaded into the syringe pump. Different shear rates were applied
to each suspension and POM images were obtained.

Table 3.8 POM Images of Flowing CNC+ Suspensions. The diagonal bands represent the flow channel in the capillary. The polarizing and analyzing filters are oriented at 90º angle to each other, blocking light that has not interacted with the birefringent suspension. The flow of the suspension is at 45º angle to both filters.

	CNC Suspension Concentration		
Shear Rate	5 g/L	10 g/L	20 g/L
50/s			
100/s			
200/s			
400/s			
600/s			

The apparent brightness seen in Table 3.8 increases with increasing shear rate and concentration. Birefringence displayed by the CNC+ suspension under shear indicates that the nanoparticles can be ordered over long ranges provided that the shear applied and the nanoparticle concentration are sufficient.

3.1.4 Electrostatic Deposition of Nanocellulose Under Flow Conditions

The feasibility of depositing nanocellulose in an aligned fashion was studied by flowing nanocellulose suspensions through capillary tubes previously treated with polycations in order to render them charged. For this purpose, capillary tubes were filled with 0.2g/L BPEI hydrochloride solution at pH 5.5 and let stand for at least 15 minutes. Then, the tubes were thoroughly washed and CNC suspension at various ionic strengths was passed through at different shear rates for 10 minutes. The tube was then washed with UPW and a polycation solution (0.1g/L PAH or PDADMAC) containing variable amounts of NaCl was passed through to yield a bilayer. During this step, the presence of birefringence was checked to see whether a birefringent deposit had formed on the walls of the capillary. As polycation solutions themselves are not birefringent, they represent a blank background. The varied parameters and their values are available in Table 3.9.

Table 3.9 Experimental Parameters for Electrostatic Deposition Under Flow

Parameter	Applied	Result
CNC Suspension Concentration	1, 2, 3.2, 5 wt. %	No Birefringence Observed
Polycation Type	PAH, PDADMAC	No Birefringence Observed
Wall Shear Rate	50, 200, 400, 600/s	No Birefringence Observed
Ionic Strength	0, 5, 50mM NaCl	No Birefringence Observed
Bilayer Number	1 – 10	No Birefringence Observed

Birefringent films were only obtained in one occasion in which the coating liquids 0.1g/L PAH and 5 wt. % CNC inadvertently mixed and formed a gel during the application of the fourth bilayer. The surface deposit formed from CNC / PAH gel was found to be conducive to the deposition of further aligned bilayers. Mean gray values indicative of brightness caused by birefringence are available in Figure 3.4 and clearly support the findings.
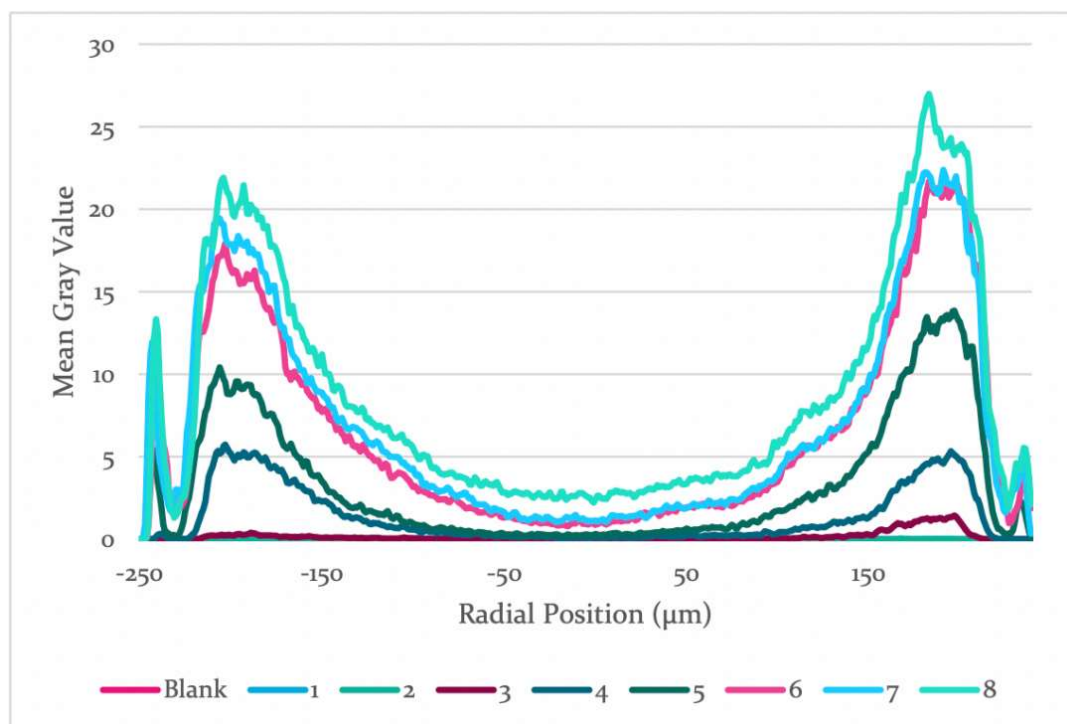
Figure 3.4 Mean Gray Values Measured Across the Capillary Tube for up to 8 Bilayers

These results could not be replicated by applying a primer layer of well-defined PAH / CNC gel. This approach was not pursued further as the in-situ formation of the PAH / CNC gel is not controllable.

In essence, the deposited films could not reliably be made out of aligned nanoparticles. The presence of a deposited film was checked by manufacturing a flow module available in Figure 3.5, and coating cover glasses with the materials.
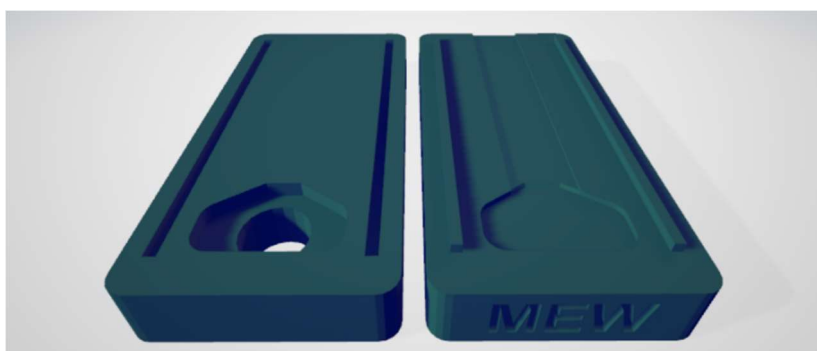
Figure 3.5 Flow Module for Coating Cover Glasses

Although the module was successful in coating cover glasses in layers thick enough to be seen with the naked eye, the films did not display birefringence. These results suggest that electrostatic interaction is the dominant interaction of the particles near the surface, and the nematic ordering formed through the application of shear force is disrupted. One possible explanation for this is that the nanocrystals are more charged towards their ends as the crystal facets have a lower number of sites that can be sulfated compared to free cellulose chains, and the nematic order is broken as the charged ends are attracted to the surface. A schematic of this explanation is available in Figure 3.6.
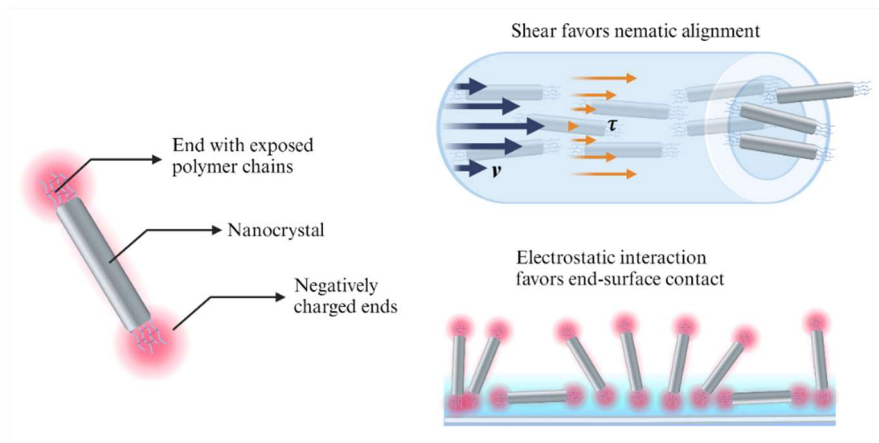
Figure 3.6 Dominant Forces Governing the Alignment of Nanocrystals

As it was found that nanocellulose cannot be deposited in an aligned state from flowing suspensions, all further coating experiments were done with stationary suspensions.

3.2   Properties of the Support Membranes

The support membranes prepared were used in tests to determine pure water permeances (PWP), pure solvent permeances (PSP), and MWCO values.

3.2.1 Pure Water Permeances

The PWP and PSP values of the support membranes are given in Table 3.10. In the case of repeated experiments, the standard deviation is indicated.

Table 3.10 Pure Water Permeances of the Support Membranes

Membrane	PWP (L/hm^{2}bar)
RCA-15	68 ± 6
PRCA-15	69 ± 8
RCA12-UPW8	308
PRCA12-UPW8	316 ± 13
PES15	340

The most permeable support membrane is the one made out of PES polymer, owing to a very rapid phase inversion yielding a highly porous albeit nonselective (MWCO >35kDa) membrane. CA-12 membranes are similarly highly permeable.

It is observed that phthalating the support membrane has little effect on the PWP. PWP is inversely related to polymer content in membranes made out of cellulose acetate and the lowest PWP among the support membranes is displayed by the membrane made from CA-15 dope solution.

3.2.2   Pure Solvent Permeances

The support membrane PRCA-15 was chosen for polyelectrolyte / nanocellulose coating experiments as it could retain and reliably adsorb the coating materials. This membrane was tested in the solvents MeOH, DMSO, and DMF.

The PSP values show a correlation with the inverse of solvent viscosity and it is inferred that the liquid permeates through the support membrane according to the pore-flow model (23). PSP values versus inverse viscosity are plotted in Figure 3.7. The data is available in Appendix F.
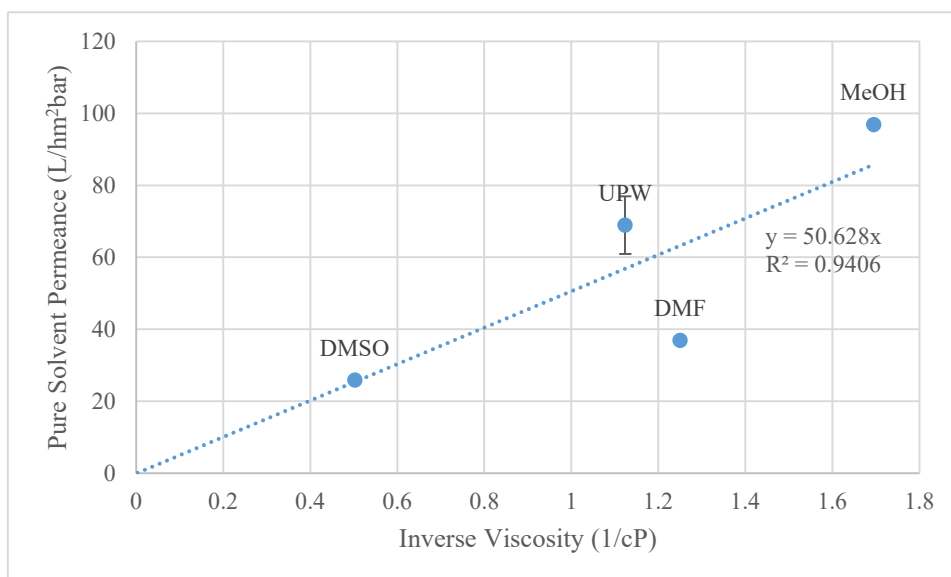
Figure 3.7 Pure Solvent Permeances of PRCA-15 Support Membrane

72

3.2.3   PEG Rejections

The membrane PRCA12-UPW8 showed less than 0.9 rejection for the largest probe molecule, PEG 35kDa.

PEG rejections of the support membrane PRCA-15 were measured in multiple solvents. As PEG 400Da cannot be separated from the DMSO solvent signal, its rejection is not reported. Setting the solvent MW to have zero rejection, MWCO curves were plotted and are available Figure 3.8. Supporting rejection data is available in Appendix F.
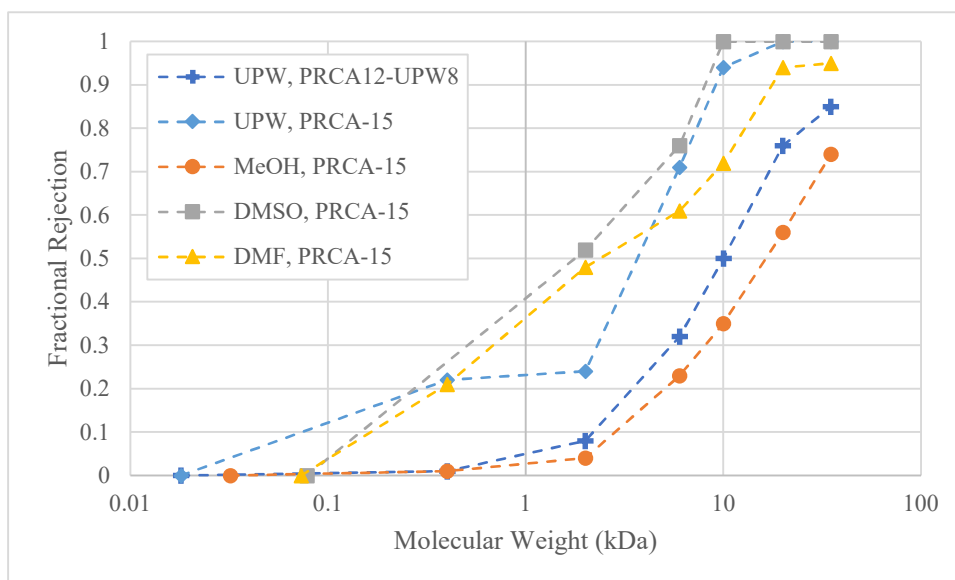
Figure 3.8 MWCO Curves of the Support Membranes, Semi-Log Graph

The MWCO values read off Figure 3.8 are available in Table 3.11. In the case less than 0.9 rejection was seen for even the heaviest probe molecule PEG 35kDa, MWCO was reported as >35kDa.

For the PRCA-15 membrane, when the MWCO values in the solvents UPW, DMF, DMSO and MeOH are compared, the order in which the value decreases is MeOH > DMF > UPW > DMSO as can be seen in Table 3.11. This is influenced by two factors, one being the swelling ratio of the matrix polymer in the solvent. Cellulose swells to a larger extent in the solvents UPW and DMSO compared to DMF and MeOH. This leads to partial closure of the pores as the matrix expands. Another effect is probe – solvent interactions. When PEG interacts with a favorable solvent, it adopts a more expanded conformation and thus has a larger diameter. The hydrodynamic diameter of PEG in different solvents was estimated via DLS to be in the order DMSO ≈ DMF ≈ MeOH > UPW as available in Table 3.15, but the hydrodynamic diameters are close in value. The observed MWCO values are thus justified due to these effects. MWCO values are lower in DMSO and UPW due to membrane swelling. The slightly larger hydrodynamic radii in DMF and MeOH were not found to offset the effect of low swelling in these solvents.

Table 3.11 MWCO Values of the Support Membranes

Membrane	Solvent	MWCO (kDa)
PRCA-15	DMF	18.2
PRCA-15	UPW	9.3
PRCA-15	DMSO	8.3
PRCA-15	MeOH	>35
PRCA12-UPW8	UPW	>35

3.3 Layer-by-Layer Coating Results

LbL deposition of polymer pairs was followed by ellipsometry. Membrane coating was tracked by *in-situ* permeance measurements.

A total of four bilayers were deposited onto membranes which underwent rejection tests. The bilayer number was fixed to facilitate comparison between membranes. The motivation for choosing four bilayers was that additional bilayers caused further lowering of PWP while offering no increase in rejections.

3.3.1 All-Cellulose Coatings

PRCA12-UPW8 support membranes were coated with CNC+ followed by cellulose nanofibers (CNF) as a base coat to provide a robust scaffolding for further layers, followed by CNC+ and CNC bilayers to obtain membranes completely made out of cellulose. The membranes were coated by submerging the support under the desired coating suspension for a duration of 15 minutes and washing off loosely bound polymers for 5 minutes. The effect of salt concentration in the CNC suspensions on the film thickness was examined. The PWP values measured during coating are available in Figure 3.9.
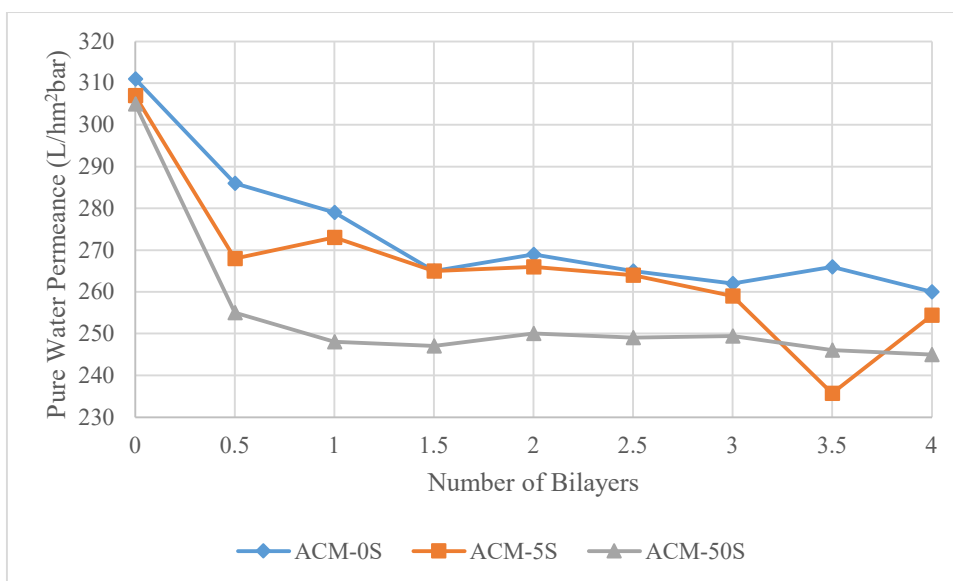
Figure 3.9 PWP Values During Coating of All-Cellulose Membranes. The blue curve represents the membrane coated without the presence of NaCl, the orange curve represents the membrane coated at 5mM NaCl concentration, and the gray curve represents the membrane coated at 50mM NaCl concentration.

As can be inferred from Figure 3.9, PWP values are decreasing as the membranes are being coated.
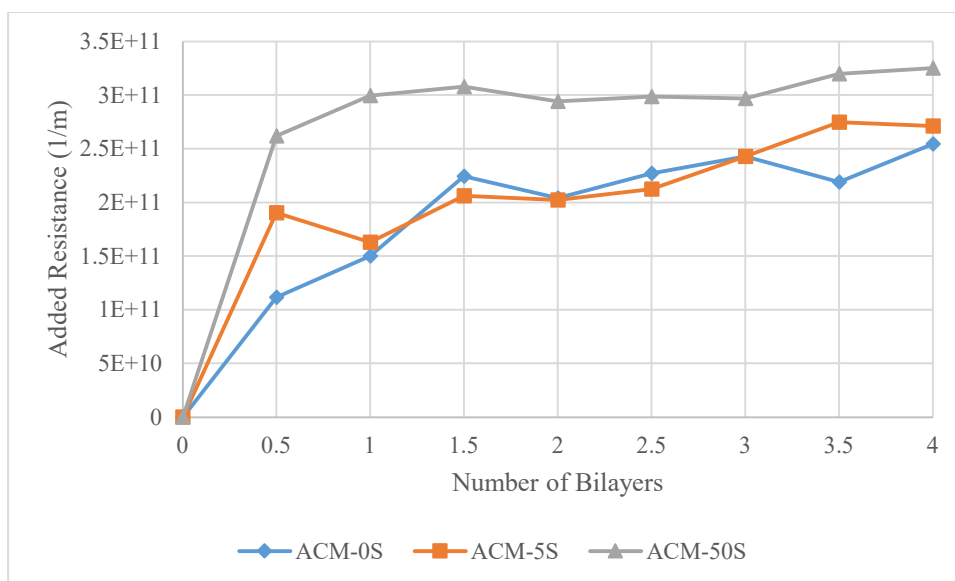
Figure 3.10 Added Resistance Values During Coating of All-Cellulose Membranes. The blue curve represents the membrane coated without the presence of NaCl, the orange curve represents the membrane coated at 5mM NaCl concentration, and the gray curve represents the membrane coated at 50mM NaCl concentration.

Figure 3.10 indicates that the added resistance increases as the membranes are being coated. The added resistance was not lessened to a significant extent when the membranes were washed.

The resistance difference is not significant when salt concentration was varied from 0 to 5mM, but further increasing NaCl concentration to 50mM yielded membranes with higher added resistance. This is because the Debye Length of the nanocellulose particles were shortened, and their charges were screened in the presence of high salt concentrations. This leads to the deposition of thicker layers as the repulsive interaction between like charges are diminished.
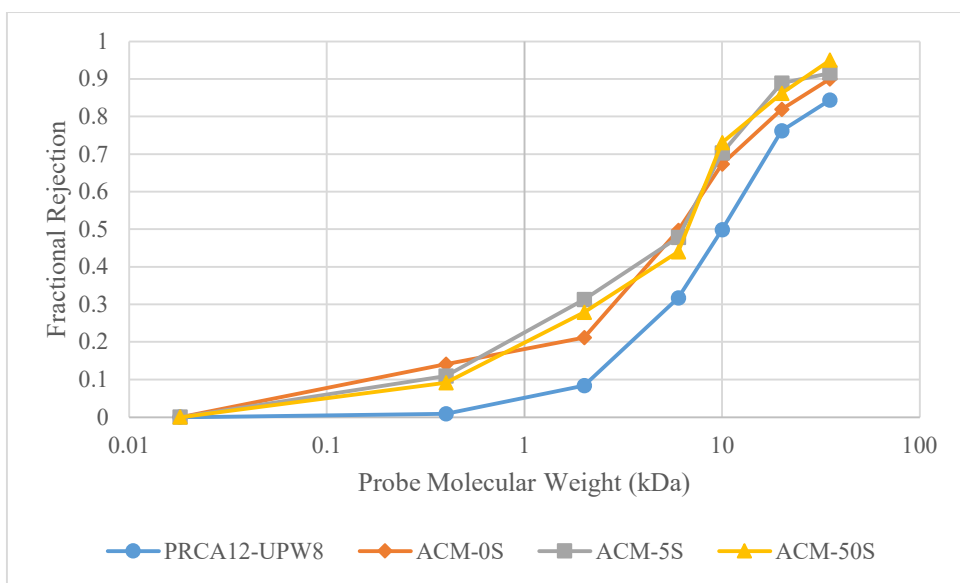
Figure 3.11 MWCO Curves of All-Cellulose Membranes

As inferred from Figure 3.11, all-cellulose coatings have lower MWCO values compared to the support membrane. The MWCO values and pure water permeances are detailed in Table 3.12.

Table 3.12 MWCO and PWP Values of All-Cellulose Membranes

Membrane	PWP (L/hm^{2}bar)	MWCO (kDa)
PRCA12-UPW8	317	>35
ACM-0S	260	35
ACM-5S	254	26.5
ACM-50S	245	26

All of the coated membranes display a similar separation performance. Therefore, ionic strength only has a weak influence on the resistance (20% for ACM-50S vs. ACM-0S) and MWCO values (35% for ACM-50S vs. ACM-0S) of membranes prepared completely out of cellulose. As the properties of these membranes could not be tailored as readily as that of polyelectrolyte coatings and as they are not very selective, hybrid coatings composed of polyelectrolytes and CNC+ were explored.

3.3.2   CNC+ / Polyelectrolyte Coatings

CNC+ and PAA of either 1.8kDa or 250kDa molecular weight were used to coat membranes.

3.3.2.1   Ellipsometry Experiments

Cleaned silicon wafers were first measured with the ellipsometer to determine the oxide layer thickness, which was subtracted from all measurements. The wafers were submerged into 0.2 g/L BPEI solution at pH 5.5 to form a primer layer to support deposition of the further layers. Then, 0.1 g/L solution of PAA with MW of either 1.8kDa or 250kDa and a suspension of 0.1 g/L homogenized CNC+ were deposited in an alternating fashion. After each layer, the film thickness was measured. The evolution of film thickness with respect to layer number is presented in Figure 3.12.
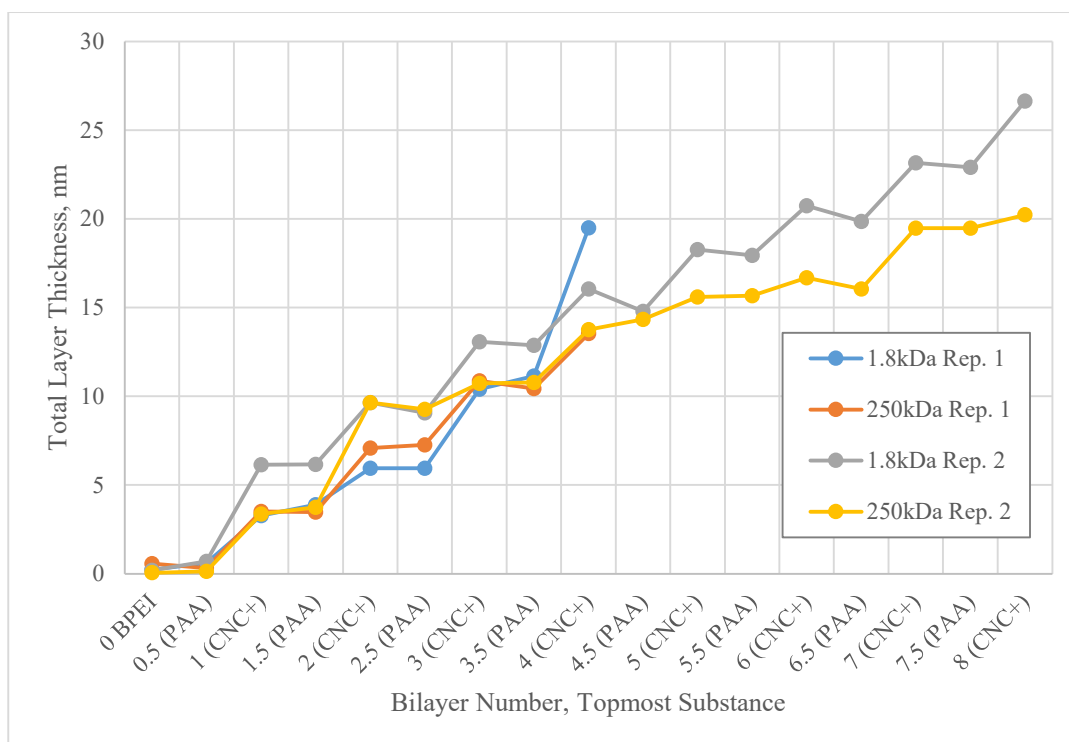
Figure 3.12 Layer Thicknesses for PAA / CNC+ Coatings. Repeated experiments up to 4 or 8 bilayers.

As can be seen in Figure 3.12, the thickness increases with increasing bilayer number, indicating that layers can be formed successfully from PAA and CNC+. The lack of a difference in thickness when comparing PAA-terminated or CNC+ terminated coatings of the same bilayer number suggests that some CNC+ may be swept off the surface during submersion in the PAA solution.

No significant difference was observed in the growth regimes of the two polyelectrolyte / CNC+ pairs, especially when it is considered that the measurement technique is prone to cumulative errors at high thicknesses. Both coatings have a linear growth behavior with PAA 1.8kDa leading to slightly thicker layers as apparent at 8 bilayers.

3.3.2.2   Permeance and Resistance During CNC+ / PAA Coating

CNC+ / PAA coatings were applied using filtration with applied TMP method. This method was chosen over coating via submersion only as the filtration method offers a denser coating with higher probe rejections. A comparison of the two methods is available in Table 3.13.

Table 3.13 Comparison of Membranes Prepared via Different Layer-by-Layer Coating Methods (Stationary Coating Liquid With or Without TMP Applied)

Method	Layers Applied via 15 min Submersion in Coating Liquid	Layers Applied via Permeating Coating Liquid at 1 bar TMP
Polyanion Solution	PAA 1.8kDa 0.1g/L Without pH Adjustment	
Polycation Suspension	CNC+ 0.1g/L Homogenized Without pH Adjustment	
% PWP Change	-6.7%	-17.1%
Resistance Increase	$4.5*10^{11}/m$	$1.1*10^{12}/m$
MWCO	10kDa	6kDa

The CNC+ / PAA pair was chosen over other polyelectrolyte / nanoparticle pairs as the initial tests revealed that CNC+ / PAA selective layers had better separation properties compared to alternative pairs such as PAH / CNC. The comparison was done on the basis of MWCO values (e.g. about 5-6kDa for CNC+ / PAA, and about 8-9kDa for PAH / CNC).

CNC+ / PAA selective layers may have higher probe rejections due to cross-linking between the carboxyl groups in PAA and hydroxyl groups in cellulose. The esterification may be catalyzed by protons donated by PAA itself. Cross-linked PAA and CNC+ may form a more rigid network capable of separating smaller molecules. This type of cross-linkable functionality is absent in other pairs such as CNC+ / PSS (hydroxyl, inert towards sulfonate) or PAH / CNC (hydroxyl, inert towards amine).

Membrane permeance and resistance were tracked during the coating procedure.
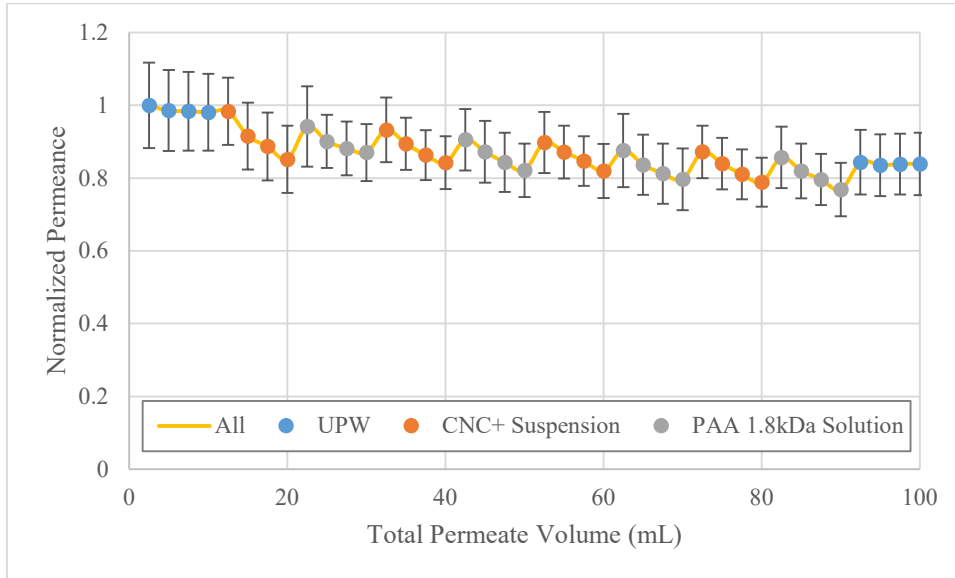
Figure 3.13 Normalized Permeance During Coating for CCM-1.8 Membrane
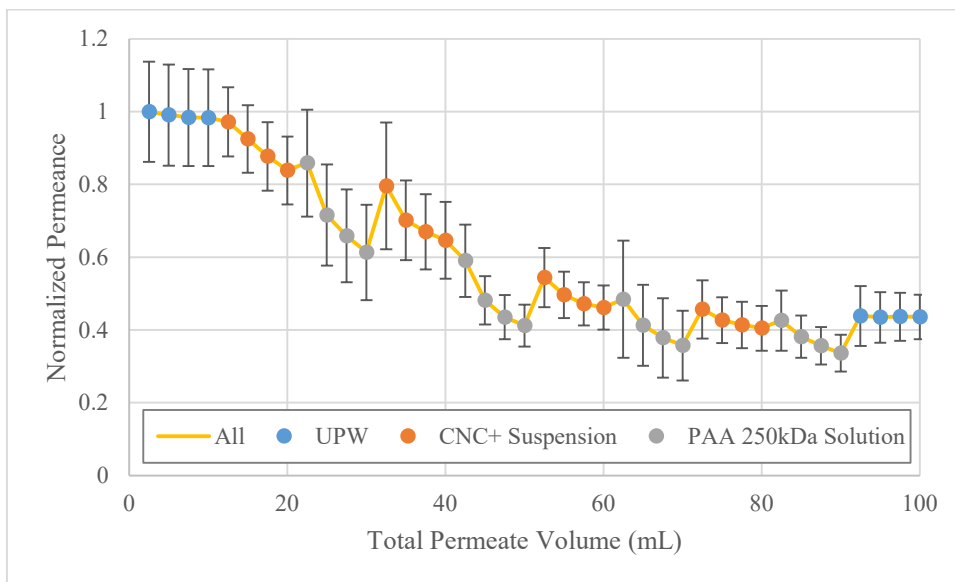
Figure 3.14 Normalized Permeance During Coating for CCM-250 Membrane

Figure 3.13 and Figure 3.14 are composites of 10 different coating experiments. The data points are the mean, normalized values and the error bars reflect the standard deviation. The normalization was done by scaling each data point to the PWP of the support membrane. For these figures, the points indicated as UPW correspond to UPW permeating through the membrane at the start and end of the coating procedure. The points indicated as CNC+ suspension mean that a 0.1g/L suspension of CNC+ is being filtered through the membrane. The points indicated as PAA (MW) solution mean a 0.1g/L solution of either PAA 1.8kDa or 250kDa MW are being filtered through the membrane.

A monotonous drop in permeance is observed while the filtration is taking place. This is inferred to be due to the deposition of solutes present in the coating liquid onto the membrane. A corresponding resistance increase was also observed and is visualized in Figure 3.15 and Figure 3.16.
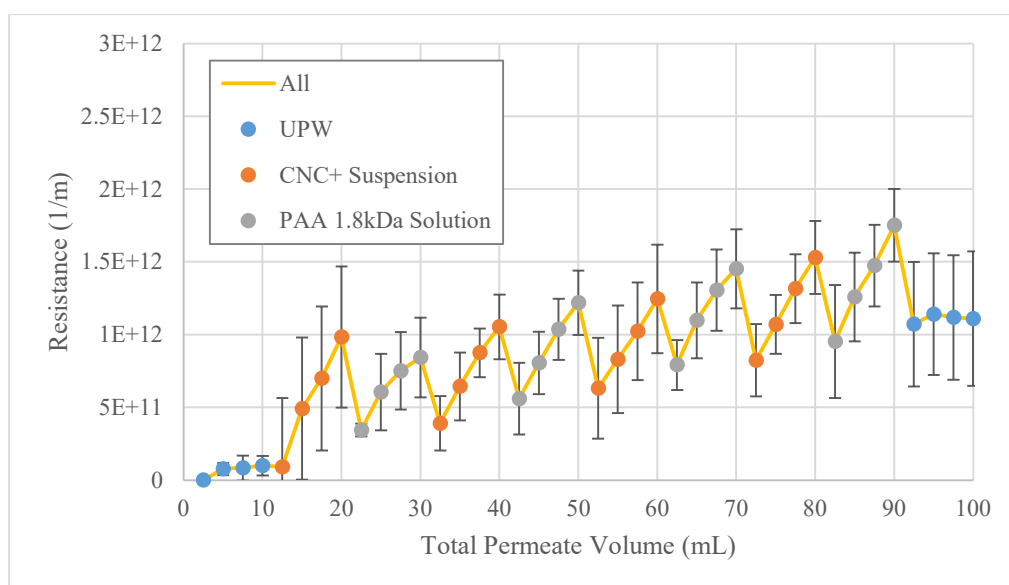
Figure 3.15 Example Added Resistance During Coating for CCM-1.8 Membrane
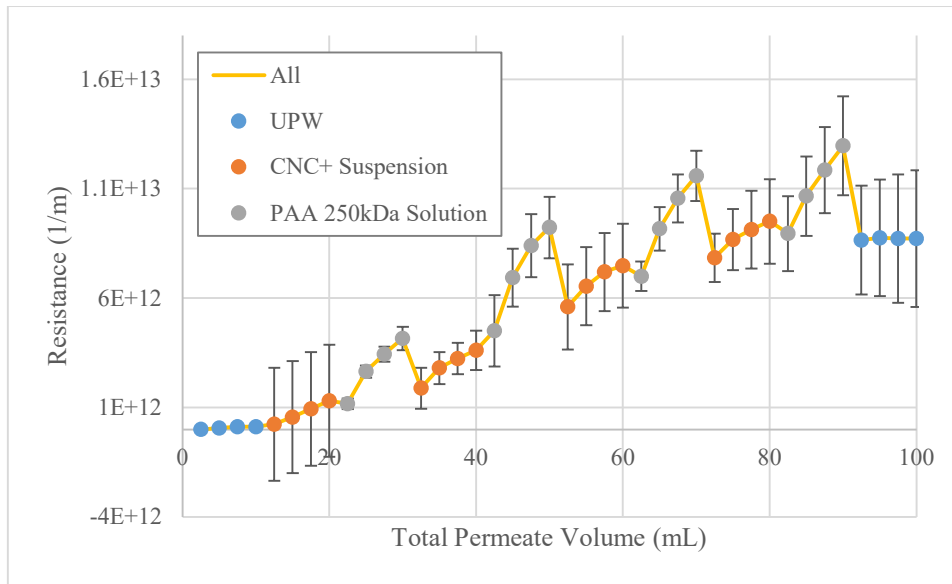
Figure 3.16 Example Added Resistance During Coating for CCM-250 Membrane

Again, the curves are composites of 10 different experiments with the data points indicating the mean and the error bars indicating standard deviation. Permeance is observed to drop monotonously on a bilayer basis, and resistance is observed to increase monotonously on a bilayer basis as further illustrated in Figure 3.17 and Figure 3.18.
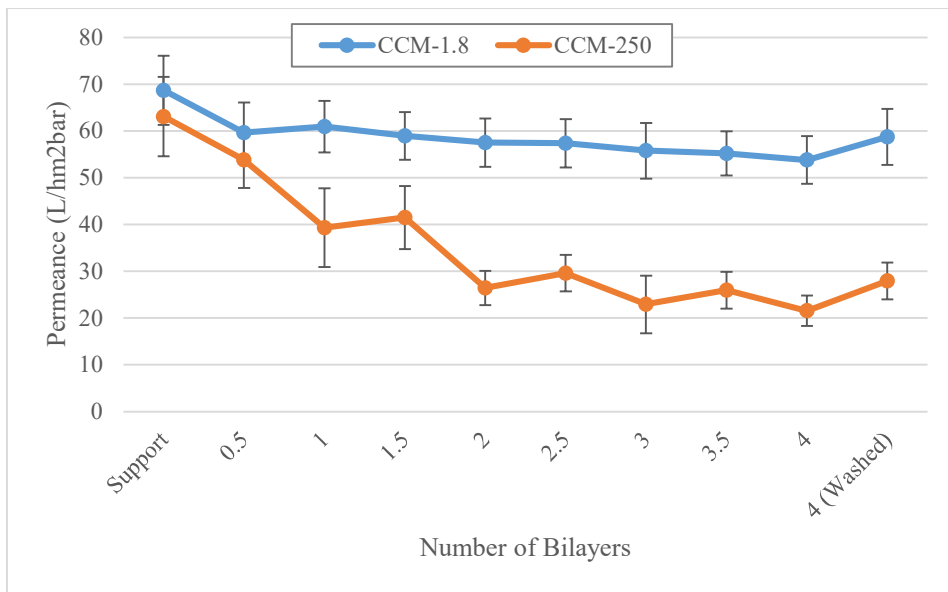
Figure 3.17 Permeance of CCM-1.8 and CCM-250 Membranes During Coating
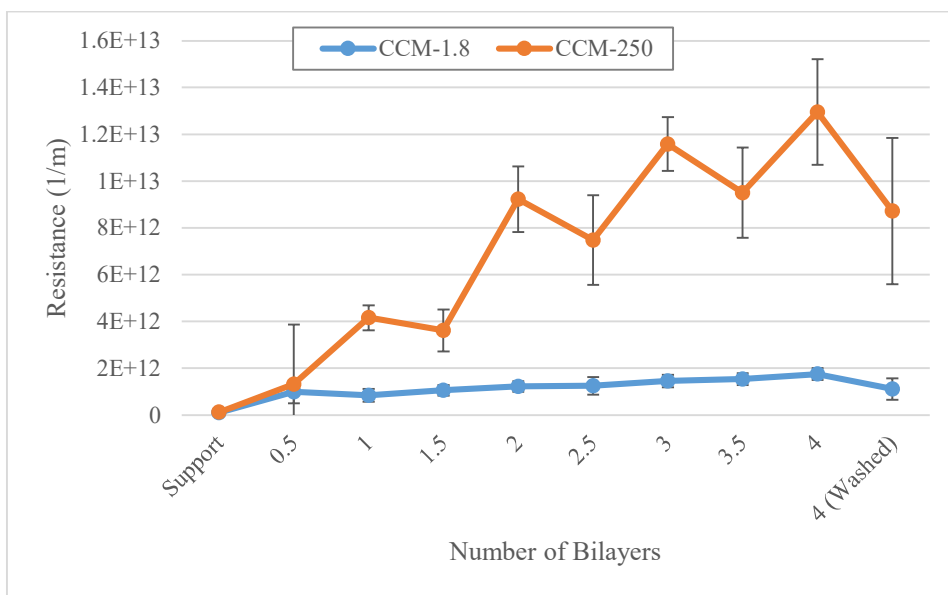
Figure 3.18 Added Resistance of CCM-1.8 and CCM-250 Membranes During Coating

In Figure 3.17 and Figure 3.18, a drop in permeance and an increase in resistance are observed for both membranes as more bilayers are formed. The final data point in each curve shows higher permeance and lower resistance compared to the data point before. This is because excess deposited materials present on the surface at the point labeled as 4 bilayers are washed away.

These results indicate that the materials used during coating are successfully deposited on the surface and adhere robustly. This is evidenced by an increase in resistance and a drop in permeance even after the membrane surface is washed. SEM imaging shows that the surface of the membranes were completely covered, as evidenced in Figure 3.19.
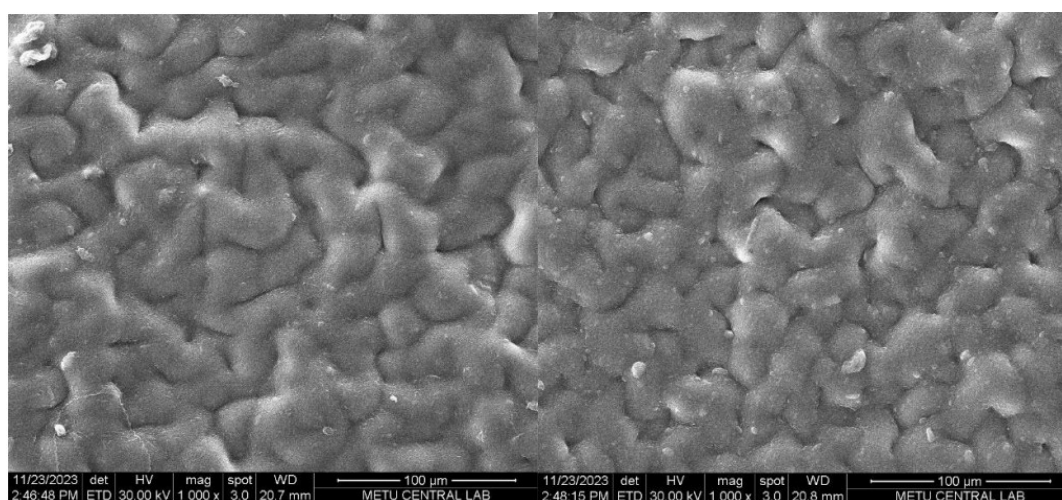
Figure 3.19 Surface SEM Image of the CCM-1.8 (left) and CCM-250 (right) Membranes

The covering thickness is estimated using the images available in Figure 3.20.
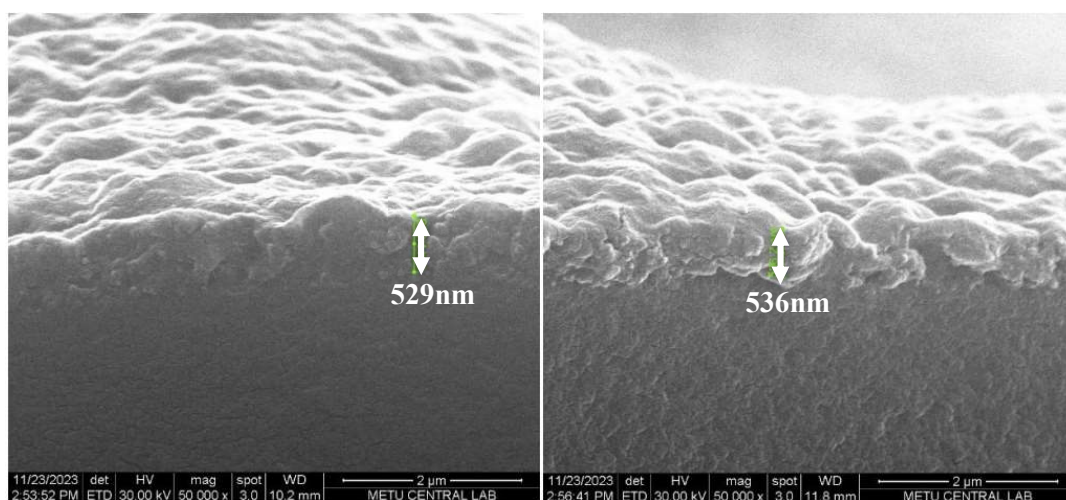
Figure 3.20 Cross-Section Images of CCM-1.8 (left) and CCM-250 (right) Membranes at 50kx Magnification. Arrows represent the thickness of the LbL assembled selective layer.

The dried coating thickness is 500-600 nanometers for both membranes. Precise values cannot be reported as the surface becomes uneven upon drying. The layers coated onto membranes were significantly thicker than the layers observed in ellipsometry.

This discrepancy can be explained by two reasons. The support material is different and significantly charged for membrane preparation due to the chemical modification step done to ensure better layer adhesion. Layers are also deposited via filtration onto membranes, instead of submersion in a coating solution as done for silicon wafers.
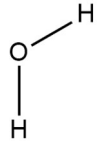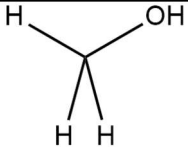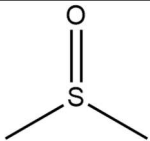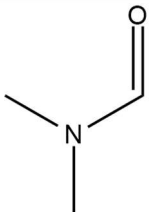
The higher thickness recorded for LbL-modified membranes can be correlated with the deposition of PAA and/or CNC+ not only at the surface but also inside the membrane. The release of previously absorbed PAA and/or CNC+ by the membrane during deposition of the subsequent layers might have resulted in the formation of PAA/CNC+ complexes in the solution and deposition at the surface in the form of aggregates. Furthermore, the greater surface roughness of the membranes compared to silicon wafers might have provided additional area for the deposition of greater amount of PAA and CNC+, resulting in greater thickness.

The higher resistance observed with CCM-250 membrane may be explained by a thicker coating layer or a denser structure. However, SEM imaging shows that the two coatings have roughly the same thickness. The density of the coating layers are also comparable according to MWCO results available in Tables 3.18, 3.19, 3.2, 3.21. Therefore, the proposed explanation is that PAA 1.8kDa diffuses into the CNC+ layers as it is smaller than the MWCO of the membrane. Once inside the CNC+ layer, PAA decreases charge by adsorbing onto CNC+ particles. PAA 250kDa on the other hand is larger than the MWCO of the membrane and forms a separate layer instead of penetrating into the CNC+ layers. Since the separate PAA 250kDa layer represents a polymer gel in between CNC+ layers and hinders flow, higher resistances are observed.

3.3.2.3 Pure Solvent Permeances of CCM-1.8 and CCM-250 Membranes

Tests were done in water as well as in MeOH, DMSO, and DMF. The properties of these solvents are available in Table 3.14.

Table 3.14 Properties of the Solvents Used

Solvent	Structure	Viscosity (25ºC)	Dipole Moment	Dielectric Constant	Molar Volume (25ºC)
UPW		0.890 cP	1.87 D	80.10	18.05 cm^3/mol
MeOH		0.590 cP	2.87 D	32.70	40.45 cm^3/mol
DMSO		1.991 cP	4.10 D	46.68	71.03 cm^3/mol
DMF		0.796 cP	3.86 D	36.71	77.43 cm^3/mol

The results obtained are plotted against inverse solvent viscosity and are available in Figure 3.21 and Figure 3.22.
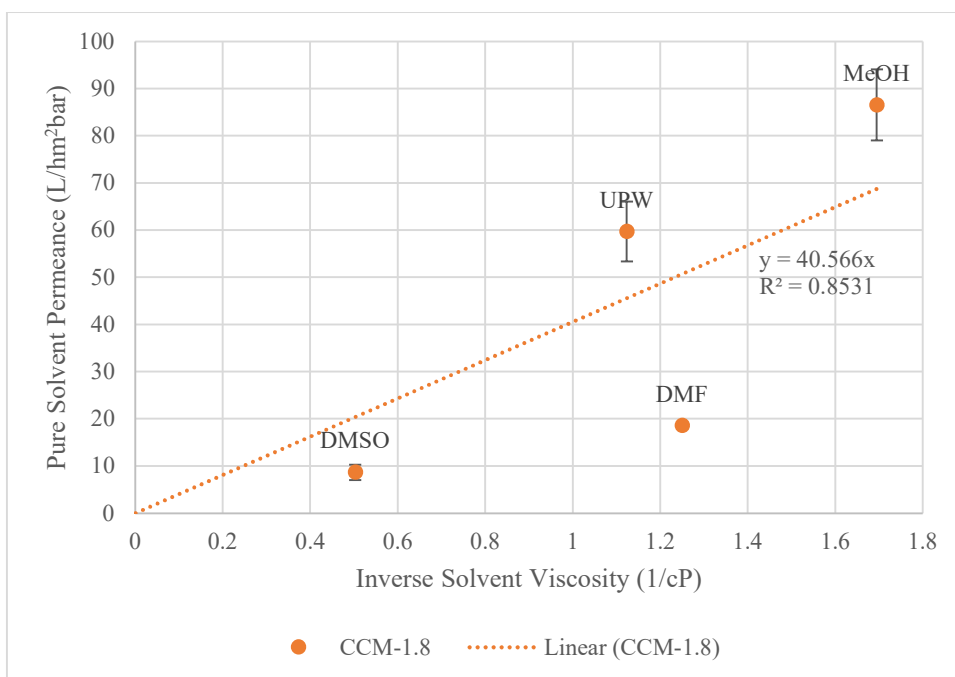
Figure 3.21 Pure Solvent Permeances of CCM-1.8
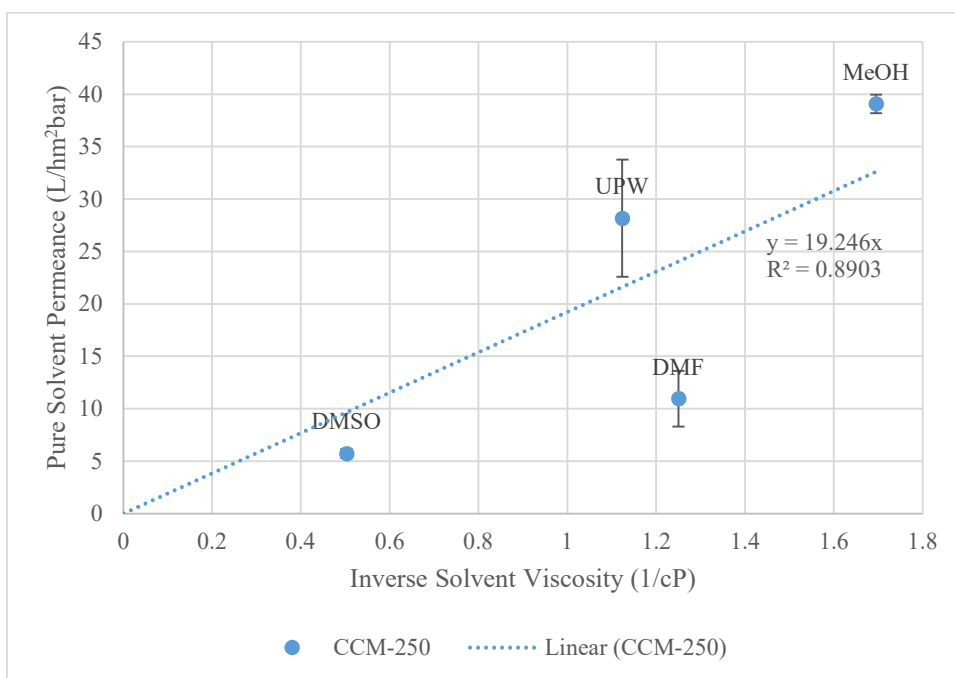
Figure 3.22 Pure Solvent Permeances of CCM-250

The data points in Figure 3.21 and Figure 3.22 represent the mean of all PSP values measured in the experiments and the error bars represent the standard deviation.

The roughly linear relation between PSP values and inverse solvent viscosity indicates that the membranes obey Darcy's Law of fluid flow through porous media. Hence, the membranes operate in the pore-flow filtration regime.

3.3.2.4   Pore Sizes of the Membranes PRCA-15, CCM-1.8, CCM-250

PEG probes of 2kDa, 6kDa, 10kDa, and 20kDa MW were dissolved in the solvents UPW, MeOH, DMSO and DMF at 0.1g/L concentration. Each sample was measured four times. The hydrodynamic diameter data is available in Table 3.15.

Table 3.15 Hydrodynamic Diameters of PEG Probes in Different Solvents

PEG MW (kDa)	Size in UPW	Size in MeOH	Size in DMF	Size in DMSO
2	2.7 ± 0.2 nm	3.0 ± 0.9 nm	2.7 ± 0.8 nm	Refractive
6	4.7 ± 0.4 nm	5.9 ± 1.4 nm	4.6 ± 1.0 nm	Indices too
10	6.1 ± 0.3 nm	8.9 ± 1.2 nm	9.6 ± 2.2 nm	Close
20	10.3 ± 0.6 nm	12.7 ± 1.4 nm	13.8 ± 2.8 nm	14.4 ± 4.5 nm

PEG probe molecules were found to be of roughly the same size in different solvents.

The diameters of lighter PEG probes could not be discerned in DMSO as the refractive indices of the probe molecules was very close to that of the solvent.

Average pore sizes were estimated using the Ferry – Renkin equation. The pore sizes are available in Figure 3.23.

Figure 3.23 Pore Sizes of the Membranes
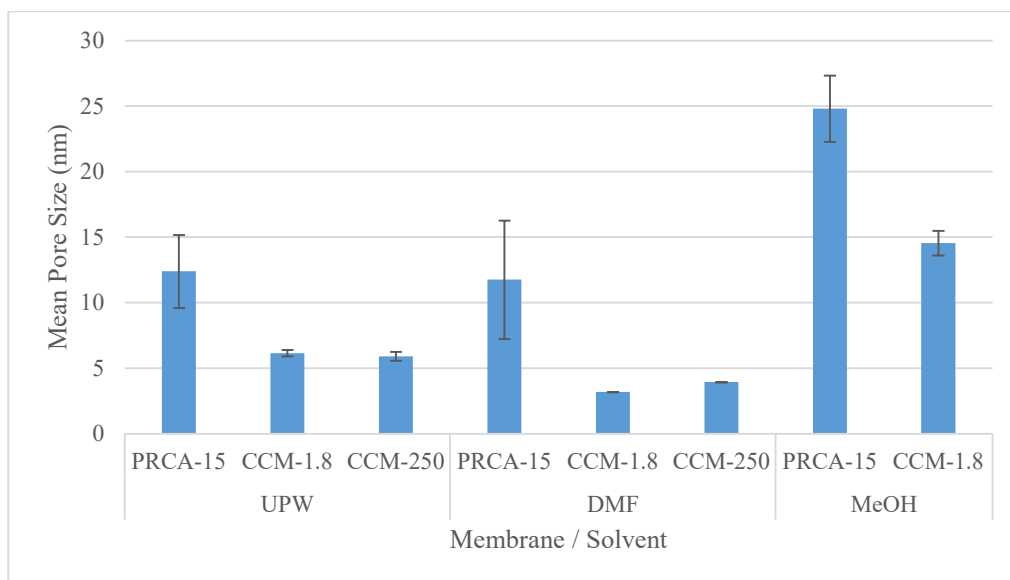
When the pore sizes are compared, it can be inferred that the coating reduces the mean pore size by a factor about two in UPW and DMSO. The pore size is reduced by a factor about three in the solvent DMF. When considered together with relatively low pure solvent permeances in DMF, this suggests that the coatings act as dense and stable selective layers in a DMF environment.

3.3.2.5 Dye Rejections of CCM-1.8, CCM-250, CPM-1.8 and CPM-250

CNC+ / PAA coated membranes with PRCA-15 or PES-15 supports were subjected to dye filtration tests. The dyes used were RB (-2 or -1 charge) and CV (+1 charge) in either aqueous solution or dissolved in MeOH. A TMP of 0.2 bar was applied and the cells were stirred at 600rpm. Besides membranes with 4 bilayers, 4.5 bilayer membranes with CNC+ as the topmost layer were also prepared to investigate the effect of outmost layer on the dye rejections.

The steady-state rejections of the dyes RB and CV in UPW and MeOH are available in Figure 3.24 and Figure 3.25. In these figures, the sign reported after the membrane indicates the charge of the terminating layer.
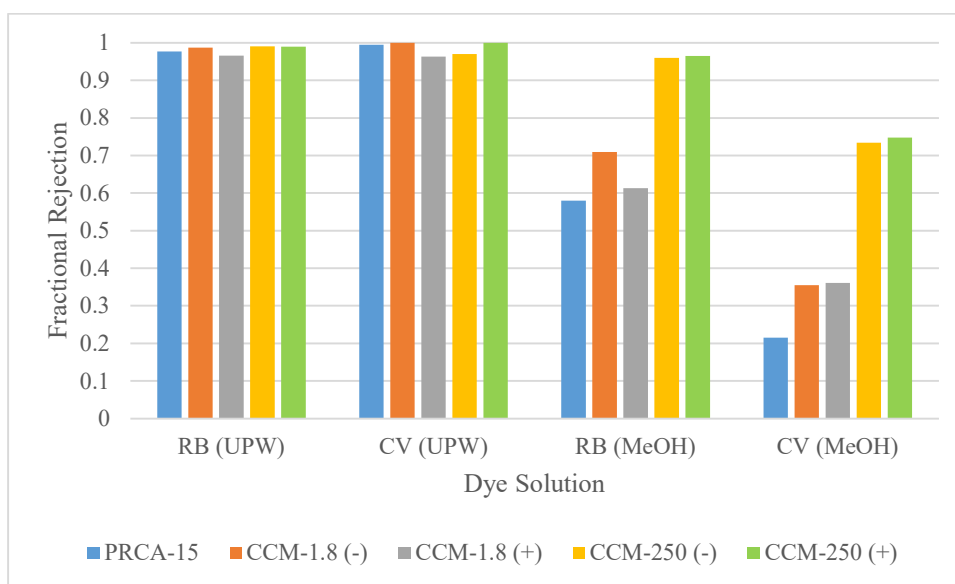
Figure 3.24 Dye Rejections of PRCA-15, CCM-1.8 and CCM-250 Membranes
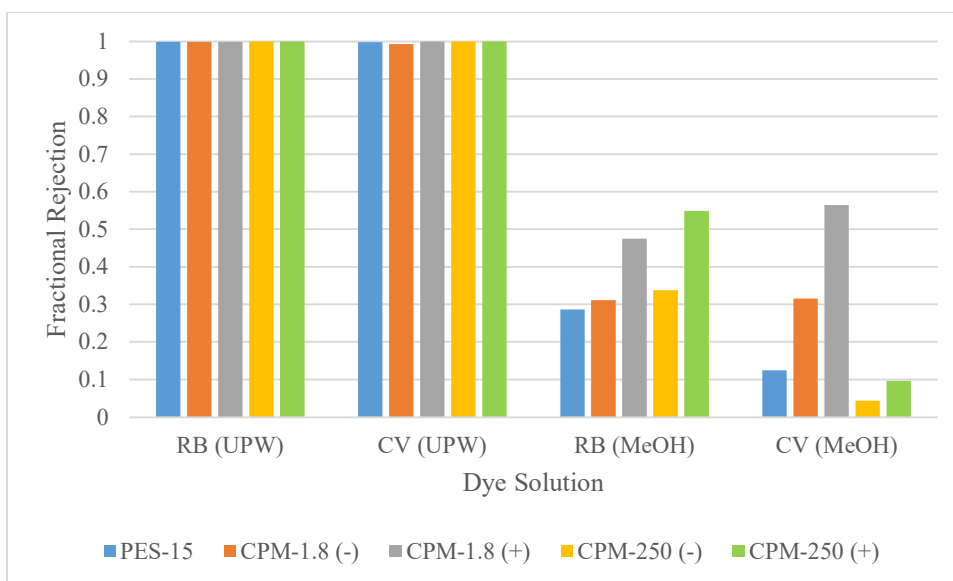
Figure 3.25 Dye Rejections of PES-15, CPM-1.8 and CPM-250 Membranes

Using material balances, crystal violet was found to sorb to all membranes in aqueous solution. This explains the almost complete rejections calculated, which are due to sorption by the membrane and not rejection by membrane pores. The amounts sorbed are indicated in Table 3.16.

Table 3.16 Amounts of CV Sorbed from Aqueous Feed Solution

Membrane	Terminated With	Moles Dye Sorbed	% Feed Dye Sorbed
CCM-1.8	PAA (-)	0.196 μmol	64%
CCM-1.8	CNC+ (+)	0.191 μmol	62%
CCM-250	PAA (-)	0.286 μmol	93%
CCM-250	CNC+ (+)	0.257 μmol	84%
PRCA-15	N/A	0.176 μmol	57%
CPM-1.8	PAA (-)	0.256 μmol	42%
CPM-1.8	CNC+ (+)	0.193 μmol	32%
CPM-250	PAA (-)	0.374 μmol	61%
CPM-250	CNC+ (+)	0.377 μmol	62%
PES-15	N/A	0.271 μmol	44%

CV sorption from feed solutions prepared using MeOH as the solvent was found to be milder. This is possibly due to the more favorable solute-solvent interactions with the less polar methanol compared to water, as crystal violet has a positive logarithmic octanol-water partition coefficient of 0.51. The amounts of CV sorbed are indicated in Table 3.17.

Table 3.17 Amounts of CV Sorbed from Feed Solution in MeOH

Membrane	Terminated With	Moles Dye Sorbed	% Feed Dye Sorbed
CCM-1.8	PAA (-)	0.009 μmol	3%
CCM-1.8	CNC+ (+)	0.006 μmol	2%
CCM-250	PAA (-)	0.022 μmol	7%
CCM-250	CNC+ (+)	0.016 μmol	5%
PRCA-15	N/A	0.008 μmol	3%
CPM-1.8	PAA (-)	0.000 μmol	0%
CPM-1.8	CNC+ (+)	0.000 μmol	0%
CPM-250	PAA (-)	0.014 μmol	2%
CPM-250	CNC+ (+)	0.015 μmol	2%
PES-15	N/A	0.015 μmol	2%

As CV sorption effects were significantly milder when MeOH was used as the solvent, a sorption and breakthrough phenomenon was not observed as in aqueous environment.

The negatively charged dye, RB, showed negligible sorption in both MeOH and UPW solvents.

The dye RB was totally rejected in aqueous solution. Separation of this dye via size sieving is not plausible as RB has a MW much lower than the MWCO of the support membranes. Therefore, this rejection is inferred to be due to charge interactions with the support membranes.

RB rejections in MeOH indicate that the charge interactions are weakened in the solvent MeOH compared to water. This leads to lower rejections by the support membranes (98% vs. 58% for PRCA-15, 100% vs. 27% for PES-15) as seen in Figure 3.24 and Figure 3.25. Coated membranes were found to have higher RB rejections (up to 96% for CCM-250) compared to their support membranes when MeOH was used as the solvent. PAA MW was the determining factor in RB rejections for PRCA-15 based membranes, possibly due to the presence of separate negatively charged PAA layers present in CCM-250 as illustrated in Figure 3.25Figure 3.26. The topmost layer was an important parameter in CPM membranes. A possible reason for this is that PES-15 is significantly less negatively charged compared to PRCA-15, and the positive layer might have better screened the support charge.
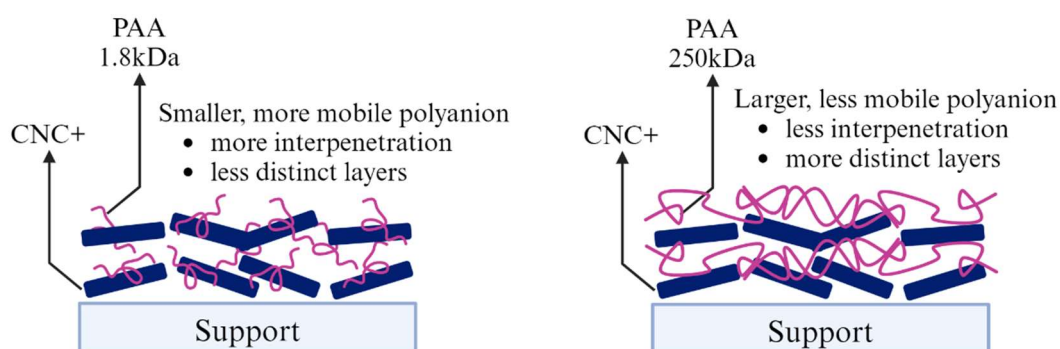
Figure 3.26 Schematic Representation of Plausible Layer Structures in CNC+ / PAA LbL Assembled Coatings

Due to the significant sorption of the positively charged dye CV, the membranes act as sorbents in the filtrations in water. The high apparent rejection caused by dye uptake by the membranes is transient and no significant rejection is observed when the feed solution is equilibrated with the membrane. Therefore, crystal violet separations in water are not to be taken as rejections, but rather as removal by sorption.

CV rejections of the support membranes were low in MeOH solvent. Coatings on PRCA-15 support gave higher rejection values compared to the support itself. The best performance was displayed by the membrane CCM-250, and the topmost layer did not influence the rejection significantly.

In essence, the support membranes and the coated membranes were able to reject negatively charged solutes with molecular weights significantly smaller than their MWCO in aqueous environment. The charge interaction is weakened in MeOH, yet negatively charged substances are still rejected to a significant extent by CCM-250. The membranes show low rejection of positively charged small molecules. All membranes sorb positively charged small molecules in aqueous environment. Therefore, these membranes could be used to separate small, negatively charged molecules from aqueous solutions.

3.3.2.6   Transient Dye Sorption Experiments

Transient dye sorption experiments were performed to observe the time-dependent sorption of oppositely charged dye to the membranes, in order to estimate the charge of the support and coated membranes. CCM-1.8 membranes prepared with a negatively charged PAA terminating layer (denoted as CCM-1.8 (-)), a positively charged CNC+ terminating layer (denoted as CCM-1.8 (+)), as well as the support membranes PRCA-15 and RCA-15 were subjected to transient CV sorption test. The calculated rates of dye sorption are available in Figure 3.27.
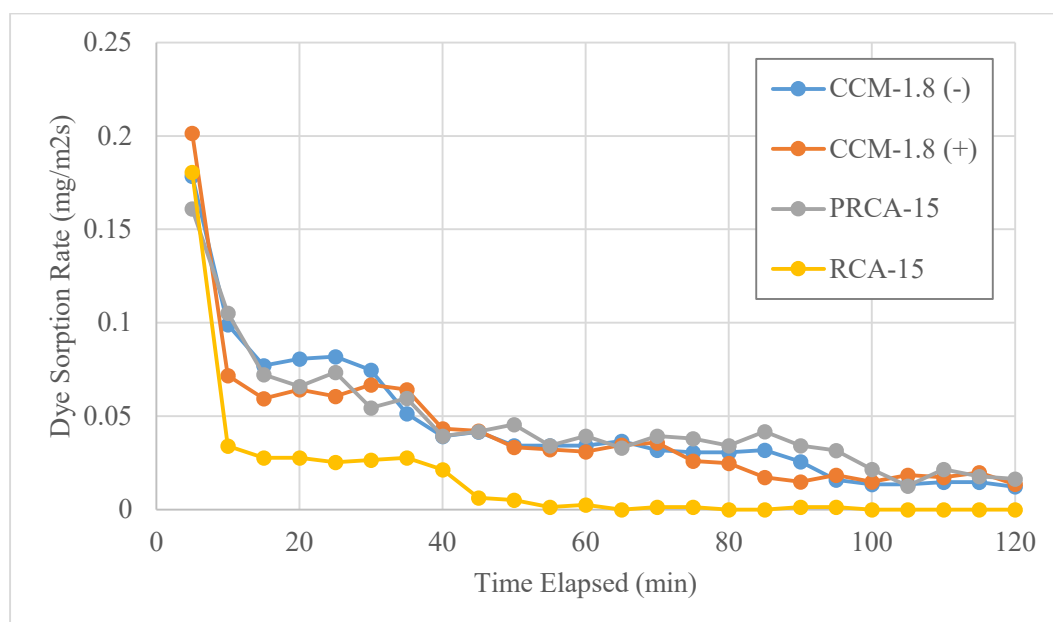
Figure 3.27 CV Sorption Rates

The dye sorption rates observed for the CCM-1.8 membranes indicate that the terminating layer has little effect on the dye sorption behavior of the membrane. Moreover, the sorption rates for CCM-1.8 membranes are very similar to that of the support membrane used in their preparation, PRCA-15. These results indicate that the support membrane is responsible for most of the dye uptake. The support membrane also appears to be responsible for the charge of coated membranes.

RCA-15 membrane was shown to be saturated with the dye after 50 minutes, which can be inferred from the sorption rate dropping to zero. The surface concentration of sorbed dye, available in Figure 3.28, also levels off at this time.
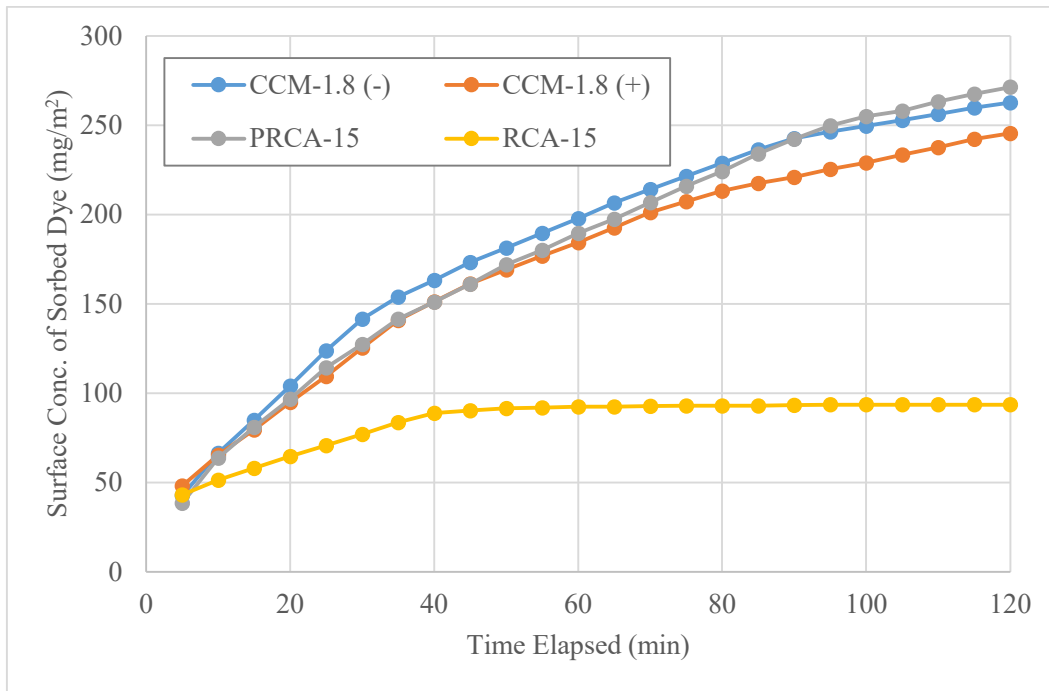
Figure 3.28 Surface Concentrations of CV

The high sorption rates and higher sorption capacity displayed by the membrane PRCA-15 and coated membranes prepared from it indicates that these membranes are more negatively charged compared to RCA-15. Given RCA-15 saturates at 94 mg / m^2 CV, and PRCA-15 and membranes prepared from it appear to be unsaturated at 250 mg / m^2 CV, membrane surface charges may be roughly estimated as:

$$\sigma_{RCA-1} = F * \Gamma = -96.5 \frac{C}{mmol} * 94 \frac{mg}{m^2} * 408^{-1} \frac{mmol}{mg} \approx -22 \frac{C}{m^2}$$

$$\sigma_{PRCA-15} \leq F * \Gamma = -96.5 \frac{C}{mmol} * 250 \frac{mg}{m^2} * 408^{-1} \frac{mmol}{mg} \approx -59 \frac{C}{m^2}$$

3.3.2.7   MWCO Values of CCM-1.8 and CCM-250

The rejection results for PEG filtrations in aqueous solution are available in Figure 3.29. The data points represent the mean of all experiments done, and the error bars represent the standard deviation.
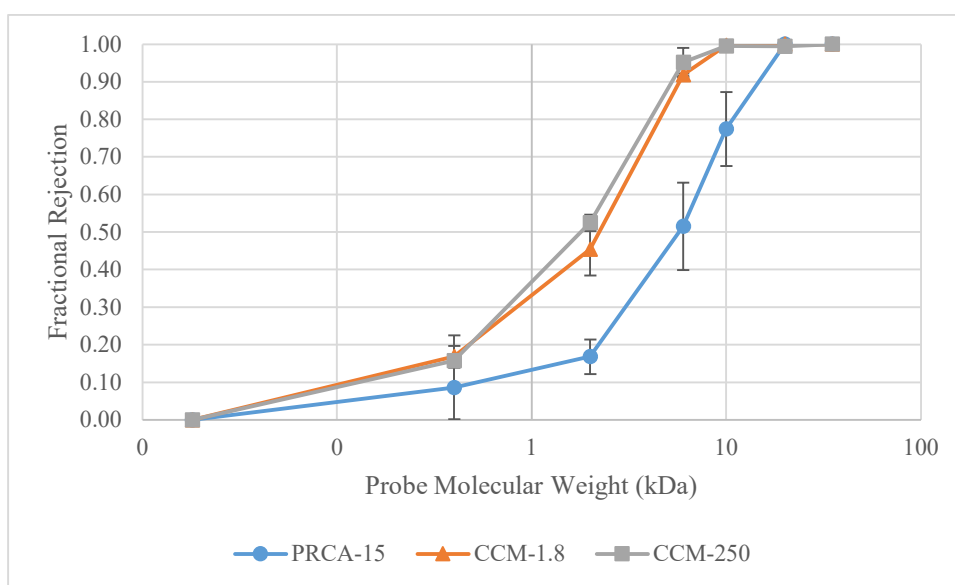
Figure 3.29 MWCO Curves in Water

The MWCO ranges obtained and the PWP values of the membranes are indicated in Table 3.18.

Table 3.18 PWP and MWCO Results in Water

Membrane	PWP (L/hm^{2}bar)	MWCO (kDa)
PRCA-15	69	15.5
CCM-1.8	60	5.7 – 5.9
CCM-250	28	5.5 – 6.5

According to the results in Table 3.18, both coatings significantly improve the separation performance of the membrane. CCM-1.8 can be said to be superior in aqueous environment as it offers the same separation performance at a higher permeance.

The rejection results for PEG filtrations in MeOH solution are available in Figure 3.30. The membrane was left submerged in the solvent for one week, and the repeated experiment is indicated.
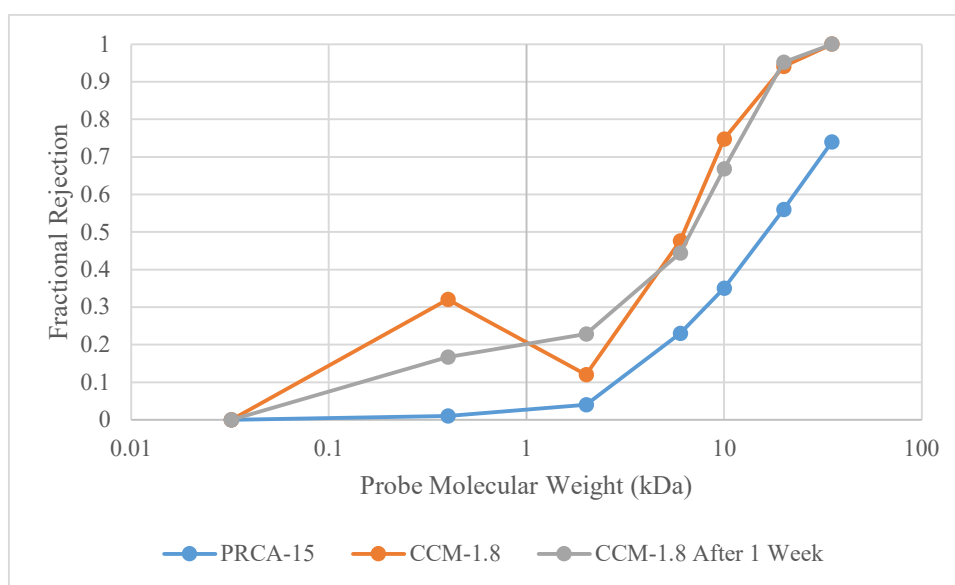
Figure 3.30 MWCO Curves in MeOH

The MWCO values obtained and the PSP values of the membranes are indicated in Table 3.19.

Table 3.19 PSP and MWCO Results in MeOH

Membrane	PSP (L/hm^{2}bar)	MWCO (kDa)
PRCA-15	97	>35
CCM-1.8 (Fresh)	84	17.7
CCM-1.8 (After One Week)	79	18.1

According to the results in Table 3.19, CNC+ / PAA 1.8kDa coating significantly improves the separation performance of the membrane. CCM-250 membranes displayed lower performance with respect to rejections compared to the support. This might be due to probe – polyelectrolyte specific interactions leading to a higher feed side PEG concentration, as concentration polarization was ruled out by permeance measurements.

The rejection results for PEG filtrations in DMSO solution are available in Figure 3.31. To test the stability of the membranes in the solvent, filtrations were repeated for a duration of one week.
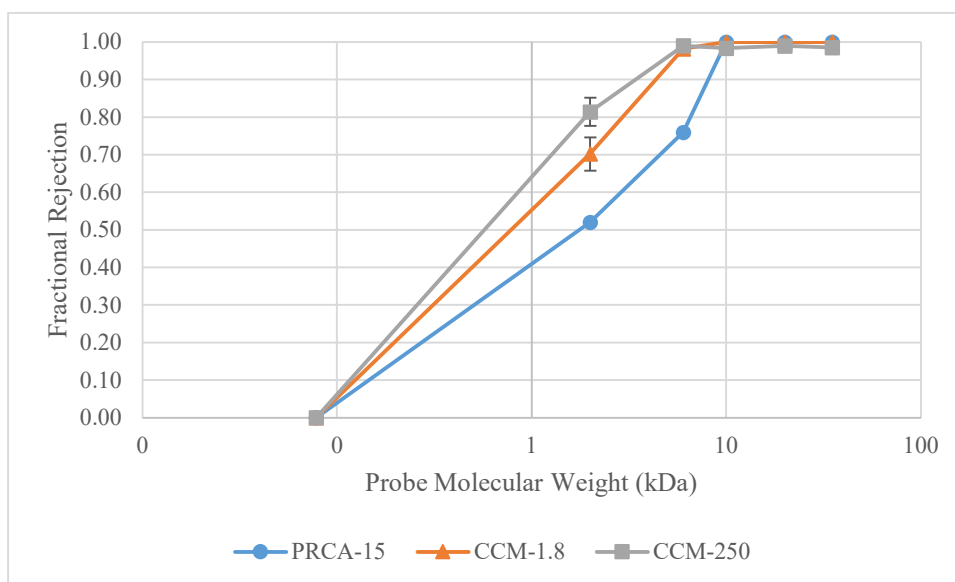
Figure 3.31 MWCO Curves in DMSO

The MWCO ranges obtained and the PSP values of the membranes are indicated in Table 3.20.

Table 3.20 PSP and MWCO Results in DMSO

Membrane	PSP (L/hm^{2}bar)	MWCO (kDa)
PRCA-15	26	8.4
CCM-1.8	9	4.6 – 5.1
CCM-250	6	2.7 – 4.6

According to the results in Table 3.20, both coatings significantly improved the separation performance of the membrane. CCM-250 offers better separation performance compared to CCM-1.8, at the expense of a lower permeance.

The rejection results for PEG filtrations in DMF solution are available in Figure 3.32. To test the stability of the membranes in the solvent, filtrations were repeated for a duration of one week.
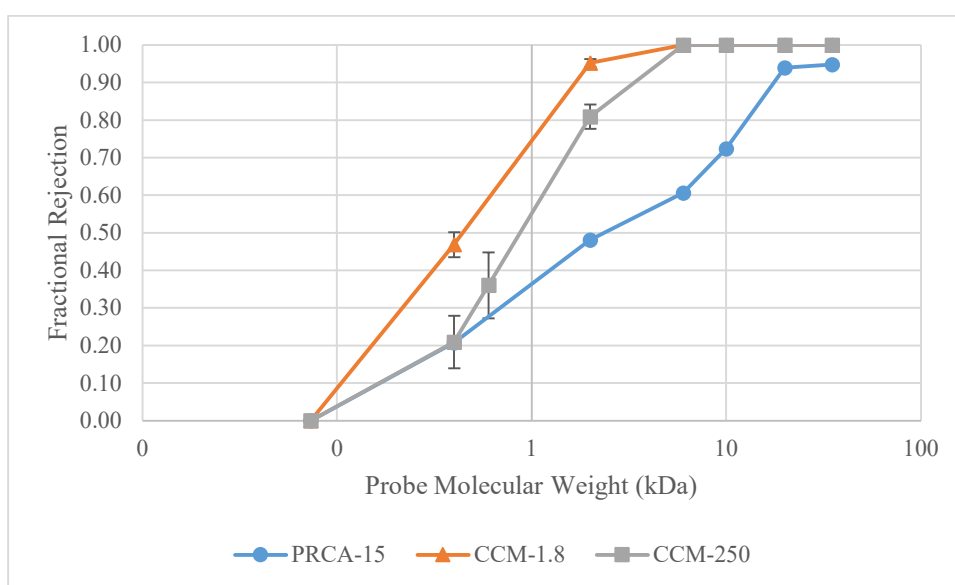
Figure 3.32 MWCO Curves in DMF

The MWCO ranges obtained and the PSP values of the membranes are indicated in Table 3.21.

Table 3.21 PSP and MWCO Results in DMF

Membrane	PSP (L/hm^{2}bar)	MWCO (kDa)
PRCA-15	37	18.2
CCM-1.8	19	1.8 – 1.9
CCM-250	11	2.8 – 4.4

According to the results in Table 3.21, both coatings significantly improve the separation performance of the membrane without a drastic reduction in permeance. The MWCO results indicate that the membrane CCM-1.8 is superior to the support in terms of separation performance in all solvents tested. The coated membrane

CCM-250 is superior to the support in terms of separation performance in the solvents water, DMSO, and DMF.

Both coated membranes were found to be stable for a week without MWCO deviation in the polar aprotic solvents used. The results of these repeated tests are available in Figure 3.33 and Figure 3.34.
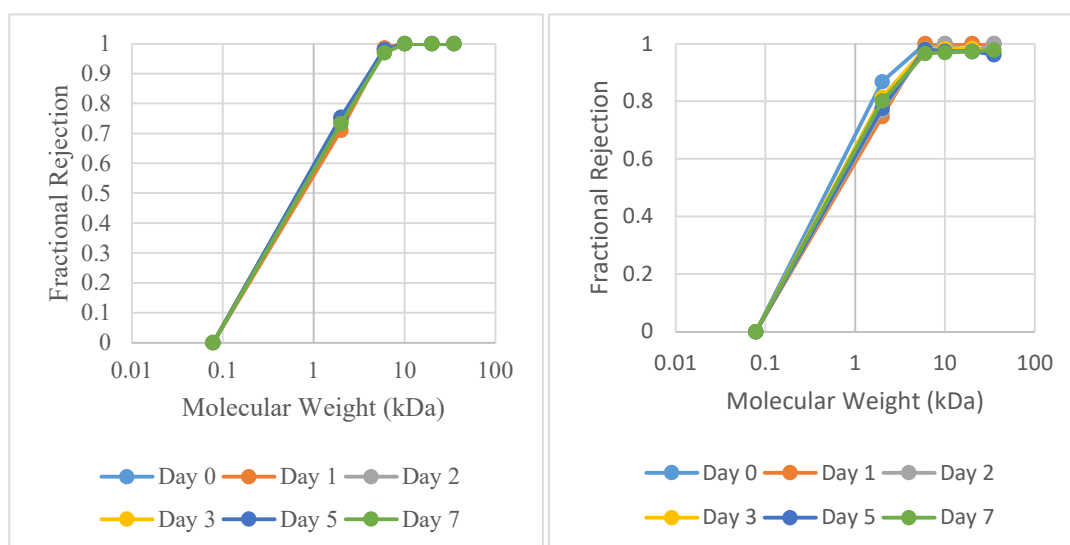
Figure 3.33 Repeated MWCO Test Results for CCM-1.8 (left) and CCM-250 (right) in DMSO
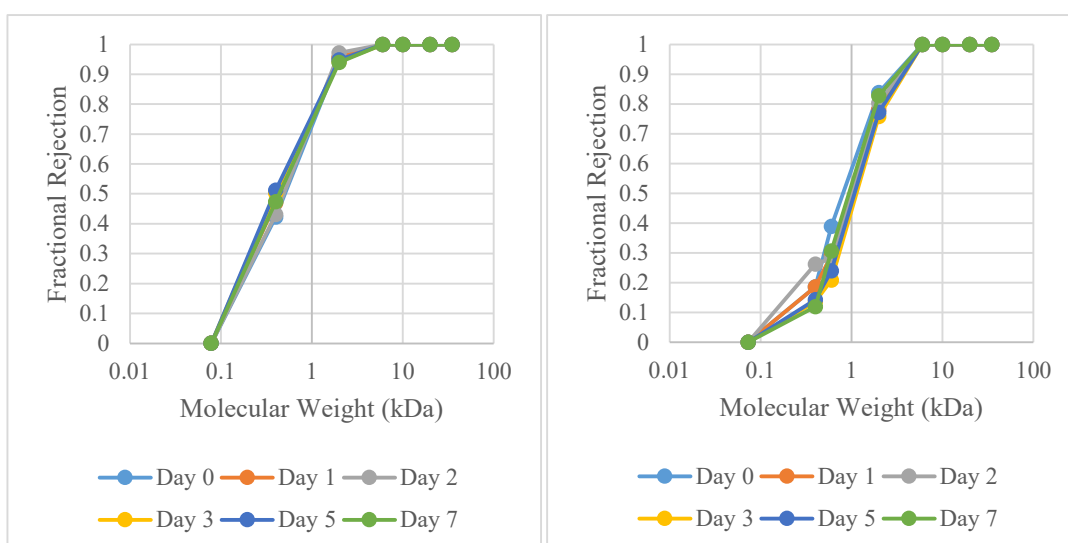
Figure 3.34 Repeated MWCO Test Results for CCM-1.8 (left) and CCM-250 (right) in DMF

The MWCO order decreases in the order MeOH > DMSO ≈ UPW > DMF. Therefore, the trend is the same as the support membrane except for the solvent DMF. It is proposed that the polyelectrolyte / CNC+ selective layer interacts with DMF in a markedly different way compared to the interaction of cellulose and DMF, and that the specific interactions between the solvent and the selective layer become important. However, as the selective layer is extremely thin, experiments on the selective layer alone to determine its properties cannot be practiced. Moreover, experiments on the whole membrane are unlikely to yield trustworthy results about the selective layer since the bulk of the membrane is composed of the support layer. For these reasons, the investigation of selective layer – solvent interactions was not pursued.

CHAPTER 4

CONCLUSION

LbL coating methodology can be applied to improve separation performance of membranes. Studies in this field have generally focused on the application of polyelectrolyte coatings. While the application of polyelectrolyte multilayers offers satisfactory separation performance, the accompanying loss in permeance can be significant in some cases. Furthermore, some studies in polyelectrolyte multilayer membranes for application in organic solvents require the deposition of a very large number of bilayers.

In this study, the aim was to explore LbL coating applications utilizing nanocellulose materials for membrane preparation and separation of organic and aqueous solutions. For this purpose, polyelectrolyte / nanocellulose multilayer coated cellulose ultrafiltration membranes were made for aqueous as well as organic solvent filtration. Support membranes were prepared by casting organic solutions of cellulose acetate and carrying out nonsolvent induced phase separation. The cellulose acetate support membranes were turned into cellulose membranes by alkaline hydrolysis in 0.05M NaOH. Cellulose membranes were chemically derivatized to render them suitable for coating.

Cellulose nanocrystals were prepared from cotton linter cellulose via sulfuric acid hydrolysis. Cationic cellulose nanocrystals were then obtained by a chemical reaction with glycidyltrimethylammonium chloride. TEMPO-oxidized cellulose nanocrystals were also produced. All nanocrystal suspensions were characterized and found to be similar to the substances reported in the literature.

Layer-by-layer self-assembly technique was used to modify the membrane surfaces with either oppositely charged nanocellulose particles or nanocellulose particles and polyelectrolytes. Multilayer deposition was followed using ellipsometry together with the changes in permeance and resistance to track the deposition of layers and to observe the growth behavior of the selective layer.

The coated membranes were tested in water, methanol, DMSO and DMF and were shown to be stable in all three organic solvents. SEM imaging has revealed complete surface coverage with a dried coating thickness of 0.5-0.6 microns. MWCO results and pore size calculations have shown that the coatings act as selective layers. The coated membranes displayed superior separation performance to the support without a drastic loss in permeance (5-6kDa vs. 15kDa in water, 17-18kDa vs. >35kDa in MeOH, 3-5kDa vs. 8kDa in DMSO, 2-4kDa vs. 18kDa in DMF). The membranes were found to be significantly negatively charged and displayed retention of small negatively charged solutes based on their charge (complete rejection of Rose Bengal (RB) in water, up to 95% RB rejection in MeOH).

REFERENCES

1. Coker AK, Coker AK. Chapter 10 – Distillation: Part 1: Distillation Process Performance. In: Ludwig's Applied Process Design for Chemical and Petrochemical Plants. 2010.

2. Baker RW. Membrane Technology and Applications. Membrane Technology and Applications. 2012.

3. Marchetti P, Jimenez Solomon MF, Szekely G, Livingston AG. Molecular Separation with Organic Solvent Nanofiltration: A Critical Review. Chem Rev [Internet]. 2014 Nov 12;114(21):10735–806. Available from: https://pubs.acs.org/doi/10.1021/cr500006j

4. Ezugbe EO, Rathilal S. Membrane technologies in wastewater treatment: A review. Vol. 10, Membranes. 2020.

5. Qasim M, Badrelzaman M, Darwish NN, Darwish NA, Hilal N. Reverse osmosis desalination: A state-of-the-art review. Vol. 459, Desalination. 2019.

6. Sánchez-Arévalo CM, Vincent-Vela MC, Luján-Facundo MJ, Álvarez-Blanco S. Ultrafiltration with organic solvents: A review on achieved results, membrane materials and challenges to face. Vol. 177, Process Safety and Environmental Protection. 2023.

7. Vandezande P, Gevers LEM, Vankelecom IFJ. Solvent resistant nanofiltration: separating on a molecular level. Chem Soc Rev [Internet]. 2008;37(2):365–405. Available from: http://xlink.rsc.org/?DOI=B610848M

8. Liu C, Dong G, Tsuru T, Matsuyama H. Organic solvent reverse osmosis membranes for organic liquid mixture separation: A review. Vol. 620, Journal of Membrane Science. 2021.

9. Yang Q, Sheng M, Li X, Tucker C, Vásquez Céspedes S, Webb NJ, et al. Potential Explosion Hazards Associated with the Autocatalytic Thermal Decomposition of Dimethyl Sulfoxide and Its Mixtures. Vol. 24, Organic Process Research and Development. 2020.

10. Klemm D, Heublein B, Fink HP, Bohn A. Cellulose: Fascinating biopolymer and sustainable raw material. Vol. 44, Angewandte Chemie - International Edition. 2005.

11. Hermanutz F, Vocht MP, Panzier N, Buchmeiser MR. Processing of Cellulose Using Ionic Liquids. Vol. 304, Macromolecular Materials and Engineering. 2019.

12. Sayyed AJ, Deshmukh NA, Pinjari D V. A critical review of manufacturing processes used in regenerated cellulosic fibres: viscose, cellulose acetate, cuprammonium, LiCl/DMAc, ionic liquids, and NMMO based lyocell. Vol. 26, Cellulose. 2019.

13. Malaisamy R, Bruening ML. High-flux nanofiltration membranes prepared by adsorption of multilayer polyelectrolyte membranes on polymeric supports. Langmuir. 2005;21(23).

14. Emonds S, Kamp J, Viermann R, Kalde A, Roth H, Wessling M. Open and dense hollow fiber nanofiltration membranes through a streamlined polyelectrolyte-based spinning process. J Memb Sci. 2022;644.

15. Kamp J, Emonds S, Seidenfaden M, Papenheim P, Kryschewski M, Rubner J, et al. Tuning the excess charge and inverting the salt rejection hierarchy of polyelectrolyte multilayer membranes. J Memb Sci. 2021;639.

16. Saleh TA, Gupta VK. Membrane Classification and Membrane Operations. In: Nanomaterial and Polymer Membranes. 2016.

17. Abd El-Ghaffar MA, Tieama HA. A Review of Membranes Classifications, Configurations, Surface Modifications, Characteristics and Its Applications in Water Purification. Chemical and Biomolecular Engineering. 2017;2(2).

18. Loeb S, Souriranjan S. Sea Water Demineralization by means of semipermeable membrane. UCLA report. 1960;60(60).

19. Strathmann H, Kock K, Amar P, Baker RW. The formation mechanism of asymmetric membranes. Desalination. 1975;16(2).

20. So MT, Eirich FR, Strathmann H, Baker RW. Preparation of asymmetric loeb-sourirajan membranes. Journal of Polymer Science: Polymer Letters Edition. 1973;11(3).

21. Lau WJ, Feng X. 60 years of the Loeb-Sourirajan membrane: From fundamental research to industrial application. Vol. 168, Chemical Engineering Research and Design. 2021.

22. Li X, Wang Z, Han X, Liu Y, Wang C, Yan F, et al. Regulating the interfacial polymerization process toward high-performance polyamide thin-film composite reverse osmosis and nanofiltration membranes: A review. Vol. 640, Journal of Membrane Science. 2021.

23. Baker RW. Membrane Transport Theory. In: Membrane Technology and Applications. 2012.

24. Phillip WA, Rzayev J, Hillmyer MA, Cussler EL. Gas and water liquid transport through nanoporous block copolymer membranes. J Memb Sci. 2006;286(1–2).

25. Yang DC, Castellano RJ, Silvy RP, Lageshetty SK, Praino RF, Fornasiero F, et al. Fast Water Transport through Subnanometer Diameter Vertically Aligned Carbon Nanotube Membranes. Nano Lett. 2023;23(11).

26. Fu J, Thomas HR, Li C. Tortuosity of porous media: Image analysis and physical simulation. Vol. 212, Earth-Science Reviews. 2021.

27.   RENKIN EM. Filtration, diffusion, and molecular sieving through porous cellulose membranes. J Gen Physiol. 1954;38(2).

28.   Wijmans JG, Baker RW. The solution-diffusion model: a review. Vol. 107, Journal of Membrane Science. 1995.

29.   Pulido BA, Waldron C, Zolotukhin MG, Nunes SP. Porous polymeric membranes with thermal and solvent resistance. J Memb Sci. 2017;539.

30.   Isik M, Sardon H, Mecerreyes D. Ionic liquids and cellulose: Dissolution, chemical modification and preparation of new cellulosic materials. Vol. 15, International Journal of Molecular Sciences. 2014.

31.   Cheng C, Xu Z, Zhang D, Xv J, Liu P. The effect of dissolution temperature and NMMO concentration on cellulose dissolution. Fangzhi Gaoxiao Jichukexue Xuebao. 2021;34(2).

32.   Dogan H, Hilmioglu ND. Dissolution of cellulose with NMMO by microwave heating. Carbohydr Polym. 2009;75(1).

33.   Wang W, Li Y, Li W, Zhang B, Liu Y. Effect of solvent pre-treatment on the structures and dissolution of microcrystalline cellulose in lithium chloride/dimethylacetamide. Cellulose. 2019;26(5).

34.   Zhang C, Liu R, Xiang J, Kang H, Liu Z, Huang Y. Dissolution mechanism of cellulose in N,N-dimethylacetamide/lithium chloride: Revisiting through molecular interactions. Journal of Physical Chemistry B. 2014;118(31).

35.   Zaccaron S, Henniges U, Potthast A, Rosenau T. How alkaline solvents in viscosity measurements affect data for oxidatively damaged celluloses. Cuoxam and Cadoxen. Carbohydr Polym. 2020;240.

36.   Bourassi L, Challioui A, Merzouki M, Abidi R, Bouammali B, Elfarh L, et al. A molecular dynamics (MD) simulation of the solubility behaviours of cellulose in aqueous cuprammonium hydroxide solution. Mater Today Proc. 2023;72.

37. WISEMAN LA. History of Viscose Rayon. Nature. 1963;197(4867).

38. Gondhalekar SC, Pawar PJ, Dhumal SS, Thakre S. Fate of CS2 in viscose process: a chemistry perspective. Cellulose. 2022;29(3).

39. Iovleva MM, Smirnova VN, Budnitskii GA. The solubility of polyacrylonitrile. Fibre Chemistry. 2001;33(4).

40. Sridhar S, Smitha B, Mayor S, Prathab B, Aminabhavi TM. Gas permeation properties of polyamide membrane prepared by interfacial polymerization. J Mater Sci. 2007;42(22).

41. Khaparde D. Preparation and prediction of physical properties of cellulose acetate and polyamide polymer blend. Carbohydr Polym. 2017;173.

42. Tao M mi, Liu F, Ma B rong, Xue L xin. Effect of solvent power on PVDF membrane polymorphism during phase inversion. Desalination. 2013;316.

43. Xu A, Cao L, Wang B. Facile cellulose dissolution without heating in [C4mim][CH3COO]/DMF solvent. Carbohydr Polym. 2015;125.

44. Tekin FS, Çulfaz-Emecen PZ. Controlling Cellulose Membrane Performance via Solvent Choice during Precursor Membrane Formation. ACS Appl Polym Mater. 2023;5(3).

45. Savaş-Alkan A, Çulfaz-Emecen PZ. Solvent recovery from photolithography wastes using cellulose ultrafiltration membranes. J Memb Sci. 2022;647.

46. Nguyen Thi HY, Kim S, Duy Nguyen BT, Lim D, Kumar S, Lee H, et al. Closing the Sustainable Life Cycle Loop of Membrane Technology via a Cellulose Biomass Platform. ACS Sustain Chem Eng. 2022;10(7).

47. Falca G, Musteata VE, Behzad AR, Chisca S, Nunes SP. Cellulose hollow fibers for organic resistant nanofiltration. J Memb Sci. 2019;586.

48. Kim D, Livazovic S, Falca G, Nunes SP. Oil-Water Separation using Membranes Manufactured from Cellulose/Ionic Liquid Solutions. ACS Sustain Chem Eng. 2019;7(6).

49. Cifuentes-Cabezas M, Carbonell-Alcaina C, Vincent-Vela MC, Mendoza-Roca JA, Álvarez-Blanco S. Comparison of different ultrafiltration membranes as first step for the recovery of phenolic compounds from olive-oil washing wastewater. Process Safety and Environmental Protection. 2021;149.

50. Abd-Razak NH, Zairossani MN, Chew YMJ, Bird MR. Fouling Analysis and the Recovery of Phytosterols from Orange Juice Using Regenerated Cellulose Ultrafiltration Membranes. Food Bioproc Tech. 2020;13(11).

51. Moreno-Vilet L, Moscosa-Santillán M, Grajales-Lagunes A, González-Chávez M, Bonnin-Paris J, Bostyn S, et al. Sugars and Fructans Separation by Nanofiltration from Model Sugar Solution and Comparative Study with Natural Agave Juice. Separation Science and Technology (Philadelphia). 2013;48(12).

52. Schmidt JM, Greve-Poulsen M, Damgaard H, Hammershøj M, Larsen LB. Effect of Membrane Material on the Separation of Proteins and Polyphenol Oxidase in Ultrafiltration of Potato Fruit Juice. Food Bioproc Tech. 2016;9(5).

53. González-Muñoz MJ, Santos V, Parajó JC. Purification of oligosaccharides obtained from Pinus pinaster hemicelluloses by diafiltration. Desalination Water Treat. 2011;27(1–3).

54. Batrinescu G, Scutariu RE, Nechifor G, Ionescu IA, Iancu VI. Comparative analysis of the processes of collagen concentration by ultrafiltration using different types of membranes. J Appl Polym Sci. 2021;138(12).

55. Tulos N, Harbottle D, Hebden A, Goswami P, Blackburn RS. Kinetic Analysis of Cellulose Acetate/Cellulose II Hybrid Fiber Formation by Alkaline Hydrolysis. ACS Omega. 2019;4(3).

56. Strathmann H, Scheible P, Baker RW. A rationale for the preparation of Loeb-Sourirajan-type cellulose acetate membranes. J Appl Polym Sci. 1971;15(4).

57. Abdellah MH, Oviedo C, Szekely G. Controlling the degree of acetylation in cellulose-based nanofiltration membranes for enhanced solvent resistance. J Memb Sci. 2023;687.

58. Zhou YJ, Luner P, Caluwe P. Mechanism of crosslinking of papers with polyfunctional carboxylic acids. J Appl Polym Sci. 1995;58(9).

59. Malm CJ, Mench JW, Fulkerson B, Hiatt GD. Preparation of Phthalic Acid Esters of Cellulose. Ind Eng Chem. 1957;49(1).

60. Sawatari C, Yagi T. Introduction of amino groups into cellulose via (2, 3-dibromopropyl)cellulose under mild conditions. Sen'i Gakkaishi. 1991;47(9).

61. Bhushan S, Etzel MR. Charged ultrafiltration membranes for protein separation. In: 2007 ASABE Annual International Meeting, Technical Papers. 2007.

62. Shui T, Feng S, Chen G, Li A, Yuan Z, Shui H, et al. Synthesis of sodium carboxymethyl cellulose using bleached crude cellulose fractionated from cornstalk. Biomass Bioenergy. 2017;105.

63. Wang A, Yuan Z, Wang C, Luo L, Zhang W, Geng S, et al. Zwitterionic Cellulose Nanofibrils with High Salt Sensitivity and Tolerance. Biomacromolecules. 2020;21(4).

64. Tarbuk A, Grancaric AM, Leskovac M. Novel cotton cellulose by cationisation during the mercerisation process-part 1: Chemical and morphological changes. Cellulose. 2014;21(3).

65. Zhuang J, Rong N, Wang X, Chen C, Xu Z. Adsorption of small size microplastics based on cellulose nanofiber aerogel modified by quaternary ammonium salt in water. Vol. 293, Separation and Purification Technology. 2022.

66. Trache D, Tarchoun AF, Derradji M, Hamidon TS, Masruchin N, Brosse N, et al. Nanocellulose: From Fundamentals to Advanced Applications. Vol. 8, Frontiers in Chemistry. 2020.

67. Patil T V., Patel DK, Dutta SD, Ganguly K, Santra TS, Lim KT. Nanocellulose, a versatile platform: From the delivery of active molecules to tissue engineering applications. Vol. 9, Bioactive Materials. 2022.

68. Phanthong P, Reubroycharoen P, Hao X, Xu G, Abudula A, Guan G. Nanocellulose: Extraction and application. Vol. 1, Carbon Resources Conversion. 2018.

69. Kocaman C, Bukusoglu E, Culfaz-Emecen PZ. Controlling Ultrafiltration Membrane Rejection via Shear-Aligned Deposition of Cellulose Nanocrystals from Aqueous Suspensions. ACS Appl Mater Interfaces. 2021;13(30).

70. Kocaman C, Bukusoglu E, Çulfaz-Emecen PZ. Tuning electrostatic interactions for controlled structure and rejection of cellulose nanocrystal membranes. J Memb Sci. 2022;661.

71. Yang M, Hadi P, Yin X, Yu J, Huang X, Ma H, et al. Antifouling nanocellulose membranes: How subtle adjustment of surface charge lead to self-cleaning property. J Memb Sci. 2021;618.

72.   Li N, Zheng J, Hadi P, Yang M, Huang X, Ma H, et al. Synthesis and characterization of a high flux nanocellulose–cellulose acetate nanocomposite membrane. Membranes (Basel). 2019;9(6).

73.   Thakur V, Guleria A, Kumar S, Sharma S, Singh K. Recent advances in nanocellulose processing, functionalization and applications: A review. Vol. 2, Materials Advances. 2021.

74.   Hasani M, Cranston ED, Westman G, Gray DG. Cationic surface functionalization of cellulose nanocrystals. Soft Matter [Internet]. 2008;4(11):2238–44. Available from: http://xlink.rsc.org/?DOI=B806789A

75.   Siró I, Plackett D, Hedenqvist M, Ankerfors M, Lindström T. Highly transparent films from carboxymethylated microfibrillated cellulose: The effect of multiple homogenization steps on key properties. J Appl Polym Sci. 2011;119(5).

76.   Fraschini C, Chauve G, Bouchard J. TEMPO-mediated surface oxidation of cellulose nanocrystals (CNCs). Cellulose [Internet]. 2017 Jul 6;24(7):2775–90. Available from: http://link.springer.com/10.1007/s10570-017-1319-5

77.   Beck S, Méthot M, Bouchard J. General procedure for determining cellulose nanocrystal sulfate half-ester content by conductometric titration. Cellulose. 2015;22(1).

78.   Indarti E, Marwan, Rohaizu R, Wanrosli WD. Silylation of TEMPO oxidized nanocellulose from oil palm empty fruit bunch by 3-aminopropyltriethoxysilane. Int J Biol Macromol. 2019;135.

79.   Goussé C, Chanzy H, Cerrada ML, Fleury E. Surface silylation of cellulose microfibrils: Preparation and rheological properties. Polymer (Guildf). 2004;45(5).

80. Yang S, Chai XY, Nie SX, Song XP, Wu M. Research Progress on Improving Dispersibility and Hydrophobicity of Nanocellulose. Chung-kuo Tsao Chih/China Pulp and Paper. 2017;36(10).

81. Yu T, Zhu F, Peng X, Chen Z. Acetylated Nanocelluloses Reinforced Shape Memory Epoxy with Enhanced Mechanical Properties and Outstanding Shape Memory Effect. Nanomaterials. 2022;12(23).

82. Alimohammadzadeh R, Rafi AA, Goclik L, Tai CW, Cordova A. Direct organocatalytic thioglycolic acid esterification of cellulose nanocrystals: A simple entry to click chemistry on the surface of nanocellulose. Carbohydrate Polymer Technologies and Applications. 2022;3.

83. Patoary MK, Islam SR, Farooq A, Rashid MA, Sarker S, Hossain MY, et al. Phosphorylation of nanocellulose: State of the art and prospects. Vol. 201, Industrial Crops and Products. 2023.

84. Sirviö JA, Ukkola J, Liimatainen H. Direct sulfation of cellulose fibers using a reactive deep eutectic solvent to produce highly charged cellulose nanofibers. Cellulose. 2019;26(4).

85. Biyani M V., Foster EJ, Weder C. Light-healable supramolecular nanocomposites based on modified cellulose nanocrystals. ACS Macro Lett. 2013;2(3).

86. Richardson JJ, Björnmalm M, Caruso F. Technology-driven layer-by-layer assembly of nanofilms. Vol. 348, Science. 2015.

87. Joseph N, Ahmadiannamini P, Hoogenboom R, Vankelecom IvoFJ. Layer-by-layer preparation of polyelectrolyte multilayer membranes for separation. Polym Chem [Internet]. 2014;5(6):1817–31. Available from: http://xlink.rsc.org/?DOI=C3PY01262J

88. Wang H, Ishihara S, Ariga K, Yamauchi Y. All-metal layer-by-layer films: Bimetallic alternate layers with accessible mesopores for enhanced electrocatalysis. J Am Chem Soc. 2012;134(26).

89. Gundogdu D, Bütün V, Erel-Göktepe I. Preparation of Layer-by-Layer Films with Remarkably Different pH-Stability and Release Properties Using Dual Responsive Block Copolymer Micelles. Macromol Chem Phys. 2018;219(15).

90. Aydemir U, Ugur E, Ermis C, Aydemir FN, Ozdemir E, Banerjee S, et al. Boron Cage Triggered Micellization of a Neutral-Cationic Block Copolymer and Preparation of Boron-Containing Layer-by-Layer Microparticles. ACS Appl Polym Mater. 2022;

91. Kiziltay A, Gündoğan Z, Erel-Göktepe I, Hasirci N. Multilayer polymeric films for controlled release of ceftriaxone sodium. Turk Hijyen ve Deneysel Biyoloji Dergisi. 2019;76(3).

92. Gundogdu D, Alemdar C, Turan C, Hazal Husnugil H, Banerjee S, Erel-Goktepe I. Tuning stimuli-responsive properties of alginate hydrogels through layer-by-layer functionalization for dual-responsive dual drug release. Colloids Surf A Physicochem Eng Asp. 2023;676.

93. Ulusan S, Bütün V, Banerjee S, Erel-Goktepe I. Biologically Functional Ultrathin Films Made of Zwitterionic Block Copolymer Micelles. Langmuir. 2019;35(5).

94. Akbar M, Cagli E, Erel-Göktepe I. Layer-By-Layer Modified Superparamagnetic Iron Oxide Nanoparticles with Stimuli-Responsive Drug Release Properties. Macromol Chem Phys. 2019;220(4).

95. Saracogullari N, Gundogdu D, Ozdemir FN, Soyer Y, Erel-Goktepe I. The effect of polyacid on the physical and biological properties of chitosan based layer-by-layer films. Colloids Surf A Physicochem Eng Asp. 2021;617.

96. Lee D, Rubner MF, Cohen RE. All-nanoparticle thin-film coatings. Nano Lett. 2006;6(10).

97. Iler RK. Multilayers of colloidal particles. J Colloid Interface Sci. 1966;21(6).

98. Decher G, Hong JD, Schmitt J. Buildup of ultrathin multilayer films by a self-assembly process: III. Consecutively alternating adsorption of anionic and cationic polyelectrolytes on charged surfaces. Thin Solid Films. 1992;210–211(PART 2).

99. Tekinalp Ö, Alsoy Altinkaya S. Development of high flux nanofiltration membranes through single bilayer polyethyleneimine/alginate deposition. J Colloid Interface Sci. 2019;537.

100. Norrman K, Ghanbari-Siahkali A, Larsen NB. Studies of spin-coated polymer films. Vol. 101, Annual Reports on the Progress of Chemistry - Section C. 2005.

101. Cai J, Chen Q, Chang C. Spray-assisted LBL assembly of chitosan/nanocellulose as coatings of commercial membranes for oil-in-water emulsion separation. Int J Biol Macromol. 2023;242.

102. Sun J, Gao M, Feldmann J. Electric Field Directed Layer-by-Layer Assembly of Highly Fluorescent CdTe Nanoparticles. J Nanosci Nanotechnol. 2001;1(2).

103. Hong X, Li J, Wang M, Xu J, Guo W, Li J, et al. Fabrication of magnetic luminescent nanocomposites by a layer-by-layer self-assembly approach. Chemistry of Materials. 2004;16(21).

104. Wang Y, Liu Y, Cheng Y, Kim E, Rubloff GW, Bentley WE, et al. Coupling electrodeposition with layer-by-layer assembly to address proteins within microfluidic channels. Advanced Materials. 2011;23(48).

105. Wang C, Park MJ, Gonzales RR, Phuntsho S, Matsuyama H, Drioli E, et al. Novel organic solvent nanofiltration membrane based on inkjet printing-assisted layer-by-layer assembly. J Memb Sci. 2022;655.

106. Tieke B, van Ackern F, Krasemann L, Toutianoush A. Ultrathin self-assembled polyelectrolyte multilayer membranes. The European Physical Journal E [Internet]. 2001 May;5(1):29–39. Available from: http://link.springer.com/10.1007/s101890170084

107. Hong SU, Ouyang L, Bruening ML. Recovery of phosphate using multilayer polyelectrolyte nanofiltration membranes. J Memb Sci. 2009;327(1–2).

108. Hong SU, Bruening ML. Separation of amino acid mixtures using multilayer polyelectrolyte nanofiltration membranes. J Memb Sci. 2006;280(1–2).

109. Hong SU, Miller MD, Bruening ML. Removal of dyes, sugars, and amino acids from NaCl solutions using multilayer polyelectrolyte nanofiltration membranes. Ind Eng Chem Res. 2006;45(18).

110. Ouyang L, Malaisamy R, Bruening ML. Multilayer polyelectrolyte films as nanofiltration membranes for separating monovalent and divalent cations. J Memb Sci. 2008;310(1–2).

111. Hong SU, Malaisamy R, Bruening ML. Separation of fluoride from other monovalent anions using multilayer polyelectrolyte nanofiltration membranes. Langmuir. 2007;23(4).

112. Ahmadiannamini P, Li X, Goyens W, Meesschaert B, Vankelecom IFJ. Multilayered PEC nanofiltration membranes based on SPEEK/PDDA for anion separation. J Memb Sci. 2010;360(1–2).

113. Li X, Goyens W, Ahmadiannamini P, Vanderlinden W, De Feyter S, Vankelecom I. Morphology and performance of solvent-resistant nanofiltration membranes based on multilayered polyelectrolytes: Study of preparation conditions. J Memb Sci. 2010;358(1–2).

114. Jin W, Toutianoush A, Tieke B. Use of Polyelectrolyte Layer-by-Layer Assemblies as Nanofiltration and Reverse Osmosis Membranes. Langmuir [Internet]. 2003 Apr 1;19(7):2550–3. Available from: https://pubs.acs.org/doi/10.1021/la020926f

115. Toutianoush A, Jin W, Deligöz H, Tieke B. Polyelectrolyte multilayer membranes for desalination of aqueous salt solutions and seawater under reverse osmosis conditions. In: Applied Surface Science. 2005.

116. Park J, Park J, Kim SH, Cho J, Bang J. Desalination membranes from pH-controlled and thermally-crosslinked layer-by-layer assembled multilayers. J Mater Chem. 2010;20(11).

117. Elzbieciak M, Kolasinska M, Warszynski P. Characteristics of polyelectrolyte multilayers: The effect of polyion charge on thickness and wetting properties. Colloids Surf A Physicochem Eng Asp. 2008;321(1–3).

118. DuChanois RM, Epsztein R, Trivedi JA, Elimelech M. Controlling pore structure of polyelectrolyte multilayer nanofiltration membranes by tuning polyelectrolyte-salt interactions. J Memb Sci [Internet]. 2019 Jul;581:413–20. Available from: https://linkinghub.elsevier.com/retrieve/pii/S0376738819302601

119. Rajesh S, Zhao Y, Fong H, Menkhaus TJ. Polyacrylonitrile nanofiber membranes modified with ionically crosslinked polyelectrolyte multilayers for the separation of ionic impurities. Nanoscale. 2016;8(43).

120. Wågberg L, Erlandsson J. The Use of Layer-by-Layer Self-Assembly and Nanocellulose to Prepare Advanced Functional Materials. Advanced Materials [Internet]. 2021 Jul 7;33(28). Available from: https://onlinelibrary.wiley.com/doi/10.1002/adma.202001474

121. Li F, Biagioni P, Finazzi M, Tavazzi S, Piergiovanni L. Tunable green oxygen barrier through layer-by-layer self-assembly of chitosan and cellulose nanocrystals. Carbohydr Polym. 2013;92(2).

122. Trigueiro JPC, Silva GG, Pereira FV, Lavall RL. Layer-by-layer assembled films of multi-walled carbon nanotubes with chitosan and cellulose nanocrystals. J Colloid Interface Sci. 2014;432.

123. Podsiadlo P, Choi SY, Shim B, Lee J, Cuddihy M, Kotov NA. Molecularly engineered nanocomposites: Layer-by-layer assembly of cellulose nanocrystals. Biomacromolecules. 2005;6(6).

124. Fuson RC, Bull BA. The haloform reaction. Chem Rev. 1934;15(3).

125. Gordon G, Adam LC, Bubnis BP, Kuo C, Cushing RS, Sakaji RH. Predicting liquid bleach decomposition. J Am Water Works Assoc. 1997;89(4).

126. Thoma JA, French D. The Starch-Iodine-Iodide Interaction. Part I. Spectrophotometric Investigations. J Am Chem Soc. 1960;82(16).

127. Brown SD, Beebe TP. Preparation of standard sodium thiosulfate solution and determination of hypochlorite in a commerical bleach product. University of Delaware. 2005;

128. Lin N, Dufresne A. Surface chemistry, morphological analysis and properties of cellulose nanocrystals with gradiented sulfation degrees. Nanoscale. 2014;6(10).

129. Swan JD. Determination of Epoxides with Sodium Sulfite. Anal Chem. 1954;26(5).

130. Edson JB, Boncella JM. Decomposition pathways of tetraalkylammonium cations via evolved gas analysis: Implications for hydroxide ion conducting fuel cell membranes. In: ACS National Meeting Book of Abstracts. 2011.

131. Kim KJ, Fane AG, Ben Aim R, Liu MG, Jonsson G, Tessaro IC, et al. A comparative study of techniques used for porous membrane characterization: pore characterization. J Memb Sci. 1994;87(1–2).

132. Batistela VR, Pellosi DS, De Souza FD, Da Costa WF, De Oliveira Santin SM, De Souza VR, et al. PKa determinations of xanthene derivates in aqueous solutions by multivariate analysis applied to UV-Vis spectrophotometric data. Spectrochim Acta A Mol Biomol Spectrosc. 2011;79(5).

133. Chial HJ, Thompson HB, Splittgerber AG. A spectral study of the charge forms of Coomassie blue G. Anal Biochem. 1993;209(2).

134. Adams EQ, Rosenstbin L. The color and ionization of crystal-violet. J Am Chem Soc. 1914;36(7).

135. Sakaino K, Kawabata Y, Adachiz S. Etching Characteristics of Si(100) Surfaces in an Aqueous NaOH Solution. J Electrochem Soc. 2000;147(4).

136. Morita M, Ohmi T, Hasegawa E, Kawakami M, Ohwada M. Growth of native oxide on a silicon surface. J Appl Phys. 1990;68(3).

137. Van Horn BL, Winter HH. Dynamics of shear aligning of nematic liquid crystal monodomains. In: Rheologica Acta. 2000.

138. Sørensen BE. A revised Michel-Lévy interference colour chart based on first-principles calculations. European Journal of Mineralogy. 2013;25(1).

139. Wei YS, Chen KS, Wu LT. In situ synthesis of high swell ratio polyacrylic acid/silver nanocomposite hydrogels and their antimicrobial properties. J Inorg Biochem. 2016;164.

APPENDICES

Example rejection and sorption calculations are available in Appendix A, GPC signal analysis information is available in Appendix B, dye calibration curves are available in Appendix C, CNC size and zeta potential distribution data is available in Appendix D, surface charge density calculations are available in Appendix E, and supporting rejection and PSP data is available in Appendix F.

A. Example Rejection and Sorption Calculations in Dead-End Mode

For a hypothetical experiment, let the sample concentrations be measured as described in Table 5.1.

Table 5.1 Example Sample Concentrations

Sample	Concentration	Volume
Initial Feed	1000 ppm	100mL
Permeate 1	50 ppm	10mL
Permeate 2	70 ppm	10mL
Permeate 3	95 ppm	10mL
Last Retentate	1402 ppm	70mL

The feed concentration when permeate 2 has been collected can be calculated as:

$$C_{feed,2} = \frac{C_{last\ retentate} * V_{last\ retentate} + C_{permeate\ 3} * V_{permeate\ 3}}{V_{last\ retentate} + V_{permeate\ 3}}$$

$$= \frac{1402ppm * 70mL + 95ppm * 10mL}{80mL} = 1239ppm$$

The feed concentration when permeate 1 has been collected can be calculated as:

$$C_{Feed,1} = \frac{C_{feed,2} * V_{feed,2} + C_{permeate\ 2} * V_{permeate\ 2}}{V_{feed,2} + V_{permeate\ 2}}$$

$$= \frac{1239ppm * 80mL + 70ppm * 10mL}{90mL} = 1109ppm$$

The initial feed is also double checked as:

$$C_{Feed,0} = \frac{C_{feed,1} * V_{feed,1} + C_{permeate\ 1} * V_{permeate\ 1}}{V_{feed,1} + V_{permeate\ 1}}$$

$$= \frac{1109ppm * 90mL + 50ppm * 10mL}{100mL} \approx 1000ppm$$

Which checks with the observed value, indicating that the material balance holds.

Rejections can be then calculated as follows:

$$R_1 = 1 - \frac{C_{permeate\ 1}}{0.5 * \left(C_{feed,0} + C_{feed,1}\right)} = 1 - \frac{50ppm}{0.5 * (1000ppm + 1109ppm)} = 0.953$$

$$R_2 = 1 - \frac{C_{permeate\ 2}}{0.5 * \left(C_{feed,1} + C_{feed,2}\right)} = 1 - \frac{70ppm}{0.5 * (1109ppm + 1239ppm)} = 0.940$$

$$R_3 = 1 - \frac{C_{permeate\ 3}}{0.5 * \left(C_{feed,2} + C_{last\ retentate}\right)} = 1 - \frac{95ppm}{0.5 * (1239ppm + 1402ppm)}$$
$$= 0.928$$

The reason for using an average of two different feed concentrations is that the average value is the approximate feed concentration encountered as that particular permeate sample is collected. For example, permeate 1 will be collected from a feed changing in composition but with an average composition represented accurately by $0.5*(C_{feed,0} + C_{feed,1})$.

If the calculated initial feed concentration is significantly lower than the measured value, sorption of the probe molecule has to be considered. For example, if the data obtained instead had the values:

Table 5.2 Example Sample Concentrations with Sorption

Sample	Concentration	Volume
Initial Feed	1000 ppm	100mL
Permeate 1	50 ppm	10mL
Permeate 2	70 ppm	10mL
Permeate 3	95 ppm	10mL
Last Retentate	1100 ppm	70mL

The feed concentrations would instead be:

$$C_{feed,2} = \frac{C_{last\ retentate} * V_{last\ retentate} + C_{permeate\ 3} * V_{permeate\ 3}}{V_{last\ retentate} + V_{permeate\ 3}}$$

$$= \frac{1100ppm * 70mL + 95ppm * 10mL}{80mL} = 974ppm$$

$$C_{Feed,1} = \frac{C_{feed,2} * V_{feed,2} + C_{permeate\ 2} * V_{permeate\ 2}}{V_{feed,2} + V_{permeate\ 2}}$$

$$= \frac{974ppm * 80mL + 70ppm * 10mL}{90mL} = 873ppm$$

$$C_{Feed,0} = \frac{C_{feed,1} * V_{feed,1} + C_{permeate\ 1} * V_{permeate\ 1}}{V_{feed,1} + V_{permeate\ 1}}$$

$$= \frac{873ppm * 90mL + 50ppm * 10mL}{100mL} = 791ppm$$

In this example, the feed concentration calculated from a material balance using retentate and permeate samples is significantly less than the measured feed concentration. The sorbed amount can then be reported as:

$$m_{sorbed} = (C_{feed\ actual} - C_{feed\ calculated}) * V_{feed}$$

$$= (1000ppm - 791ppm) * 0.1L = 20.9mg$$

B. GPC Signal Analysis

The chromatograms obtained for the samples were converted to MS-DOS comma-separated value (.csv) format and opened with the program fityk, where Gaussian curve fitting was done. The identities of the probes were inferred using their residence times.
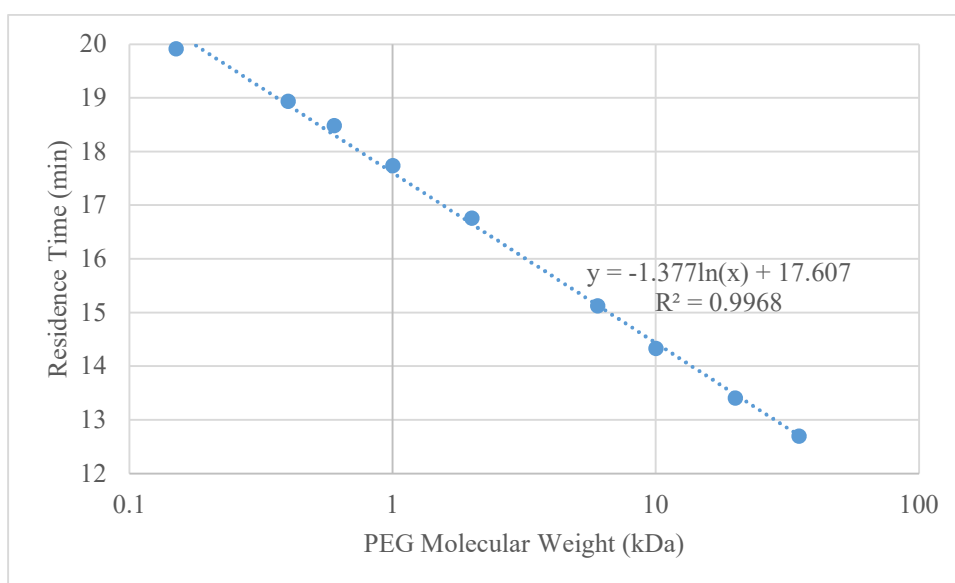

Figure 5.1 Example PEG Residence Times in Aqueous Environment

Peak areas were then obtained from the program and converted to concentrations using linear calibration graphs as seen in Figure 5.2. Example fitted curves for aqueous solutions and organic solutions are available in Figure 5.3, Figure 5.4, and Figure 5.5.
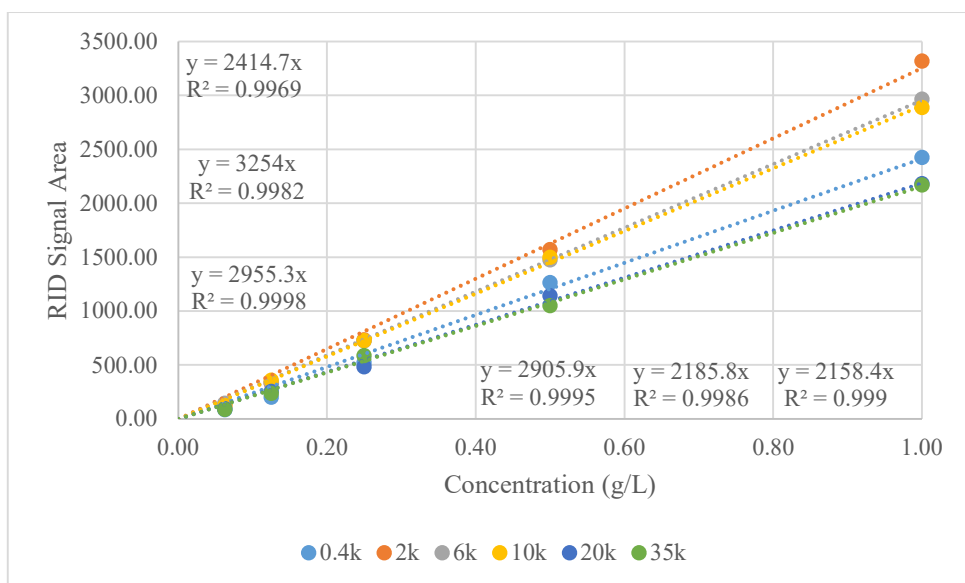
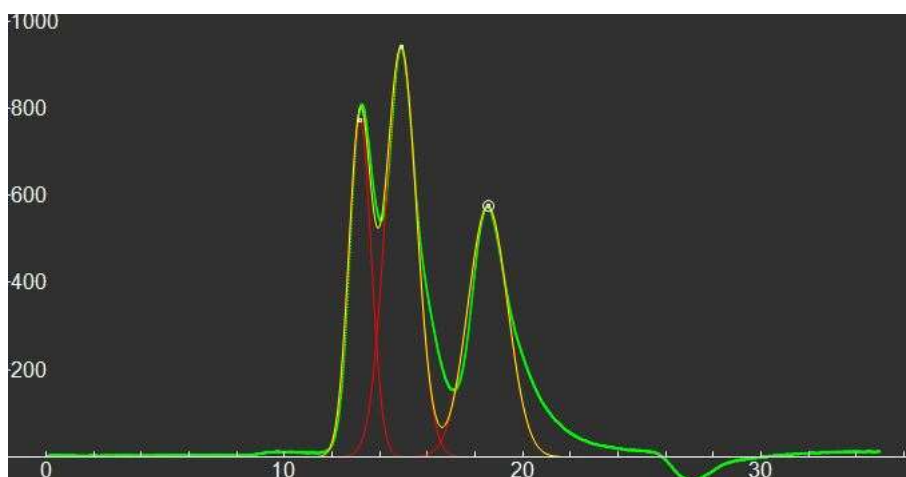Figure 5.2 PEG Calibration Curves in the Solvent DMF

Figure 5.3 Example Curve Fitting to a Chromatogram. The y-axis has the units nano refractive index units (nRIU) and the x-axis represents the time elapsed in minutes.

In the sample used to obtain the chromatogram in Figure 5.3, the solvent is UPW, and 0.5 g/L each of PEG 400Da, 6kDa, and 20kDa are present as solutes.
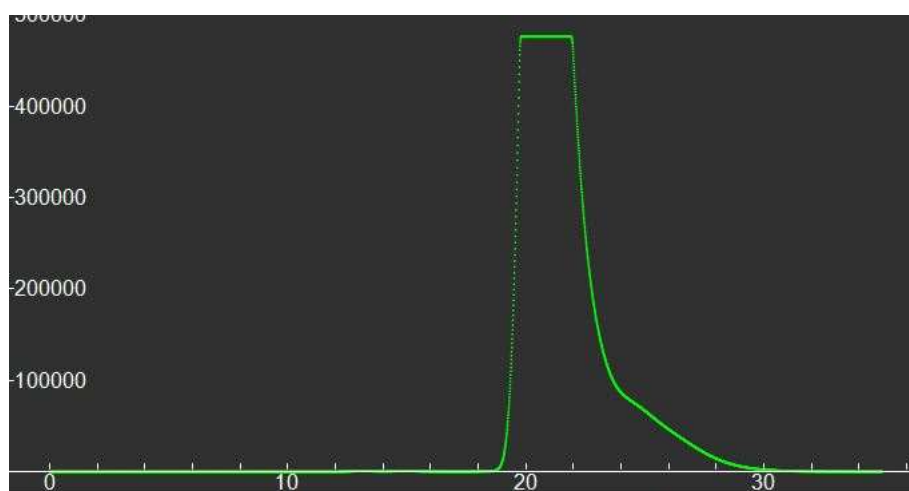
Figure 5.4 Example Chromatogram Obtained from an Organic Solution. The y-axis has the units nano refractive index units (nRIU) and the x-axis represents the time elapsed in minutes.

The solvent of the sample which was used to obtain the chromatogram in Figure 5.4 is DMSO. As can be seen from the figure, the solvent signal overpowers the PEG signals. Therefore, curve fitting by hand was done for organic solvents.
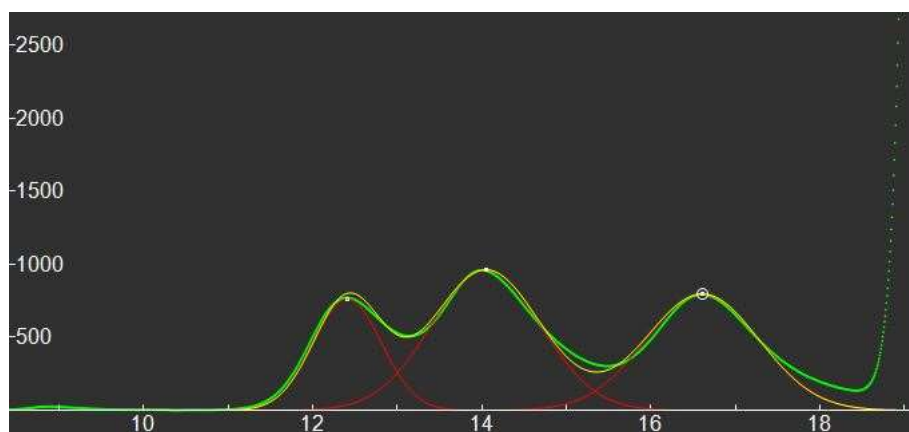

Figure 5.5 Example Curve Fitting for Samples in Organic Solvents. The y-axis has the units nano refractive index units (nRIU) and the x-axis represents the time elapsed in minutes.

The PEG signals become apparent after zooming in to exclude the solvent signal, and the fitted curves can be used to extract signal area data.

C. Dye Calibration Curves

Absorbance values were recorded using a UV-VIS spectrophotometer Shimadzu UV-1601. Measurements were taken in quartz cuvettes with an optical path length of 1 cm. In the case of dyes sorbing strongly to the cuvettes, the cuvettes were washed with EtOH in between measurements to flush out the dye.
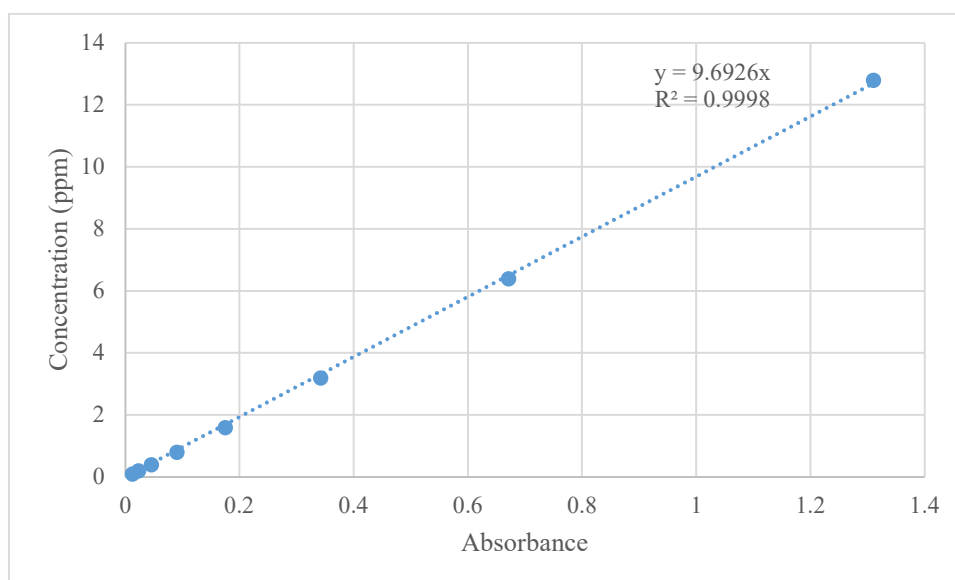

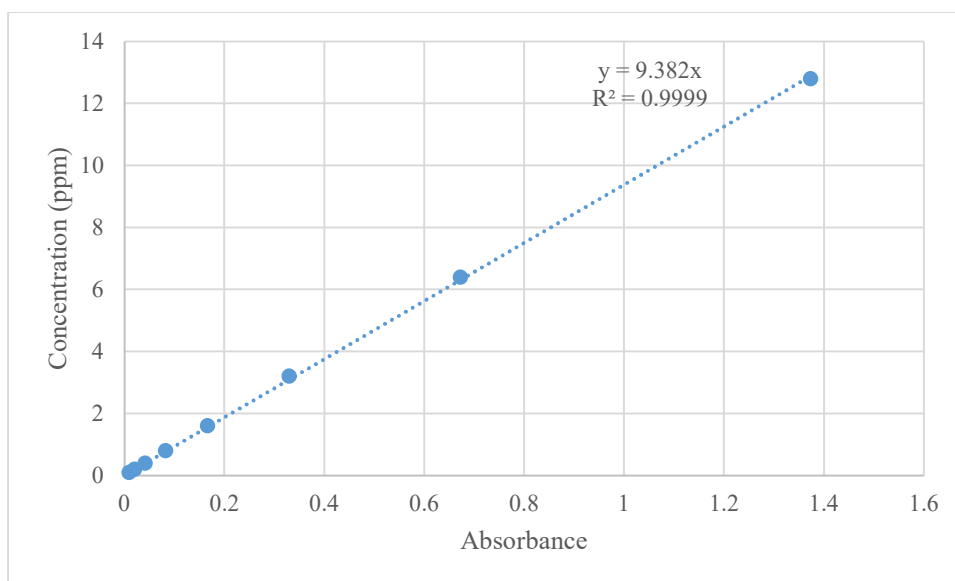Figure 5.6 RB Calibration Curve in UPW at 550nm Wavelength

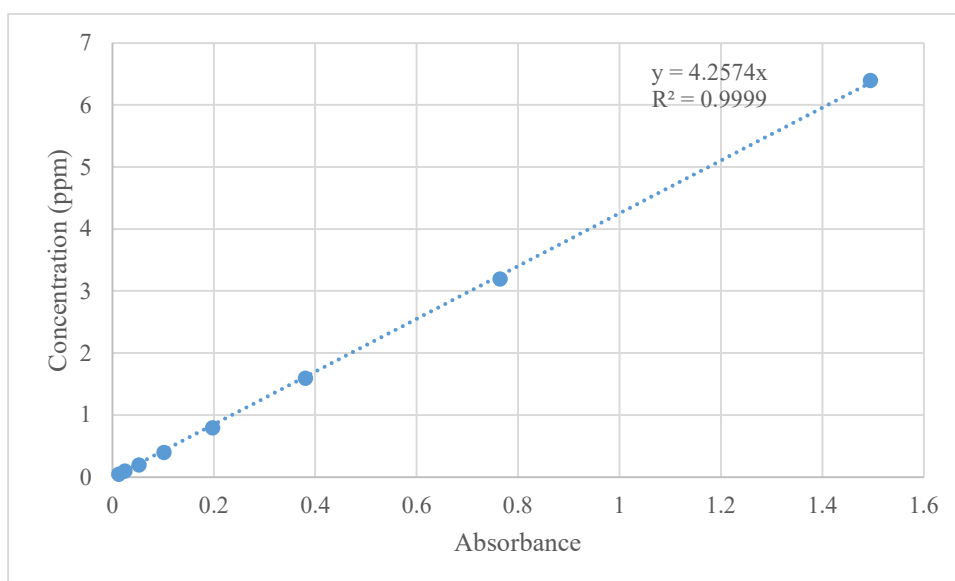Figure 5.7 RB Calibration Curve in MeOH at 558nm Wavelength

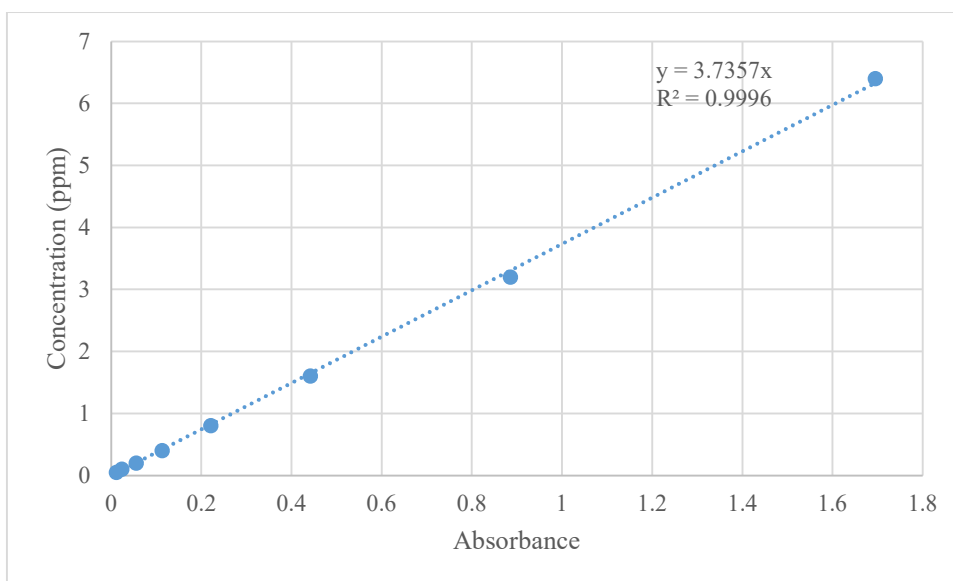Figure 5.8 CV Calibration Curve in UPW at 590nm Wavelength

Figure 5.9 CV Calibration Curve in UPW at 585nm Wavelength

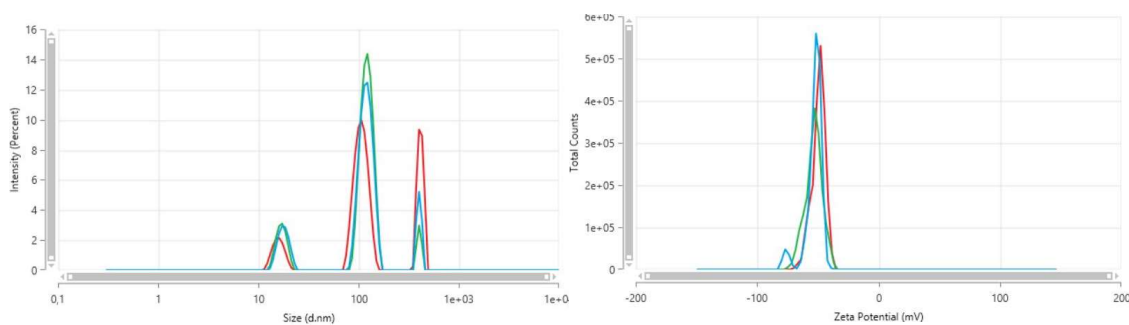**D. Size and Zeta Potential Distributions of Nanocellulose**

Figure 5.10 Size (left) and Zeta Potential (right) Distributions of Dilute, Homogenized CNC Suspension in UPW
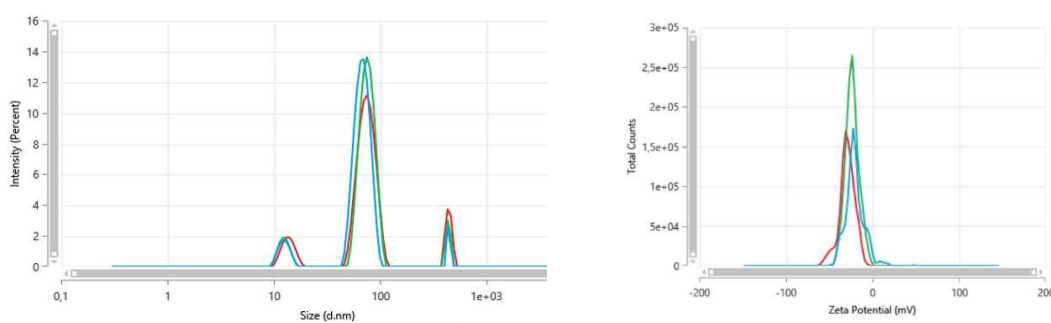

Figure 5.11 Size (left) and Zeta Potential (right) Distributions of Dilute, Homogenized TEMPO-CNC Suspension in UPW
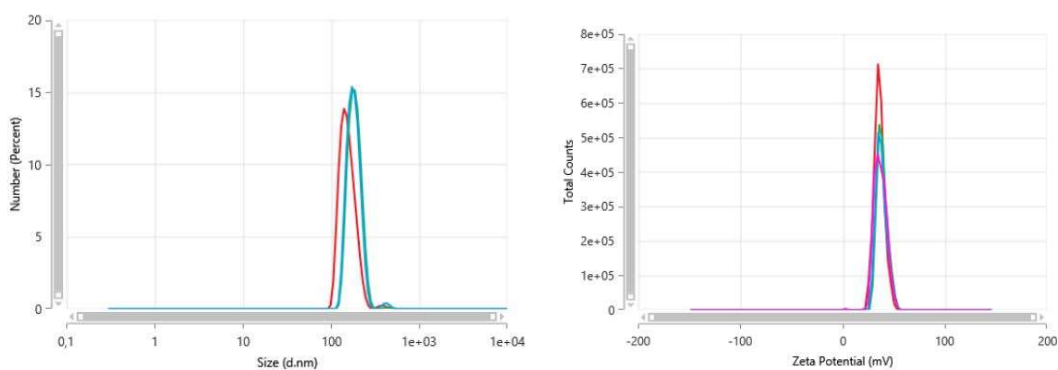

Figure 5.12 Size (left) and Zeta Potential (right) Distributions of Dilute, Homogenized CNC+ Suspension in UPW

E. Surface Charge Density Calculations

Cellulose nanocrystals may be reasonably approximated as rods of 180nm length and 8nm diameter. Their volume, surface area, mass and specific surface area can then be calculated as:

$$V_{CNC} = \frac{\pi d^2 L}{4} = \frac{\pi * 64nm^2 * 180nm}{4} \approx 9050nm^3 = 9.050 * 10^{-24}m^3$$

$$A_{CNC} = \pi dL + \frac{\pi d^2}{2} = \pi * 8nm * 180nm + \frac{\pi * 64nm^2}{2} \approx 4840nm^2$$
$$= 4.840 * 10^{-15}m^2$$

$$m_{CNC} = V_{CNC}\rho_{CNC} = 9.050 * 10^{-24}m^3 * 1500\frac{kg}{m^3} = 1.358 * 10^{-20}kg$$

$$SSA_{CNC} = \frac{A_{CNC}}{m_{CNC}} = \frac{4.840 * 10^{-15}m^2}{1.358 * 10^{-20}kg} = 356400\frac{m^2}{kg}$$

Therefore, the surface charge densities may be calculated as:

$$\sigma_{CNC} = \frac{F * \hat{N}_{charge}}{SSA_{CNC}} = \frac{96500\frac{C}{mol} * -0.3\frac{mol}{kg}}{356400\frac{m^2}{kg}} = -0.0812\frac{C}{m^2}$$

$$\sigma_{CNC+} = \frac{F * \hat{N}_{charge}}{SSA_{CNC}} = \frac{96500\frac{C}{mol} * 0.15\frac{mol}{kg}}{356400\frac{m^2}{kg}} = 0.0406\frac{C}{m^2}$$

And individual particle charges may be calculated as:

$$z_{CNC} = \hat{N}_{charge} * m_{CNC} * N_A = -0.3\frac{mol}{kg} * 1.358 * 10^{-2}\ kg * 6.022 * 10^{23}\frac{1}{mol}$$
$$\approx -2450$$

$$z_{CNC+} = \hat{N}_{charg}\ * m_{CNC} * N_A = 0.15\frac{mol}{kg} * 1.358 * 10^{-20}kg * 6.022 * 10^{23}\frac{1}{mol}$$
$$\approx 1230$$

F. Supporting Rejection and PSP Data

Table 5.3 Pure Solvent Permeances of PRCA-15 Support Membrane

Solvent	Viscosity (cP)	PSP (L/hm^{2}bar)
Water	0.89	69 ± 8
MeOH	0.59	97
DMSO	1.99	26
DMF	0.80	37

Table 5.4 PEG Rejections of the Support Membrane PRCA12-UPW8 in UPW

PEG MW (kDa)	Fractional Rejection
0.4	0.01
2	0.08
6	0.32
10	0.50
20	0.76
35	0.85

Table 5.5 PEG Rejections of the Support Membrane PRCA-15

PEG MW (kDa)	Fractional Rejection Values in the Solvent:			
	UPW	MeOH	DMSO	DMF
0.4	0.22	0.01	NA	0.21
2	0.24	0.04	0.52	0.48
6	0.71	0.23	0.76	0.61
10	0.94	0.35	1.00	0.72
20	1.00	0.56	1.00	0.94
35	1.00	0.74	1.00	0.95